UNIVERSITY OF OKLAHOMA

GRADUATE COLLEGE

THE DEVELOPMENT OF A COMBINED APPROACH FOR THE REAL-TIME, NON-DESTRUCTIVE MONITORING OF *IN VITRO* BONE TISSUE ENGINEERED CONSTRUCTS UTILIZING PHYSIO-METABOLIC MARKERS

A THESIS

SUBMITTED TO THE GRADUATE FACULTY

in partial fulfillment of the requirements for the

Degree of

MASTER OF SCIENCE

By

AARON D. SIMMONS
Norman, Oklahoma
2016

THE DEVELOPMENT OF A COMBINED APPROACH FOR THE
REAL-TIME, NON-DESTRUCTIVE MONITORING OF
IN VITRO BONE TISSUE ENGINEERED CONSTRUCTS
UTILIZING PHYSIO-METABOLIC MARKERS

A THESIS APPROVED FOR THE
SCHOOL OF CHEMICAL, BIOLOGICAL AND MATERIALS ENGINEERING

BY

_____
Dr. Vassilios I. Sikavitsas, Chair

_____
Dr. Matthias U. Nollert

_____
Dr. Roger G. Harrison

ACKNOWLEDGMENTS

I would like to thank, first and foremost, my advisor, Dr. Vassilios Sikavitsas, for it is through his support, guidance, and advice these past few years, not only in research, but in life, that I have achieved much that I have accomplished in this time, including my successful attainment of a Master's Degree in Chemical Engineering. Of course, this would not have been possible without the assistance of the rest of my committee, to whom I am also grateful: Dr. Matthias Nollert and Dr. Roger Harrison.

Furthermore, I would like to extend my gratitude to the ever-approachable faculty and staff of the School of Chemical, Biological and Materials Engineering with special thanks to Dr. Lance Lobban and Dr. Edgar O'Rear for sharing their knowledge and wisdom, Terri Colliver, Donna King, Wanda Gress, and Madena McGinnis, for keeping me on track and always being available to talk, and Alan Miles for all of his assistance over the years.

Additionally, I want to thank my lab mates and peers over the years for their support, friendship, and at times, comic relief: Zach Mussett, Cortes Williams, Julien Arrizabalaga, Needa Virani, Patrick McKernan, Jin Liu, James Buerck, and Zach Yokell, among others, with special thanks to Brandon Engebretson for training me upon first joining the lab what seems like so long ago.

Finally, no acknowledgment would be complete without recognizing my parents, Thomas and Loretta Simmons, for all of their support and guidance through all of the years leading up to, and through, my degree and forever more.

TABLE OF CONTENTS

LIST OF TABLES

LIST OF FIGURES

ABSTRACT

Annually, over $2.5 billion is spent on more than 500,000 bone grafts in the US alone, with more than 2 million being implanted worldwide. The limited supply of autografts and complications associated with traditional alternatives leave much to be desired. As of late, bone tissue engineering has developed as a promising alternative to these "gold standard" strategies for bone regeneration, effectively combining a patient's own cells with biological factors together on a supportive construct to promote and induce *de novo* bone tissue formation. Due to the complexity involved in such an approach, its pathway to clinical application is wrought with numerous regulatory demands, all of which must be met in order to secure FDA approval prior to realization of clinical relevance. Key among these is the ability to monitor tissue engineered constructs, being able to effectively track such key aspects of construct quality as cellularity and degree of maturation (differentiation and mineralization). In the field, current methodologies for the determination of said aspects require the sacrificial destruction of the cultured constructs, an obviously infeasible practice for regenerative medical applications. As such, the main objective of this study was the development of alternative strategies for the real-time, non-destructive monitoring of bone tissue engineered constructs.

To this end, constructs comprised of 85% porous poly(L-lactic acid) (PLLA) spunbonded fibrous scaffolds were dynamically seeded with 1.5 MM rat mesenchymal stem cells (rMSCs) and cultured within flow perfusion bioreactors (providing for the mitigation of nutrient gradients and the beneficial introduction of shear stresses throughout the construct) with either basal or osteoinductive media for periods of up to 14 days. Throughout the culture period, oxygen concentration measurements were taken

at the inlet and outlet of each construct and global media samples were taken and assayed for glucose and osteoprotegerin content in order to determine oxygen uptake, glucose consumption, and osteoprotegerin (OPG) production rates. As specified time points throughout the culture period (Days 1, 3, 5, 7, 9, 11, and 14), constructs were sacrificed and assayed for cellularity (via a dsDNA assay), alkaline phosphatase (ALP) activity, and calcium deposition. Comparative analysis of trends in both the non-invasive mid-culture and destructive post-culture data revealed correlations that can be utilized for the real-time, mid-culture determination of construct quality. Key trends observed include increases in the cell-specific rate of oxygen uptake and decreases in the cell-specific rate of glucose consumption by osteoinduced constructs with little change in non-osteoinduced ones and a steady cell-specific production rate of OPG for osteoinduced cultures as compared to significantly decreased production rates for non-osteoinduced cultures. The opposing trends for oxygen uptake and glucose consumption of osteoinduced cultures can be explained my metabolic shifts in differentiating MSCs, a phenomenon which has proven useful in the development of monitoring metrics herein. Utilization of the ratio of oxygen uptake rate to glucose consumption rate as a key determinant of construct quality has proven promising in the analyses performed herein, potentially allowing for the elucidation of both a construct's maturation and its cellularity non-destructively in real time.

1. INTRODUCTION

1.1 Background and Significance

1.1.1 Bone Tissue Defects

Bone tissue defects effects millions of people annually, requiring in excess of two million bone graft interventions (with over 500,000 of these being required in the US alone, at a cost of over $2.5 billion) [1,2]. As daunting as these figures seem they are expected to double by the year 2020, exacerbated by an aging and increasingly obese population, leading to particularly high projected increases in the need for long bone and spinal fusion procedures [2,3].

Common defects requiring surgical intervention span from simple fractures (suffering from non-union or delayed-union complications) to mass resection of bone tissue as a result of malignant tumor formation [4,5]. Furthermore, bone grafts are often implemented alongside implanted devices, as a means to aid in the incorporation and mitigation of immune rejection thereof [6].

1.1.2 Bone Grafts and Alternatives

The “gold standard” for bone grafts is the autograft, a section of bone obtained from a donor site elsewhere in the patient receiving the graft. Such a graft has the benefits of complete histocompatibility and intrinsic bone-supportive properties [5]. Numerous limitations, however, exist for autografts including scarcity of viable donor tissue, donor site morbidity, and the requirement for two surgical procedures thereby increasing costs in addition to the potential for infection.

In attempt to overcome some of the limitations of autografts, many people rely on foreign sources for graft supply, obtaining donor tissue from deceased human cadavers (allografts) or other animal sources (xenografts). Although these two sources do much to push beyond autografts with respect to availability, they are still subject to supply limitations. Furthermore, the introduction of non-native tissue to a patient brings with it numerous complications including the possibilities of immune rejection, infection, and disease transmission. Additionally, these grafts require extensive processing to remove the cells and other immunogenic material thereby rendering them much less osteo-potent than autografts. [2,4,5]

Non-tissue synthetic alternatives to the above traditional grafts have been employed to great extent due to their ready availability, ease of manufacturing into the specific size and shape required, relatively low cost, and elimination of the risk of disease transmission. These grafts are typically comprised of various calcium-based ceramics, metals, polymers, hydrogels, etc. As a result, they often exhibit good osteoconductive properties and can exhibit some beneficial osteoinductive ones, but due to their lack of cells they lack the osteogenicity afforded by autografts. Finally, depending on the specific material selected, the site of implantation, and the patient himself, a synthetic graft may elicit a foreign body response from the immune system resulting in graft rejection. [1,4,5]

One final type of graft seeks to mitigate the limitations and complications of these aforementioned grafts, while incorporating as many of their benefits as possible: the bone tissue engineered graft. Although not currently available for surgical intervention, these grafts are being heavily researched as of late and have shown promising results in

numerous animal models [7]. Essentially, they seek to combine synthetic grafts with a patient's own cells and potentially additional growth factors to produce a construct which is osteoconductive, osteoinductive, and osteogenic in addition to overcoming supply limitations and the risks of disease transmission and immune response. In order to achieve these numerous benefits, bone tissue engineered grafts do result in slightly longer preparation times and higher costs than the above-mentioned alternatives (the specifics of the bone tissue engineering approach are discussed in detail in **Section 1.3)**. **Table 1**, below shows a comparison of the benefits and detriments of each of the graft types discussed above.

		Autograft	**Allograft/ Xenograft**	**Synthetic Graft**	**Tissue Engineered Graft**
Graft Properties	Osteoconductivity	+++	++ / +++	++ / +++	++ / +++
	Osteoinductivity	+++	+ / ++	+ / ++	++ / +++
	Osteogenicity	++	0	0	++ / +++
Associated Risks	Infection	Moderate	Low	Low	Low
	Disease Transmission	0	Moderate	0	Low
	Immune Response	0	High	Moderate	Low / Mod
Constraints	Supply	Low	Moderate	High	Mod / High
	No. of Procedures	2	1	1	2*
	Time to Implantation	Hours	Hours	Hours	Days**
	Cost	Low	High	Moderate	Mod / High

Table 1. Comparison of Graft Alternatives
Graft properties (top) demonstrate beneficial bone-forming capabilities (more "+" corresponds to effect); osteoconductivity is the ability for a graft to serve as a viable construct for bone healing and in-growth, osteoinductivity is the ability for a graft to induce the differentiation of stem cells into mature bone cells, osteogenicity is the ability of a graft to itself produce new bone [8]. Associated risks (middle) demonstrate potential complications; higher risk of infection in the autograft is due to the requirement of multiple surgical interventions (increasing the amount of tissue exposed during operation, potential disease transmission in the tissue engineered graft is associated with supplements used in the culturing phase, immune response (or foreign body response) is associated with the introduction of foreign material (either natural or synthetic) into the patient. Constraints of each graft (bottom) represent relative limitations of each; supply demonstrates the amount of graft material available from

each source, time to implantation takes into account the time from the start of the first surgical intervention until the end of the last, cost takes into account the cost of materials, labor, and (in the case of tissue engineered grafts) the additional culture supplies and labor required prior to implantation, and the number of surgeries represents the number of individual surgical interventions required (autografts require two, one for the removal of donor tissue and a second for its implantation to the grafting site).
*Tissue engineered grafts require two procedures, although the first is a simple minimally invasive bone marrow biopsy requiring little time to complete.
**The time to implantation required for tissue engineered grafts is displayed as days due to the extended culture period required from the original bone marrow biopsy until the final construct is implanted into the patient. (Compiled from [1,5,9]).

1.2 Bone Physiology

In order to better understand the bone tissue engineering approach (detailed in the next section), the target tissue it aims to create must first be understood. Knowledge of this highly complex tissue also allows for the development of methods for the determination of the quality of such engineered constructs.

1.2.1 Function of Bone

Bone, comprising roughly 15% of the average person's mass, serves numerous functions for the body [10,11]. Far beyond providing simple structural support, bone also provides protection for vital internal organs and contains attachment sites for muscles, tendons, and ligaments to allow for locomotion [12–14]. Furthermore, bone serves several storage functions: it provides a reservoir for marrow (wherein blood cells are produced) and minerals (predominately calcium and phosphorus) in addition to acting as a sequester location for several dangerous minerals (such as lead) [12,14]. Finally, bone has homeostatic balancing functions, predominately acting to balance internal pH levels through the absorption and release of alkaline salts [13,14].

1.2.2 Composition of Bone

Bone is a highly complex tissue with numerous levels of organization. It is typically classified into two distinct categories based predominately on the porosity and meso-structural organization with cortical (compact) bone, being denser, and cancellous (spongy) bone being less so. These two types of bone will be discussed further in the next section, but first an overview of the microstructural aspects shared by both will now be discussed.

There exist three main types of bone cells, each with its own unique function: osteoblasts, osteocytes, and osteoclasts. One key feature of all of these cells is that none of them are capable of self-replication, meaning that they are all derived from the differentiation of precursor cells [15]. Osteoblasts, differentiated from mesenchymal stem cells, are responsible for the formation of new bone through the secretion of osteoid (predominantly type I collagen), and subsequent mineralization thereof. They also serve to manufacture hormones and several proteins, producing large quantities of alkaline phosphatase [15,16]. As a result of their role, osteoblasts are mainly found at the periphery of newly forming bone tissue (periosteum and endosteum) or defect locations [15]. As bone deposition occurs, some osteoblasts inevitably become trapped within channels (lacunae) in the newly-formed tissue, these then undergo alterations, transforming into osteocytes. These cells, comprising up to 95% of all bone cells, form dendritic extensions between each other through small channels (canaliculi) which also serve to allow for nutrient transport [17,18]. Thanks to their internal location and high inter-connectivity, osteocytes work to regulate mineral concentrations within bone via the secretion of numerous enzymes while concurrently regulating bone formation and

maintenance via the signaling of osteoblasts and osteoclasts [15–17]. Completely different from osteoblasts and osteocytes are the osteoclasts. These polynucleated cells, originating from hematopoietic stem cells, resorb bone previously deposited by osteoblasts [19,20]. In this capacity, osteoclasts work alongside osteoblasts to continuously remodel existing bone and heal bone defects [12]. As such, osteoclasts are also predominantly located at the surface of bones or at defect locations requiring resorption and remodeling [15]. **Table 2,** below, summarizes these different bone cell types.

	Progenitor Cells	**Predominant Location**	**Key Phenotypic Features**	**Major Functions**
Osteoblasts	Mesenchymal stem cells	Bone surface Defect sites	Cuboidal	Osteoid formation Mineral deposition
Osteocytes	Osteoblasts	Bone interior, Lacunae	Dendritic extensions	Mineral regulation Remodeling regulation
Osteoclasts	Hematopoietic stem cells	Bone surface, Defect sites	Poly-nucleated	Bone resorption

Table 2. Types of Bone Cells
The three major types of differentiated bone cells fulfill very different roles, giving rise to their varied locations and features.

While cells comprise the living component of bone, giving rise to its adaptive and regenerative properties, they only account for a mere 2 – 5 % of bone by mass [12]. The remainder is composed of proteins (~25%), minerals (~70%), and water (~5%) [12,14,21]. **Figure 1**, below, details the relative amounts of the acellular components present in bone.

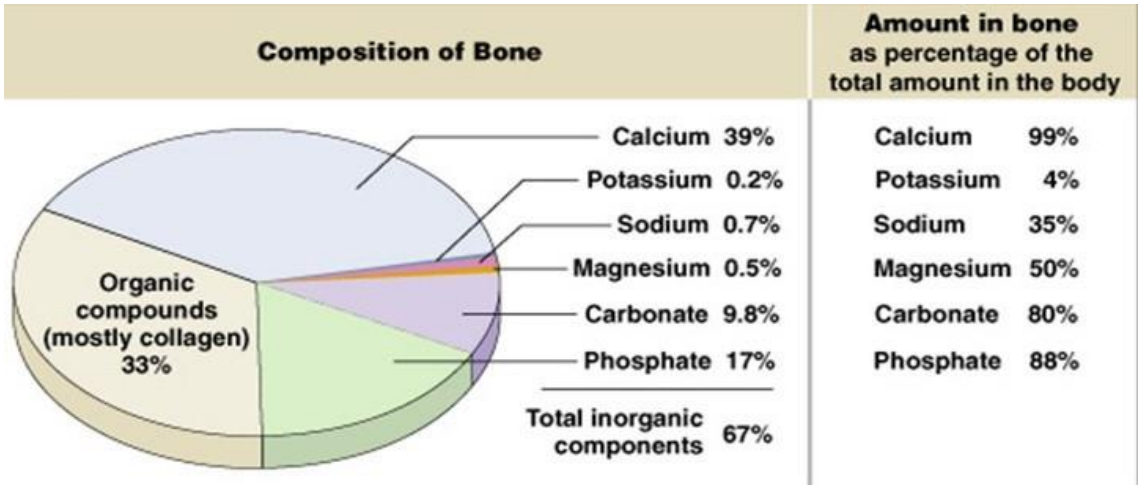

Figure 1. Acellular Composition of Bone
The main components of bone (percentage by mass). The amounts of each component relative to total amount of each within the average human are also provided, demonstrating the important regulatory/buffering function of bones. (Figure copied from [22]).

The main protein found in bone is collagen type I provides the structural framework of the osteoid, giving rise to the flexibility of bone [21,23,24]. Several other proteins, glycoproteins, and proteoglycans are also present in bone. The most abundant of these non-collagen proteins is bone Gla protein, also known as osteocalcin (BGP or OCN). This protein is specifically secreted by mature osteoblasts and osteocytes and is thought to have important roles in bone remodeling [23]. It mainly binds to calcium present in bone mineral, but is also present at lower levels in the extracellular fluid [24–26]. Another important protein present in bone is osteoprotegerin (OPG, also known as tumor necrosis factor receptor superfamily member 11b or osteoclast inhibitory factor). This soluble protein is secreted by both mesenchymal stem cells and osteoblasts and functions mainly as an inhibitor of osteoclast maturation and activity [27–30]. The main glycoproteins found in bone include bone sialoproteins, osteonectin, alkaline phosphatase (ALP), and the bone morphogenetic proteins (BMPs). The first two of

these are important in directing the attachment of bone mineral to bone collagen, ALP aids in the regulation of phosphate levels and mineralization (and is often used as a marker for the presence of bone), and several BMPs are known for their osteoinductive properties [24–26]. Finally, the bone proteoglycans have been shown to play significant roles in mineralization of osteoid. They are thought to serve as spacers in newly-formed collagen matrix, being later cleaved to allow for mineral deposition [24–26].

The inorganic mineral component makes up the most significant portion of bone. This consists mainly of calcium, phosphate and carbonate with small percentages of potassium, sodium, and magnesium [22,23]. The predominant mineral structure is in the form of hydroxyapatite, $Ca_{10}(PO_4)_6(OH)_2$, crystals no larger than approximately 20-40 nm in any dimension (**Figure 2**, below, shows the unit cell for crystalline hydroxyapatite) [21,23]. This crystal structure is not perfectly crystalline, containing many carbonate substitutions and being interlaced with other crystalline forms of calcium phosphate [21,23]. It is this crystal component that gives rise to the rigidity of bone and its mineral regulatory/buffering capabilities [21,23].

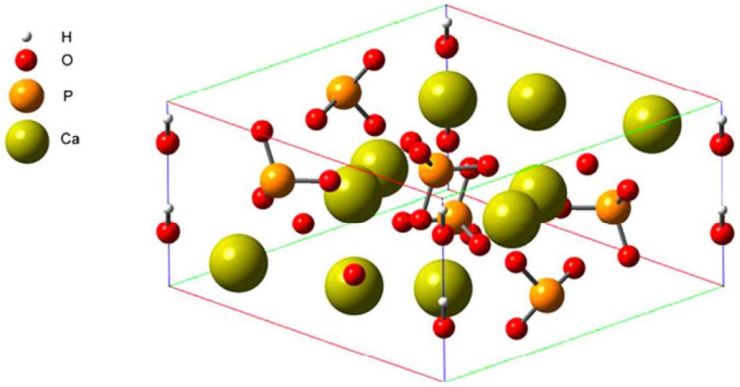

Figure 2. Structure of Hydroxyapatite
Hydroxyapatite, the main component of bone, is a crystalline structure with the unit cell depicted. Note: the eight hydroxyl groups present on the vertical edges of the unit cell are depicted in full, though only one quarter of each is actually contained within the unit cell. (Figure copied from [31]).

1.2.3 Structure of Bone

Bone tissue is traditionally classified into two different categories based on its porosity and architecture. The first of these, characterized by higher density and more parallel alignment is cortical bone (also called dense or compact bone). With a porosity typically between 5 and 10%, cortical bone provides rigidity and tensile strength for the shaft of long bones, and the outer shell of most other bones [14,32]. The structure of compact bone is highly organized, consisting of longitudinal osteons each containing a central Haversian canal surrounded by concentric lamellae [33]. Osteocytes are contained within lacunae between these concentric lamellar rings, with small interconnected channels of canaliculi [33]. Together, the Haversian canals and canaliculi provide a vessel network for the transport of nutrients and signaling molecules.

The other type of bone tissue, cancellous bone (also called spongy or trabecular bone) maintains a porosity usually ranging from 75 to 95% [32]. It consists of numerous seemingly-randomly organized trabecular plates, creating small cavities inside of which red bone marrow is contained [33]. The organization of these trabeculae, however, is not random, rather they are arranged along the main stress lines in a bone, providing structural support against stresses and strains [33].As a result, cancellous bone is found predominately in high-stress regions of bones such as the epiphyses of long bones and the bulk of the interior of vertebrae and flat bones [32]. **Figure 3**, below, demonstrates the organization of both cortical and trabecular bone tissues within a long bone.

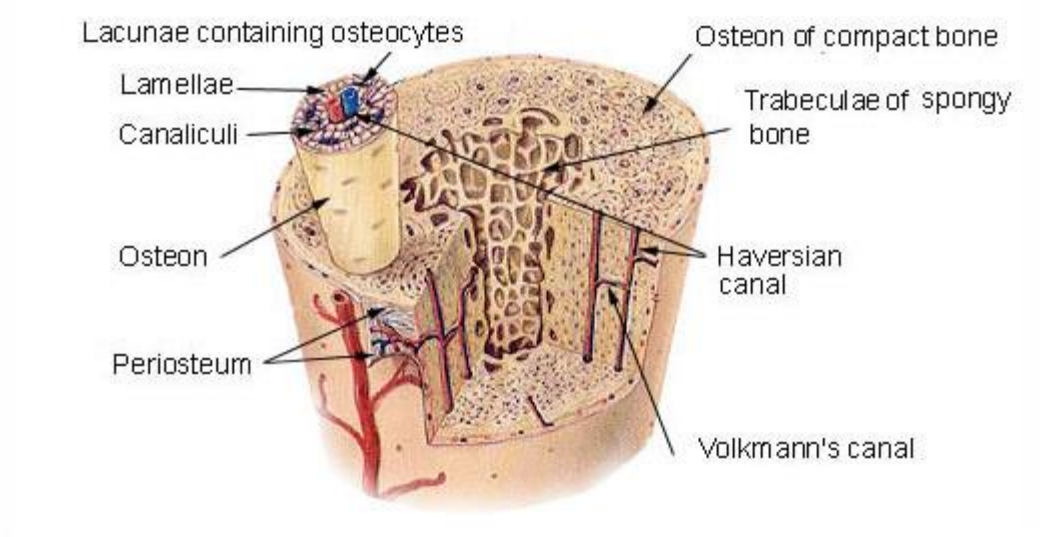

Figure 3. Structural Organization of Long Bone
A typical long bone is composed of cancellous (spongy) bone in the interior (filled with red bone marrow) surrounded by a shell of cortical (compact) bone. (Figure copied from [33]).

1.2.4 Bone Development, Growth, and Modeling

Bones begin to develop as a fetus and continue to grow into adulthood. The formation of new bone, or osteogenesis, occurs via the replacement of other tissues with bone tissue, a process called ossification (although the two terms are often mistakenly used interchangeably) [22]. This occurs via one of two different methods: intramembranous ossification or endochondral ossification. The former method, occurring mainly in flat bones, involves the infiltration of sheets of connective tissue formed within the fetus (the mesenchyme) [34–36]. This involves the direct differentiation of mesenchymal stem cells into osteoblasts, followed by the subsequent deposition of osteoid followed by the mineralization thereof, creating primary bone [34–36]. Endochondral ossification, in contrast, occurs within most of the bones of the skeleton [33]. In this process, mesenchymal stem cells first form a cartilage model for the bone to come; MSCs differentiate into cartilage and deposit cartilaginous extracellular matrix before inducing

apoptosis to allow for the infiltration of undifferentiated MSCs which subsequently differentiate into osteoblasts, replace the cartilaginous matrix with osteoid, and mineral said osteoid into primary bone [33–36]. **Figure 4**, below, demonstrates the process of endochondral ossification.

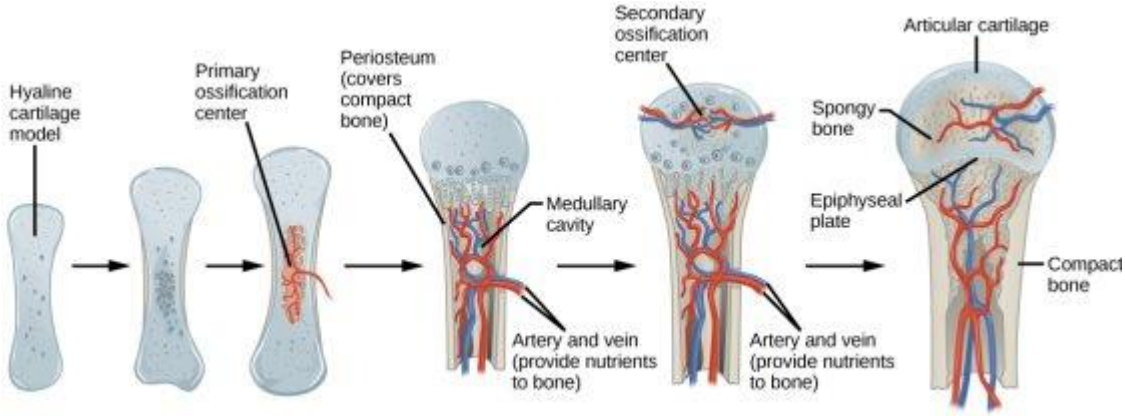

Figure 4. Endochondral Ossification Process
Endochondral ossification is the method by which most bones develop. A cartilage model of the bone-to-be is subsequently replaced by bone tissue. (Copied from [37]).

The continued growth of bones into adulthood occurs via a process similar to endochondral ossification. Occurring primarily in long bones, cartilage near the epiphyseal plate (growth plates, located at the metaphysis) continually proliferates and is continually ossified, thereby lengthening the bone into early adulthood [33,36]. Increases in the diameter of long bones (termed appositional growth) can continue on into later adulthood as a result of continued deposition of cortical bone at the periosteum (an outer layer of connective tissue encasing most bones) [33,36]. Continued growth (in length and diameter) of bones without concurrent modeling thereof would produce oddly-shaped, increasingly-heavier bones. To account for this, bone is continually modeled via the synchronized formation and resorption of bone on different surfaces [12]. In bone lengthening this is accomplished via the resorption of bone by osteoclasts at the

medullary cavity as the epiphyseal plate moves; in appositional growth this is accomplished via the resorption of bone at the endosteum (adjacent to the medullary cavity) as it is deposited at the periosteum [33,36]. It is important to note that the bone formation discussed in this section is all primary bone, also known as woven bone. This type of bone is characterized by its weak mechanical properties and disorganized arrangement of collagen [12,38]. Woven bone also contains more osteocytes per volume than does its more organized secondary (or lamellar) bone, and exhibits a much higher turnover rate (as it is remodeled relatively quickly into lamellar bone) [38]. The remodeling process is discussed in the next section.

1.2.5 Bone Remodeling and Repair

In order to produce the strong, highly-organized bone tissues introduced in **Section 1.2.3** from the weak, randomly-organized woven bone originally developed (as discussed in **Section 1.2.4**), it is obvious that some reorganization is required. The process by which this occurs is called remodeling which can be divided into 5 distinct phases. The first phase entails the stimulation and differentiation of pre-osteoclasts and their recruitment to the signaling area. Second, the osteoclasts resorb bone matrix in their local vicinity. Third, the osteoclasts are signaled to halt resorption. Fourth, osteoblasts are recruited to the area and begin to form and mineralize osteoid. Finally, some osteoblasts become trapped in the newly formed bone and transform into osteocytes while the remaining ones undergo quiescence and become inactive bone lining cells. This process occurs throughout one's entire life to continuously replace older, potentially weaker bone with newer, stronger bone in addition to allowing for

alterations in bone structure to compensate for changes in stress patterns and load requirements. It also aids in the homeostatic regulation of pH and mineral balances within bone as well as throughout the body. A diagram of this process is provided in **Figure 5**, below. [12,39,40]

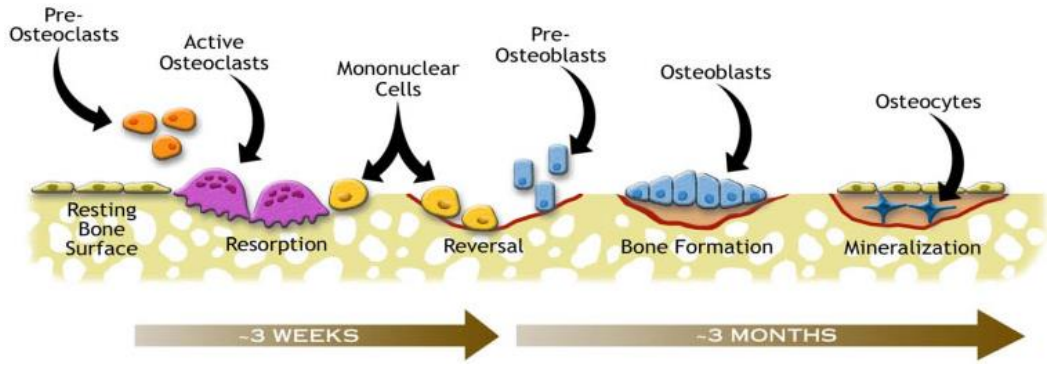

Figure 5. The Bone Remodeling Process
The five phases of bone remodeling are activation/recruitment of osteoclasts, resorption of bone matrix, reversal of osteoclast activation, formation of new bone, and mineralization of osteoid and quiescence of osteoblasts. (Copied from [39]).

While the remodeling of bone represents a continuous maintenance process, certain events can elicit a more drastic, immediate response. Any significant bone defect resulting in the exposure of internal bone matrix (such as a fracture, complete break, mass resection, etc.) will invoke the bone repair response. This process occurs in four main steps, and can take up to several months even years to complete depending on the location and degree of defect and other factors related to the person themselves (such as age, sex, medication, etc.) [41]. The first, immediate response is inflammation resulting in the formation of a protective hematoma around the defect site. This is followed by the formation of a fibrous callous within the hematoma via the infiltration of fibroblasts and mesenchymal stem cells into the area which secrete collagen fibers throughout. Next, in a process similar to endochondral ossification this fibrous callous is ossified into crude,

woven bone with the recruitment and differentiation of osteoblasts, osteoclasts, and osteocytes within the mineralizing matrix [12]. Up to this point approximately two months are required for the entire gap to be filled with new bone (depending on the factors mentioned earlier). Finally, this crude, weak bony callous is remodeled over the next several months to years until the bone regains is previous structure and strength. A diagram of this process is provided below, in **Figure 6**. [12,40–42]

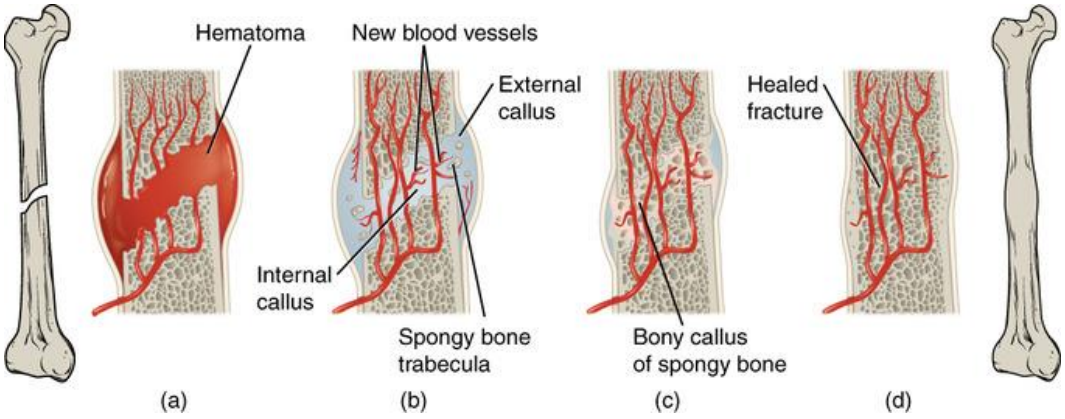

Figure 6. The Bone Repair Process
The process of bone repair can be described in four main steps: hematoma formation (a), soft callous formation (b), ossification of soft callous (c), and bone remodeling (d). (Figure copied from [40]).

1.2.6 The Metabolism of Bone Cells

The metabolic profiles of different bone cells can vary greatly due to their varied roles and locations within bone. This section will discuss the metabolism of those bone cells belonging to the mesenchymal lineage, namely mesenchymal stem cells, osteoblasts, and osteocytes (as these are the relevant cells to the project discussed herein). Mesenchymal stem cells, normally residing within an hypoxic environment *in vivo* (deep within the red marrow of bones), have been shown to metabolize predominately through glycolysis, though they do still utilize low levels of oxidative phosphorylation

[43–48]. Even when cultured *in vitro* in a more oxygen rich environment, MSCs have still been shown to favor glycolysis, though potentially exhibiting more oxidative phosphorylation that those cultured in hypoxic environments [43,44]. This high glycolytic metabolism is consistent with the Warburg effect as has been reported for cells adapted to living in hypoxic conditions *in vivo* [44].

Osteoblasts, typically present in regions of bone with higher oxygen levels, have been shown to have increased oxygen consumption rates compared with their progenitor MSCs [43,46,49,50]. This has been shown to be the result of a shift in metabolic profile from glycolysis-dominated to a decreased reliance on glycolysis coupled with an increased utilization of more efficient oxidative phosphorylation [43,46,49]. Moreover, MSCs cultured *in vitro* under hypoxic conditions have demonstrated a decreased capacity for osteogenic differentiation, perhaps due to their commitment along a chondrogenic pathway [43,44]. Chen et al. hypothesize that this transition from a metabolism dominated by glycolysis in MSCs to one with a significant contribution from oxidative phosphorylation in osteoblasts is permitted by the concurrent upregulation in antioxidant enzymes during osteogenic differentiation [46]. As a result, osteoblasts have the cellular machinery that permits them to reduce reactive oxygen species produced via oxidative phosphorylation, allowing them to benefit from this more efficient pathway [46].

Osteocytes, located deep within highly-mineralized tissue, have been shown in limited studies to exhibit much lower oxygen uptake rates than their osteoblast progenitors [51]. Although few studies have been published on the subject, the literature tends to suggest a return to a more glycolytic metabolism [51–53]. Furthermore, some studies propose that hypoxia could potentially promote the differentiation of osteoblasts to osteocytes,

though this claim is not well substantiated as of yet [52,53]. **Figure 7**, below, summarizes the metabolic changes accompanying the differentiation of MSCs to osteoblasts (and chondroblasts). **Table 3**, below, summarized the effect of oxygen tension on MSCs and osteoblasts.

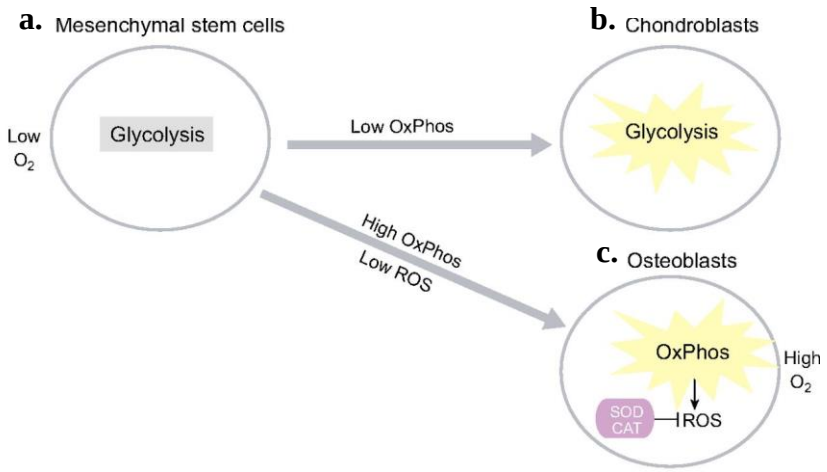

Figure 7. Metabolic Changes During MSC Differentiation
Mesenchymal stem cells, present in a low oxygen environment in vivo, metabolize predominately through glycolysis (a.). If maintained within a hypoxic environment they differentiate preferentially into chondroblasts (b.). In the presence of higher oxygen levels, they preferentially differentiate into osteoblasts which can derive energy much more efficiently through the use of oxidative phosphorylation (c.). The resulting effect is increased oxygen and decreased glucose consumption by osteoblasts as compared with MSCs. (Copied with modification from [43])

	MSCs	->	Osteoblasts
Hypoxia	Mainly glycolysis [43–45] Physiological ~4 - 7% O_2	Inhibited osteogenesis[43–46,54,55]	Inhibition of growth and mineralization[54,55]
Normoxia	Balance of glycolysis and OxPhos [43–46]	increased proliferative capacity [43–46]	Mainly OxPhos [43,46] with glycolysis

Table 3. Effect of Oxygen Tension on MSCs and Osteoblasts
Local oxygen concentration can greatly affect the metabolism, proliferation, and differentiation of MSCs and osteoblasts.

1.3 The (Bone) Tissue Engineering Approach

Tissue engineering has emerged over the past couple of decades as a multidisciplinary field aimed at the production of tissue substitutes predominately for regenerative medicine purposes. At its core, tissue engineering seeks to produce *de novo* tissue via the combination of cells, biomaterials, and biological factors, typically cultured in vitro within a bioreactor. The general approach entails the following steps: extraction of a stem cell rich sample from a patient, separation of the stem cells from the sample, deposition of these isolated stem cells onto a biomaterial scaffold, culture of this construct *in vitro* (typically in a bioreactor, with the addition of biological factors), and subsequent implantation of the engineered construct into the defect site within the patient. Each of these aspects as they relate to bone tissue engineering will be discussed in turn. **Figure 8**, below, summarizes the key aspects of the tissue engineering approach.

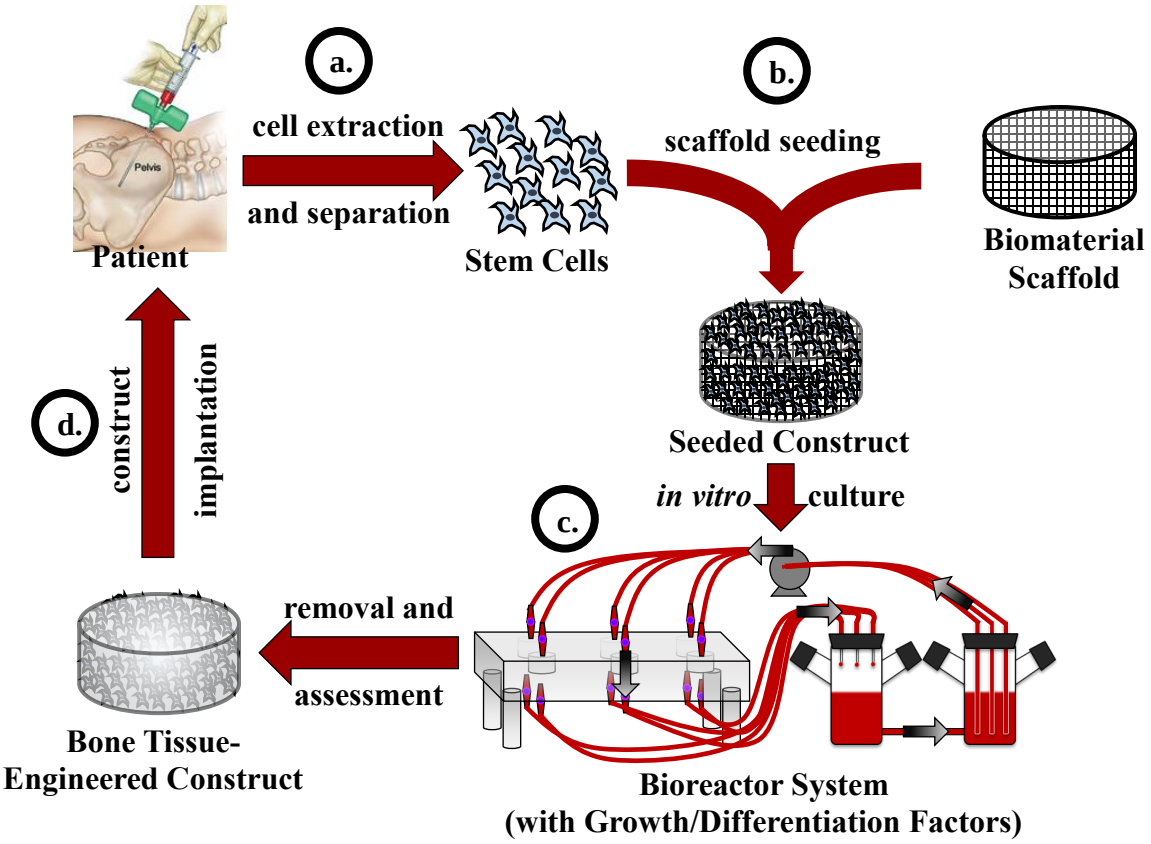

Figure 8. The Tissue Engineering Approach
The generalized tissue engineering approach entails the extraction, separation, and proliferation of stem cells from the patient (a.), the deposition of these cells within a biomaterial scaffold to produce a cell-seeded construct (b), the *in vitro* culture of this construct (typically within a bioreactor system with the addition of biological factors to promote the proliferation and differentiation of the stem cells within the construct) (c.), and the ultimate implantation of the resulting tissue engineered construct into the patient at the site of the defect requiring the graft (d.).

1.3.1 Cells

The first aspect of tissue engineering which separates it from other fields is its direct utilization of cells to aid in tissue (re)generation. For bone tissue engineering, a multitude of different osteogenic progenitor cells are used, each with its own benefits [2,56]. The most widely used of these is the bone marrow-derived mesenchymal stem cell (BM-MSC) due to its high degree of osteogenicity and well characterized nature [1,56,57]. Other cells implemented for bone tissue engineering thus far include adipose-derived

stem cells (ADSCs; as they are easy to extract and highly abundant), embryonic stem cells (ESCs; as they exhibit high pluripotency), umbilical cord blood mesenchymal stem cells(CB-MSCs), and as of late, induced pluripotent stem cells (iPSCs; as they are able to be produced following non-invasive fibroblast extraction) among others [1,56]. Each of these cell types comes with its own complications as well: BM-MSCs are not available in very large quantities, necessitating extensive *in vitro* expansion; ESCs are surrounded with legal and ethical controversy in addition to producing teratomas *in vivo*; iPSCs require extensive reprogramming and expansion and are accompanied with safety concerns as well; and ASCs and CB-MSCs are not well studied, necessitating further testing of their efficacy for bone tissue engineering [1,2,56,57]. No matter what cell type is used, the key characteristics desired by most include the ability to proliferate, differentiate into osteoblasts (and osteocytes), and secrete the appropriate matrix, proteins, and other signaling molecules required for proper tissue formation and incorporation [1,2,56]. Some researchers impose further demands of their cells, also requiring the potential for vascularization of their construct (typically through the co-culture of various cell types *in vitro* [1,2,56,58].

Based on their high degree of characterization, easy isolation and expansion, and well-established osteogenicity, bone marrow derived MSCs were selected as the cell of choice for the studies conducted herein.

1.3.2 Materials and Scaffolds

One field within the bioengineering domain which overlaps quite heavily with tissue engineering is that of biomaterials. This is a result of the necessity for a vehicle that

provides a framework for the development of a tissue engineered construct. The field of biomaterials, as of late, has proven a hotbed of activity for tissue engineering with research spanning from material development, characterization, and modification to scaffold design, production, and testing [1,2,58–61]. There exist numerous classes of biomaterials in use already, these include metals (aluminum, stainless steel, etc.), synthetic polymers (poly(lactic acid), poly(caprolactone), etc.), natural (bio)polymers (collagen, hyaluronic acid, etc.), and ceramics (hydroxyapatite, calcium phosphate, etc.) to name a few [1,2,58–61]. Furthermore, several composite/hybrid materials exist, comprised of two or more of these classes of materials combined in various ways [2,58–60].

The choice of biomaterial to use is only part of the process; further attention must also be given to the scaffold. Such considerations as scaffold size, shape, porosity, pore size, and rate of degradation (if applicable) must be made. Furthermore, the method of manufacture of said scaffolds comes into play, as many exist. Fabrication techniques span from particulate leaching, fiber meshing, molding, casting, and of particular interest recently are several additive manufacturing techniques [2,58,59]. Each method has its own advantages and disadvantages, such as the ability to tune porosity, the size and shape of the scaffold and its pores, scalability, speed, accuracy, and precision [2,59].

The end result of this vast selection process is the development of a scaffold exhibiting the desired characteristics. For bone tissue engineering these are generally defined as having a scaffold with high osteoconductivity, osteoinductivity, and biocompatibility; exhibiting properties similar to that of the target tissue (which even in bone tissue engineering can vary greatly depending on the target defect location) such as hardness, elasticity, porosity, pore size, alignment; and displaying degradation rates compatible

with (on the time-scale as) the expected tissue production rate of the implanted construct (allowing for the gradual replacement of the scaffold with native tissue) [1,2,58,59].

The biomaterial of choice selected for the experiments discussed herein was selected to be poly(L-lactic acid), for several reasons. First of all, it is a widely used material in the field of tissue engineering due to its biocompatibility, biodegradability, bioresorbability, and its already being an FDA approved material [62–64]. Furthermore, the hardness of PLLA is similar to that of bone, establishing it as an apt osteoconductive material [65,66].

1.3.3 Growth/Differentiation Factors

In addition to cells and biomaterial scaffolds, many employ the use of chemical stimulation to enhance the regenerative capabilities of tissue engineered constructs. For bone tissue engineering, most of these additives are implemented *in vivo* to promote the recruitment of native cells, their proliferation, differentiation, and secretion and mineralization of matrix, and the vascularization of the resultant *de novo* bone [1,59,61,67]. The most widely used of these include the classes of bone morphogenetic proteins (BMPs; predominately BMPs -2 and -7; to promote migration, proliferation, and differentiation), fibroblast growth factors (FGFs; to promote proliferation and differentiation), insulin-like growth factors (IGFs; to promote proliferation and matrix secretion), transforming growth factors (TGFs; to promote proliferation; the family to which most BMPs belong), and platelet-derived growth factors (PDGFs; to promote proliferation and matrix secretion) [1,59,61]. These are typically added just prior to the

implantation of a bone tissue engineered construct either directly onto the construct or in some encapsulated form to control the local release profile of said molecules [1,61,67]. More relevant to this study, some chemicals are added to *in vitro* cultures to assist the proliferation and/or differentiation of stem cells along an osteoblastic lineage. Some groups have utilized osteogenin, BMPs, and FGFs, while a majority of research involving the *in vitro* culture of bone tissue engineered constructs utilizes the smaller and cheaper molecules: dexamethasone, ascorbic acid, and β-glycerophosphate [68,69]. Dexamethasone, a synthetic corticosteroid not naturally present *in vivo*, has been found to promote the differentiation of stem cells into osteoblasts by acting as an agonist, binding to regulatory proteins (typically activated by natural glucocorticoids) which subsequently induce the transcription of osteoblastic genes [68,69]. Ascorbic acid (vitamin C) is thought to serve potentially many roles in aiding in osteogenesis. It has been shown to be important in collagen secretion for matrix formation by serving as a cofactor for the hydroxylation of pro-collagen, facilitating proper structuring of collagen [68,69]. Furthermore, ascorbic acid has antioxidant properties, providing a means for the reduction of reactive oxygen species produced via oxidative phosphorylation, the metabolic pathway highly utilized by osteoblasts [46]. The main roles of β-glycerophosphate in aiding in bone tissue engineering stem from its providing organic phosphates; the evolution of free phosphates serves to shift the balance of phosphates in solution which in turn provides a potential not only for mineral deposition (which then can further promote cell adhesion and differentiation) but also for the phosphorylation of key regulatory enzymes involved in the production of proteins expressed by osteoblasts [68,69].

The growth/differentiation factors selected for the experiments outlined herein include dexamethasone, ascorbic acid, and β-glycerophosphate due to their relatively cheap cost and extensive use within bone tissue engineering.

1.3.4 Bioreactor Systems

Although an approach does not necessitate the utilization of a bioreactor to be considered tissue engineering, most groups do employ their use. The primary purpose for the use of bioreactors is their introduction of a convective mode of transport through a construct, a phenomena which has a multitude of effects [2,70–72]. First of all, with respect to mass transport, the addition of a convective mode allows for the production and culture of much larger constructs which would otherwise be subject to severe diffusive limitations with regard to nutrient transport into, and byproduct transport out of, said construct [2,71,73]. Additionally, this allows for the mitigation (or, if desired, control) of otherwise potentially large gradients (of nutrients, byproducts, pH, cell signaling molecules, and even cell density) throughout the construct [2,71,73]. Furthermore, such added benefits as improved cell seeding, automation of culture, and facilitated monitoring can be realized [2,74].

Specifically for bone tissue engineering, the convective flow produced within a bioreactor has the added benefit of inducing shear stresses on the cells within (similar to their native environment) which has proven beneficial for the osteoinduction of osteogenic cells [2,71,73–75].

Several different bioreactor systems are employed in bone tissue engineering, with the most widely used being spinner flasks, rotating wall vessels, and perfusion systems [2,70–

[74]. The simplest bioreactor, the spinner flask, consist of constructs suspended in culture media which is circulated via a stir bar or impeller; such a system subjects constructs to non-uniform shear stresses and does little to mitigate internal gradients [2,72,73]. A step up in complexity is the rotating wall vessel, comprised of a chamber made from two concentric horizontally-oriented cylinders filled with media into which constructs are placed; originally developed by NASA, these bioreactors exhibit fairly uniform low shear stresses while acting to reduce diffusional limitations through the constructs in a continuous state of free-fall [2,70,72,73]. The most complex of these systems, the flow perfusion system, consists of constructs immobilized within chambers through which media is perfused; in this manner such systems provide for quite uniform shear stresses throughout the construct while allowing for the mitigation (and control) of gradients present within said constructs though they typically require highly porous constructs with high pore-interconnectivity [2,70,72,73,75]. **Figure 9**, below, provides a representation of each of the bioreactor systems discussed.

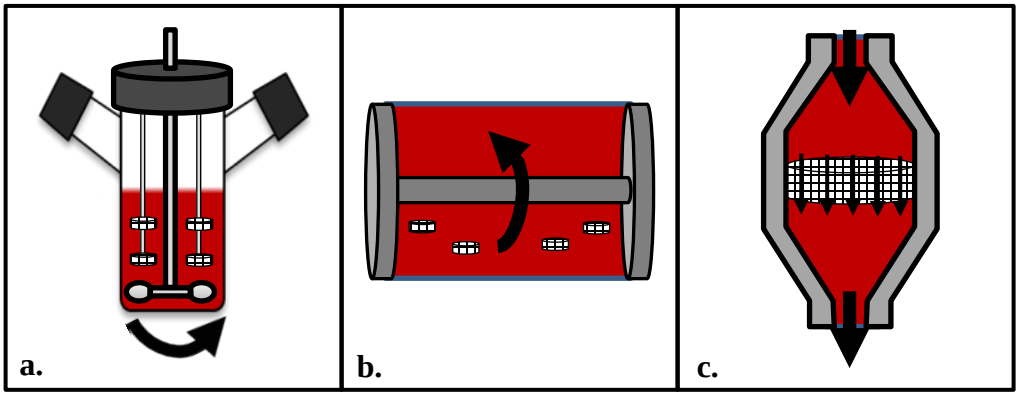

Figure 9. Bioreactor Systems for Bone Tissue Engineering
Common bioreactor systems for bone tissue engineering include the spinner flask (a.), rotating wall vessel (b.), and flow perfusion system (c.).

The bioreactor system selected for the experiments detailed herein was selected to be the flow perfusion system due to its uniform shear stress, mitigation of intra-construct gradients, and ease of implementing on-line monitoring systems.

1.4 FDA Regulations

One of the greatest hurdles faced by bone tissue engineering to date is that of obtaining approval from the US Food and Drug Administration (FDA) for the clinical use of bone tissue engineered constructs. Much of the complication in securing said clearance stems from the classification system utilized by the FDA in determining the appropriate regulatory pathway wherein medical products must be classified as either a drug, biologic, or device, each being regulated by a different center [76,77]. Due to the complex interplay involved in tissue engineered products, it is often difficult to place them into one of these categories. In order to facilitate the regulation of such combination products, the FDA established that "combination products" shall be classified according to their primary mode of action with drugs being assigned to the Center for Drug Evaluation and Research (CDER), biologics to the Center for Biologics Evaluation and Research (CBER), and devices to the Center for Devices and Radiological Health (CDRH) [76–79]. Even so, it is still often difficult to define the primary mode of action of tissue engineered constructs, though in general it seems that they will fall under the jurisdiction of CBER if it is asserted that the cells within the construct are the primary source of regeneration or potentially CDRH if it is found that the scaffold itself is the main contributor, although both these centers as well as CDER may become

cooperatively involved in the regulation of tissue engineered constructs [76]. Though each center involves navigating different regulatory pathways, several similarities exist [78]. Many tissue engineering applications (and certainly the project outlined herein) will most likely be regulated under the oversight of CBER, specifically under 21 CFR Part 1271: Human Cells, Tissues, and Cellular and Tissue-Based Products (HCT/Ps) [80]. This code establishes requirements for all aspects involved in the manufacture, distribution, reporting, and inspection of HCT/Ps [80,81]. Key among these requirements is Subpart D current good tissue practice (cGTP) which sets forth regulatory guidelines for methods, facilities, and controls for recovery, screening, testing, processing, storage, labelling, packaging, and distribution of HCT/Ps with the main purpose of preventing the introduction, transmission, or spread of communicable diseases [80]. Furthermore, oversight from CDRH will most likely also contribute to further regulations, namely 21 CFR 861: Procedures for performance standards development (for medical devices), aimed at the establishment of standards for the safety and effectiveness of a device [82]. These, among many other regulatory requirements must be met for a tissue engineered construct to achieve FDA clearance for clinical use. As such, it is important that the field begin to establish sound quality monitoring procedures to prove and ensure the safety and efficacy of tissue engineered constructs. It is one of the main objectives of the research presented herein to begin to establish said procedures, laying the groundwork for FDA approval of bone tissue engineered constructs.

1.5 Research Objectives

1.5.1 Hypothesis

The predominant hypothesis utilized in the development of the project outlined herein was that such aspects of bone tissue engineered constructs as quality, degree of differentiation, and confluency can be determined via non-destructive soluble analyte monitoring alone. Specifically, that trends in analyte rates of change (or ratios thereof) will allow for the determination of these aspects.

1.5.2 Objective 1: Production of Bone Tissue Engineered Constructs

The first objective sought by this project was to produce bone tissue engineered constructs via currently established methods (as outlined in **Materials and Methods, Section 2.1**). Additionally, baseline (non-osteoinduced) constructs were to be produced as a means of comparison. This objective was determined to have been achieved successfully based on the analyses employed in Objective 3.

1.5.3 Objective 2: Mid-Culture Construct Sampling and Monitoring

The second objective was to monitor key analytes during culture. Key analytes were first selected, then a means for their quantification was to be determined. Finally, said species were to be measured intermittently throughout culture in order to calculate rates of change of each. Both osteoinduced and non-osteoinduced constructs were to be monitored to allow for comparison and differentiation.

1.5.4 Objective 3: Post-Culture Construct Analyses

The third objective was to determine the above-mentioned construct aspects (quality, degree of differentiation, and confluency) from constructs sacrificed after different culture times. This was to be done using established methods (as outlined in **Materials and Methods, Sections 2.2.5 – 2.2.7**). Both osteoinduced and non-osteoinduced constructs were to be analyzed.

1.5.5 Objective 4: Development of Quality Monitoring Metrics

The final, and main objective of this project was to develop metrics or correlations for the real-time, non-destructive monitoring of *in vitro* bone tissue engineered constructs. This was to be accomplished via comparative analyses of the data collected in Objectives 2 and 3 for both the osteoinduced and non-osteoinduced constructs.

2. MATERIALS AND METHODS

2.1 Cell and Bioreactor Basics

2.1.1 Cell Extraction

The cells utilized within the experiments outlined herein were rat mesenchymal stem cells (rMSCs). The cells were extracted and isolated from the femurs and tibias of adult male Wistar rats approximately 6 weeks of age (175 – 199 g in mass; Envigo, previously Harlan Laboratories) utilizing established methods [83] as approved by the University of Oklahoma Institutional Animal Care and Use Committee (IACUC). Rats were asphyxiated one at a time in a sealed chamber with a rate of influx of CO_2 equal to 10% of the volume of the chamber per minute (the chamber was expelled of CO_2 between each rat to prevent premature asphyxiation). Immediately following confirmed death, the lower half of each rat was shaved, and the rats were submerged in 95% ethanol for 5-10 minutes to sterilize the exterior of each rat. Next, the skin along the legs was scrubbed with Triadine™, then 95% ethanol to further sterilize the area of interest. An incision was then made longitudinally from the hip to the ankle to allow for the excision of the femur and tibia, which were then carefully removed of all attached flesh and tendons. The patella was removed, and the two bones were separated before rinsing with cell culture media.

Rinsed tibias and femurs were then cut at the distal and proximal metaphyses, respectively. An 18-gauge needle attached to a 5 mL syringe filled with α-MEM (see next **Section 2.1.2** for details on α-MEM) was then inserted through the uncut epiphysis and metaphysis of each bone (the proximal epiphysis of the tibia and distal epiphysis of

the femur) into the diaphysis, wherein the bone marrow was subsequently flushed from the medullary cavity into a sterile 50 mL conical tube. The collective marrow from all specimens was then gently homogenized within the media, and split evenly into T75 cell-culture flasks (one flask per bone), which were then brought to a total volume of 10 mL with fresh α-MEM. Three days after the extraction, the media in the flasks was removed, the flasks were rinsed with PBS, and 10 mL of fresh α-MEM was added to each flask. This step was utilized as a means to remove any non-adherent cells also found within the extracted solution, such as hematopoietic stem cells and various blood cells. The remaining adherent cells constitute passage zero rMSCs.

2.1.2 Media

Two types of cell culture media were utilized in these experiments: basal α-MEM and Osteoinductive media. The α-Minimum Essential Media was prepared from powder (+ L-glutamine, - ribonucleosides and deoxyribonucleosides; gibco, Ref. # 12000-022). The reconstituted powder was pH adjusted to between 7.2 and 7.4 before being filter-sterilized with a 0.22 μm bottle-top vacuum filter (Corning; Ref. # 431097). This solution was then supplemented with 10% vol/vol fetal bovine serum (FBS; Atlanta Biologics; Cat. # S11150) and 1% vol/vol antibiotic-antimycotic (Gemini Bio-Products; Cat. # 400-101).

Osteoinductive media was prepared from the aforementioned α-MEM and further supplemented with 50 mg/L of L-ascorbic acid (Sigma; Ref. # A4544), 10 mM β-glycerophosphate (Sigma; Ref. # G5422), and 10 nM dexamethasone (Sigma; Ref. # D4902).

All media was prepared fresh at the start of each experiment and discarded immediately upon reaching a pH outside of the range of 7.2 – 7.4 or after one month of storage at 4 °C.

2.1.3 Cell Culture and Expansion

All cells were kept in an incubator set to 37 °C, 95% relative humidity, and supplemented with 5% CO_2. Up until such point as cells were seeded into a bioreactor, their media (only basal α-MEM was used during cell culture and expansion) was changed every Monday, Wednesday, and Friday until they reached a maximum of 80% confluency within a T-75 cell culture flask (Corning; Ref. # 430641U) (with the exception of the immediate post-extraction cell culture deviation as described in **Section 2.1.1**). Upon achieving 70 – 80% confluency, cells were passaged. Cells were first lifted from their flasks by removing the media from each flask, rinsing the flasks with 5 mL of Dulbecco's phosphate buffered saline (PBS; gibco; Ref. # 21600-010), removing the PBS, incubating the flask with 1 mL of Trypsin-EDTA (Sigma; Ref. # T4049), and removing the cells with excess α-MEM into a conical tube. This tube was then centrifuged at 1100 rcf for 5 min to pelletize the cells. The supernatant (containing α-MEM and trypsin) was removed, the cell pellet was homogenized into fresh α-MEM and subsequently fed into sterile T-75 flasks at a concentration of 250,000 – 333,000 cells per flask. Each flask was then brought to a total of 10 mL with fresh α-MEM.

2.1.4 Scaffolds

The scaffold utilized within these experiments were approximately 85% porous spunbonded poly(l-lactic acid) (PLLA; grade 6251D, 1.4% D-enantiomer, MW = 108,500, PDI = 1.87, NatureWorks LLC.) meshes approximately 5 mm in height and 8 mm in diameter.

Scaffolds were produced via the spunbonding process due to its many benefits. It is a simple, single unit operation amenable to fiber formation of myriad polymers in addition to being easily implementable from lab scale to full industrial scale processes [84–86]. Furthermore, the resulting highly porous scaffolds have immensely-interconnected pores. The spunbonding process consists of forcing molten polymer through a die and subsequently attenuating the resulting fiber by rapidly drawing it through an air venturi. The equipment setup was the same as that used in previous studies in the lab; consisting of a Brabender™ single screw extruder (19.1 mm diameter, 381 mm length, compression ratio of 3:1, maintained at 265 °C), a spin pack equipped with a Zenith™ gear pump (maintained at 275 °C), and a spinneret (0.42 mm inner diameter, 2.97 mm length, maintained at 280 °C). 100 cm below the spinneret, the fiber was attenuated in an air venturi [84]. A screen approximately 150 cm below the venturi was used to manually collect the attenuated fiber into random nonwoven layers. A diagram of this setup is provided in **Figure 10a**, below. Several sheets were stacked to obtain sheets of approximately 0.055 g / cm^2. These sheets were subsequently compressed to obtain a thickness of approximately 5 mm. The resulting porosity was determined to be approximately 85%, with fiber diameters of approximately 20 μm, and pores of approximately 250 μm in diameter (μCT images of the scaffold architecture are

provided in **Figure 10b**, below). Cylindrical plugs 8 mm in diameter were punched from these sheets to produce the final scaffolds for use in the bioreactor setup.

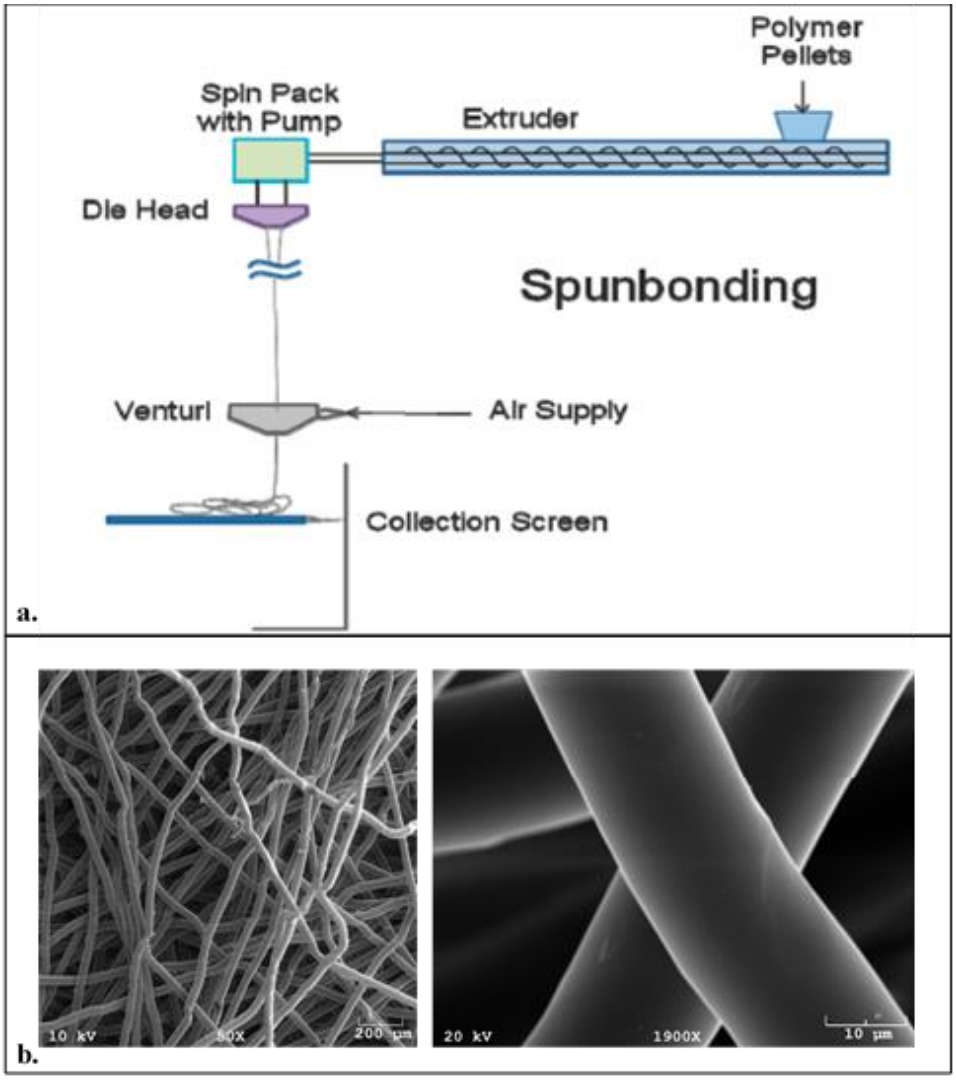

Figure 10. Spunbonding Process and Scaffolds
A diagram of the spunbonding process details the principle components (a., copied from [87]). SEM images of the spunbonded scaffolds used in the experiments conducted herein are provided at two different magnifications (b.).

2.1.5 Flow Perfusion Bioreactor System

The bioreactor system utilized for these experiments was based on the design by Bancroft, Sikavitsas, and Mikos [88]. The system comprises a main body connected with a reservoir system by tubing and a peristaltic pump. The body is composed of an acrylic

block approximately 1.5” in thickness containing six individual hollowed-out chambers allowing for one sample each. Into these chambers are placed cassettes with O-rings at the top and bottom of each. A scaffold is press-fit into each cassette to ensure snug, immovable positioning, requiring media flow to perfuse directly through the scaffold. A threaded top provides the means to seal each cassette into a chamber. Tubing adapters located at the top of each threaded top and the bottom of each chamber provide the means for attachment of 1/16” ID tubing (Cole-Parmer; Item# EW-96410-13). This tubing was selected as it is permeable to both O_2 and CO_2, allowing for both the re-oxygenation of media from the exit of each chamber until its re-entry and the facilitation of the buffering effect CO_2 has on the circulating media. Upon exiting the chambers, tubing directs the flow of media into one reservoir of a dual reservoir system. This effluent reservoir is attached to the feed reservoir by a small length of tubing connecting hollow glass barbs at the bottom of each reservoir. This provides the means for media recirculation, wherein the effluent media flows back into the feed reservoir before being fed via peristaltic pump (Langer Instruments; Model # BT100-1L) back into each scaffold chamber. It is important to note that each scaffold chamber has its own feed and effluent tubing (for a total of 12 tubing segments per bioreactor), all of which feed from (and deposit into) the globally-shared media reservoir system. Additionally, the system was equipped with oxygen sensing modules (see **Section 2.2.1** for details) placed immediately before and after each individual scaffold chamber. **Figure 11**, below, details the major components of the system.

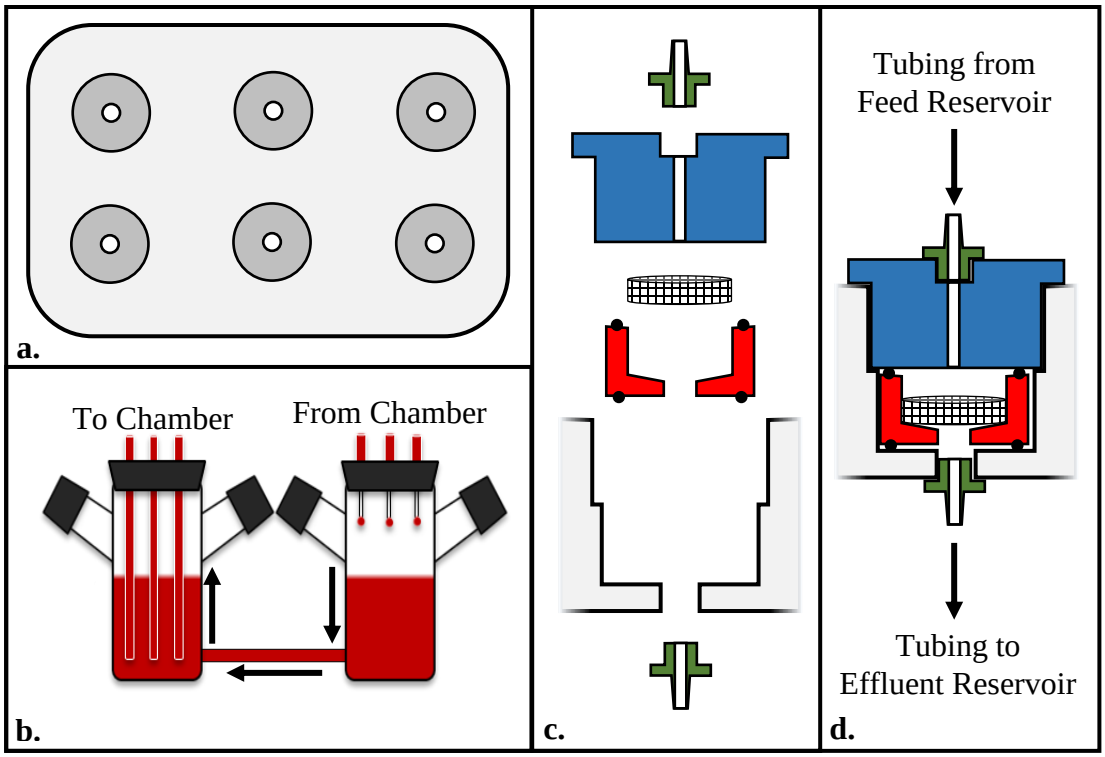

Figure 11. Key Components of Flow Perfusion Bioreactor System
The bioreactor system comprises an acrylic body (a.) which houses the reactor assemblies (c. and d.), a reservoir system (b.), oxygen permeable tubing (not depicted), and a peristaltic pump (not depicted). The body (a.) contains six individual chambers to allow for continuous culture of up to six constructs. The dual-bottle reservoir system (b.) allows for continuous recirculation of media throughout the bioreactor while further allowing for easy changing of media and quantification of flow rate. The reactor assemblies (provided in both an exploded and assembled view, c. and d., respectively) allow for the immobilization of, and forced media perfusion through, cultured constructs. These assemblies consist of two barbed tubing adapters (green), a threaded compression top (blue), and a cassette (red with black O-rings) into which a scaffold is placed, all housed within the reactor body (gray).

2.1.6 Pre-Seeding Scaffold Treatments

Prior to seeding, full liquid intrusion of the scaffolds was facilitated via a pre-wetting procedure [89]. Ensuring full liquid intrusion allows for more homogenous cellular intrusion into the scaffold and overall increased seeding efficiency [89]. The procedure consisted of submerging the scaffolds in 95% ethanol (due to its lower surface-tension than water) in a septum-sealed beaker and manually pulling a vacuum on the contents of

the beaker with a syringe. The low pressure environment produced by this method forces air contained within the scaffold to be displaced by the ethanol as observed by vapor bubble formation within and dissipation from the scaffolds. Vacuum was continuously pulled until such time as no more bubble evolution was observed. Next, the vacuum was released and the scaffolds were transferred to a beaker of PBS for a minimum of 30 minutes in order to displace the otherwise cytotoxic ethanol.

After pre-wetting, scaffolds were press-fit into cassettes which were then placed within the bioreactor chamber before closing the system. The pump was then turned on to allow media to circulate throughout the system and perfuse through the scaffold for a minimum of 1 hour prior to seeding. The reasons for this are two-fold: first to ensure there are no leaks within the system, and second to allow for protein attachment to the scaffold to facilitate cell attachment during seeding.

2.1.7 Dynamic Seeding

Scaffolds were dynamically seeded to promote better cell dispersion and homogeneity throughout the construct. This was accomplished by pipetting 150 µL of a cell suspension containing the desired concentration of cells (~2MM cells/150 µL) dispersed in α-MEM directly on top of the scaffold, closing the system, and beginning an oscillatory flow regimen. This regimen consisted of perfusing media through the scaffolds at a rate of 0.15 mL/min/scaffold in alternating directions with a period of one minute (i.e. one minute in forward, one minute in reverse, etc.) for one hour. After this oscillatory flow regimen, the flow was stopped, and the cells were allowed to attach to the scaffolds during a rest period of two hours. The flow was turned on in the forward

direction for the remainder of the experiment. Immediately following this rest phase, the entire volume of media within the system was replaced with fresh media (either osteoinductive media or α-MEM, depending on the group) in order to remove all unattached cells and prevent their accumulation elsewhere in the system. A diagram of this process is provided below, in **Figure 12**.

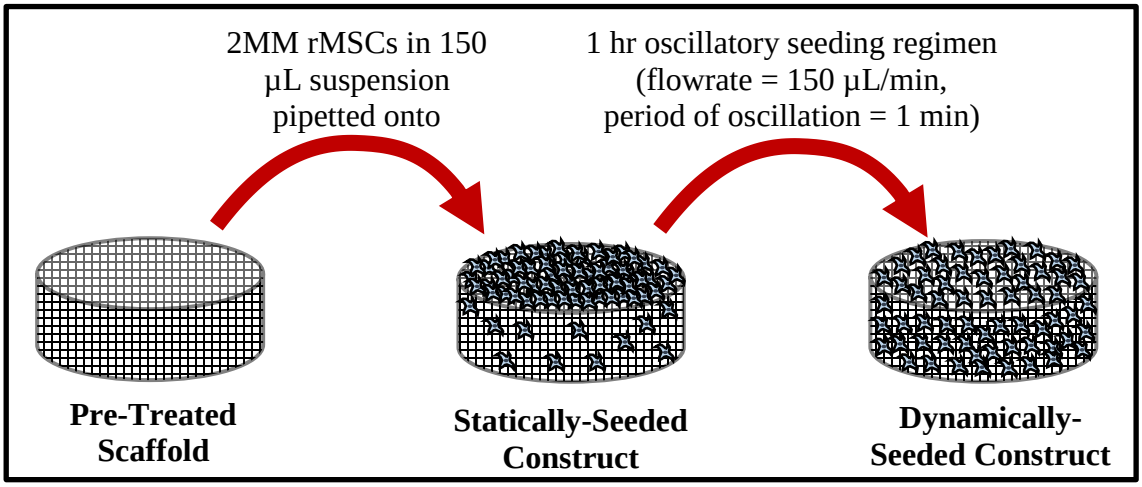

Figure 12. Dynamic Seeding Process
Scaffolds (having been pre-treated as described in **Section 2.1.6**) were seeded by first pipetting 2MM rMSCs onto each scaffold followed by one hour of oscillatory flow wherein media was perfused through each in alternating directions at a flowrate of 150 µL/min with a period of oscillation equal to one minute. This oscillatory (or dynamic) seeding regimen is utilized to produce a more homogenous distribution of cells throughout each scaffold (as demonstrated in the figure). After dynamic seeding, flow is then turned off for two hours to allow for cell attachment.

2.1.8 Replacing Media in Bioreactor System

The entire volume of media within the reactor was replaced every two or three days. This was accomplished by turning off the pump, suctioning out the entire volume of media contained within both reservoirs, clamping the segment of tubing between the reservoirs, filling the feed reservoir with the desired content of the desired media (set as

16.67 mL per active construct), turning the pump back on in the forward direction and allowing the system to run thusly for 20 minutes (calculated as the time required for the media within the feed reservoir to reach the effluent reservoir), removing the media accumulated in the effluent reservoir (as this was the old media still remaining in the tubing), removing the clamp between the reservoirs and returning the bioreactor to the incubator. Prior to being disposed of, the media accumulated in the effluent reservoir was measured, allowing for the calculation (and if required, recalibration) of the media flowrate through the system.

2.2 Species Measurement Methods

The numerous species investigated within this experiment were measured via various means. Some species were measured from construct samples (after sacrifice of said constructs) as a direct means for determination of certain properties (such as cellularity, mineralization, degree of differentiation, etc.) of the constructs following established methods. Constructs were sacrificed by removing them from their cassettes, tearing them apart into small segments, and placing said segments in 1 mL if nanopure water. Other species were measured from global media samples (taken immediately prior to each media change and frozen at -20 °C) as the basis for the establishment of an indirect means for the determination of such properties. As such, some of the quantified species provide construct-specific values while others are global values. Each species and the method of its measurement is discussed further below.

2.2.1 Oxygen

The dissolved oxygen content of the media was measured at the entrance to and exit from each individual construct-containing chamber of the bioreactor. It is important to note that the tubing used throughout the majority of the system was permeable to oxygen, and that a sufficient length of tubing was used such that full re-oxygenation of the media was achieved between the time it exited the scaffold-chamber and the time it re-entered a scaffold-chamber. Measurements were obtained with an optical dissolved oxygen probe system. The system used was a NeoFox Kit with RedEye® oxygen sensing patches, a system which measures the concentration of molecular oxygen without consuming it (Ocean Optics). RedEye® patches were affixed to the interior of custom-build oxygen sensing modules (referred to henceforth as OxyMods) which were then placed in line with the construct chambers, both before and after the chambers. A small segment of non-oxygen-permeable tubing was used to attach each OxyMod to the barbed tubing adapters on the bioreactor body (to prevent re-oxygenation of media between the measurement locations). **Figure 13**, below, shows the key components of the NeoFox system and the custom-built OxyMods.

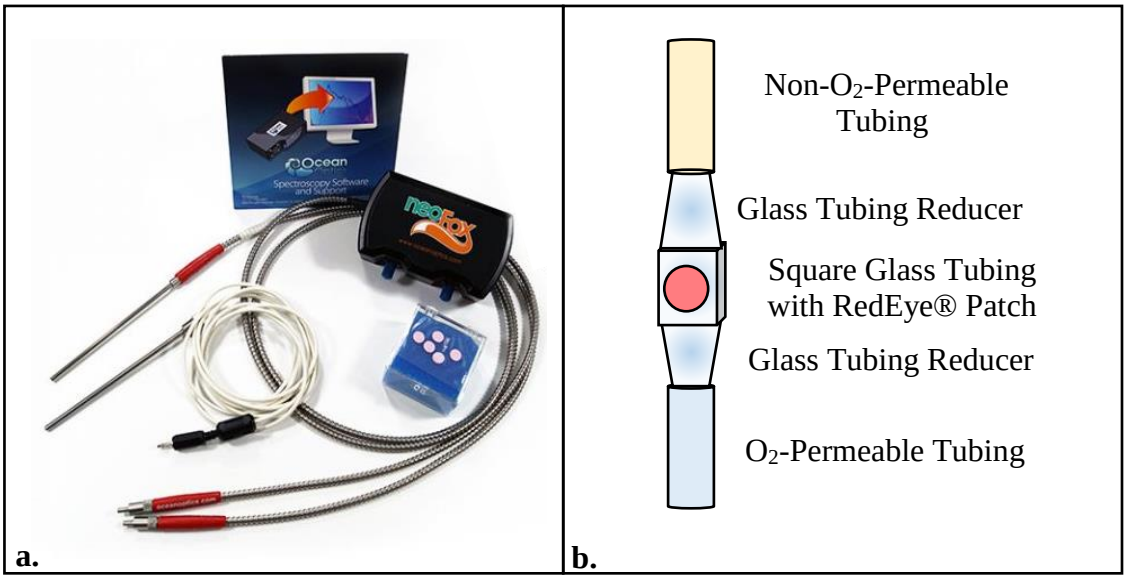

Figure 13. NeoFox System and OxyMods
The NeoFox Kit (a.) contains a phase fluorimeter, bifurcated fiber probe, thermistor probe, RedEye® patches, and NeoFow Viewer software. The RedEye® patches were affixed to the inside of custom-made OxyMods as seen in b.

The RedEye® patches contain a proprietary formulation of fluorescent organometallic molecules; the fluorescence of these molecules is quenched in the presence of O_2, proving the means for detection and quantification thereof. The system operates by emitting a blue light (as a 10 Hz pulsating square wave) through a fiber optic cable with a probe adapter which is held up to the patch; this blue light excites the fluorescent complex which then emits a responsive signal (of red light) which is subsequently read by a detector. The detector tracks the fluorescent decay profile, which is a function of the concentration of molecular oxygen. The signal from the detector is then analyzed by the NeoFox Viewer software package. It utilizes a Stern-Volmer equation to calculate the oxygen content as a function of the fluorescent decay as follows [90]:

$$\frac{F_0}{F} = \frac{\tau_0}{\tau} = 1 + k_q * \tau_0 * [O_2] = 1 + K_{SV} * [O_2] \quad \textbf{(Eqn. 1)}$$

Where F_0 = fluorescent intensity in absence of O_2

F = fluorescent intensity in presence of O_2

τ_0 = fluorescent decay time in absence of O_2

τ = fluorescent decay time in presence of O_2

k_q = bimolecular quenching constant

K_{SV} = Stern-Volmer constant for static decay

$[O_2]$ = concentration of molecular oxygen present at fluorophore

The RedEye® patches were supplied with pre-calibration files wherein the above constants were calculated over the entire operating temperature range (as they do vary with temperature). Initial calibration adjustments were performed prior to each bioreactor setup by using a single-point offset wherein pure water at 25 °C was set to 8.2 ppm. This built-in re-calibration method shifts all of the calculated values to correct for the signal loss through the glass. The effect of salinity on these readings was determined to be negligible, resulting in a less than 1% aberration from the uncorrected values. As the reading for each individual patch could vary slightly, at the start of each bioreactor setup initial pre-seeding oxygen measurements for each OxyMod were recorded to correct for these variations.

Oxygen measurements were obtained prior to each media change and/or construct sacrifice. Read values were allowed to level-off (after approximately 10 seconds of holding the probe in line with the RedEye® patch within an OxyMod) prior to recording values.

2.2.2 Glucose

Measurements of glucose were made on global media samples utilizing a GlucCell™ Glucose Monitoring System (CESCO BioProducts; Ref. # DG1000, **Figure 14**, below). This meter, though proprietary, most likely utilizes an enzymatic glucose oxidase reaction wherein glucose oxidase immobilized on test strips converts glucose in a sample to gluconic acid and hydrogen peroxide [91]. The hydrogen peroxide is then oxidized, releasing two electrons; the release of these electrons induces a current which is read by the sensor and converted (via internal calibrations) to a glucose concentration readout [91].

This meter has a test range of 1.6 – 33.3 mM, well beyond the 3.0 – 5.7 mM range for sample measurements. Samples were thawed and vortexed to ensure homogeneity. A 10 µL volume was suspended from a pipette tip then touched to the sample port on a new GlucCell™ test strip, allowing it to be pulled into the reaction chamber. All samples were run in triplicate.

Figure 14. GlucCell™ Glucose Monitoring System [92]
Glucose measurements were obtained with the GlucCell™ (CESCO BioProducts). The device is depicted along with two vails of test strips, three individual test strips, and a device tester.

2.2.3 Osteoprotegerin

Measurements of osteoprotegerin (OPG) were made on global media samples utilizing an enzyme-linked immunosorbent assay kit (ELISA; LifeSpan Biosciences, Inc.; Ref. # LS-F12843). The detection range of this assay is 15.6 – 1000 pg/mL.

This kit utilizes the sandwich ELISA principle wherein a sample is added to a 96-well plate coated with an immobilized capture antibody (in this case an anti-rat OPG antibody) to which the analyte of interest attaches (in this case, rat OPG). After washing the plate to remove unbound species, a biotinylated detection antibody (also anti-rat OPG) is added in solution to bind to the bound analyte of interest. Next, after a wash step, a solution of streptavidin-horseradish peroxidase enzyme complex is added, which then attaches to the biotin of any bound detection antibody. Then, after a wash step, a solution of 3,3′,5,5′-Tetramethylbenzidine (TMB) is added; this chromogenic substrate is oxidized by the HRP, turning the solution into a blue color. After a specific amount of time, the reaction is stopped with the addition of a sulfuric acid, which disrupts the enzyme and changes the solution to a yellow color, readable at 450 nm. A brief schematic of these steps is provided in **Figure 15**, below.

Running standards along with the samples of unknown concentration allows for the quantification of the analyte in these samples. Standard curves were fit to a sigmoidal 4-parameter logistic curve for proper determination of sample analyte concentrations. All samples and standards were run in duplicate per kit recommendation.

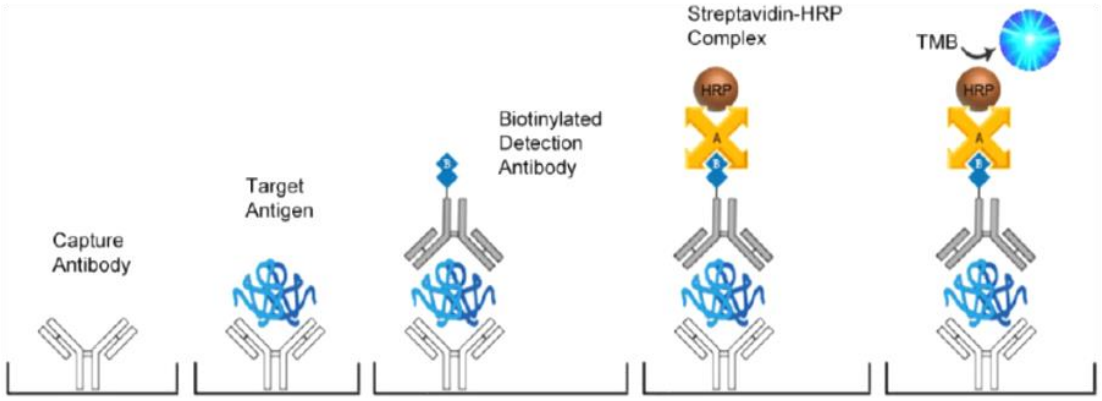

Figure 15. Pictographical representation of the sandwich ELISA principle [4]
A plate coated in the appropriate capture antibody (in this case anti-rat OPG) captures the target analyte present in a sample. To this bound analyte a second, biotinylated detect antibody (again, anti-rat OPG) subsequently binds. Next, streptavidin-conjugated horseradish peroxidase (HRP) is added, which binds to the biotin presenting on the detect antibody. Then, 3,3′,5,5′-Tetramethylbenzidine (TMB) is oxidized by the HRP to 3,3',5,5'-tetramethylbenzidine diimine (at a rate proportional to the concentration of the target antigen (rat OPG) present in the original sample). Finally, this reaction is stopped by the addition of sulfuric acid, and the plate is read at an absorbance wavelength of 450 nm.

2.2.4 Osteocalcin

Measurements of osteocalcin (OCN) were made on global media samples utilizing an enzyme-linked immunosorbent assay kit (ELISA; LifeSpan Biosciences, Inc.; Ref. # LS-F12230). The detection range of this assay is 62 – 4000 pg/mL. This kit utilizes the sandwich ELISA principle, see **Section 2.2.3**, above, for explanation. All samples and standards were run in duplicate per kit recommendation.

2.2.5 Cellularity (via dsDNA Quantification)

Measurements of double-stranded DNA (dsDNA) were made on the solution of constructs immersed in 1 mL of nanopure water and subjected to three freeze-thaw cycles wherein the constructs were sequentially frozen solid at -20 °C, thawed at 25 °C, and vortexed for 5 seconds prior to re-freezing. The resulting cell lysate was assayed for

dsDNA content utilizing a Quant-iT™ PicoGreen® dsDNA assay kit (Invitrogen; Cat. # P11496). The PicoGreen® reagent binds specifically to double-stranded DNA, providing the means for quantification. Standards over the range of the assay (0.1 – 3.0 µg/mL) were prepared with λ-DNA. 43 µL aliquots of all samples and standards were added to 257 µL of reaction mixture (10 mM Tris-HCl, 1 mM EDTA, 1.3 µL PicoGreen® reagent, pH 7.5) in an opaque 96-well plate and allowed to incubate for 5 min. The plate was then read on a Synergy HT microplate reader (Bio-Tek) for fluorescence with an excitation wavelength of 490 nm and an emission wavelength of 520 nm. The resulting intensity values were used along with the standard curve to quantify the concentration and ultimately content of dsDNA per sample. All samples and standards were run in triplicate.

The dsDNA content was then divided by the known dsDNA content per cell as obtained by performing the same assay on known quantities of cells cultured concurrently in T75 cell culture flasks and sacrificed at various time points (and counted prior to assay with a hemocytometer). NOTE: the dsDNA content of the cells was found to vary with time as the immature rMSCs differentiated into mature osteoblasts. This time-variable dsDNA content was used in the determination of cellularity, and is discussed further in the **Section 3.1.1**.

2.2.6 Alkaline Phosphatase Activity

Measurements of alkaline phosphatase (ALP) activity were made on the same cell lysate solution as that used for quantification of cellularity described above. These measurements were performed utilizing a fluorometric assay based on the enzymatic

conversion of p-nitrophenol phosphate (pNPP) to p-nitrophenol (pNP). Standards of pNP were prepared over the range of the assay (0 – 200 µM). 80 µL aliquots of each sample and standard were added to 20 µL of glycine buffer (0.1 M glycine, 1 mM $MgCl_2$, 1 mM $ZnCl_2$, pH 10.4) and 100 µL of substrate solution (1 mg/mL pNPP in glycine buffer) in a clear 96-well plate and allowed to incubate at 37 °C for 30 min before being stopped with the addition of 50 µL of stop solution (3.0 M NaOH). The plate was then read on a Synergy HT microplate reader (Bio-Tek) at an absorbance wavelength of 410 nm. The resulting absorbance values were used along with the standard curve to quantify the concentration of reacted pNPP and ultimately the activity of ALP in each sample. All samples and standards were run in triplicate.

2.2.7 Calcium

Measurements of calcium deposition were made on the same cell lysate solution as that used for quantification of cellularity and ALP activity described above after said assays were performed. The remaining cell lysate was diluted 1:1 with 1 M acetic acid and agitated overnight to solubilize deposited calcium. The resulting solution was then assayed for calcium content utilizing a calcium colorimetric assay (Sigma, Cat. # MAK022). Standards were prepared from $CaCl_2$ over the range of the assay (0 – 200 µg/mL). 10 µL aliquots of each sample and standard were added to 100 µL of buffer solution (500 mM 2-amino-2-methyl-1,3 propanediol) and 100 µL of binding reagent (o-cresolphtalein Complexone® and 0.024% 8-hydroxyquinoline) in a clear 96-well plate. The plate was then read on a Synergy HT microplate reader (Bio-Tek) at an absorbance wavelength of 575 nm. The resulting absorbance values were used along

with the standard curve to quantify the concentration and ultimately content of calcium in each sample. All samples and standards were run in triplicate.

2.3 Species Rate of Change Calculations

The aforementioned species concentrations were measured on samples obtained at specified (recorded) times. As such, the rate of change of each species was able to be calculated. The only exception to this is that for the concentration oxygen, whose rate of change is a direct function of flowrate (and an indirect function of time).

2.3.1 Oxygen Uptake Rate

A flowrate-dependent open-system mass balance on O_2 across each construct was derived to be:

$$\frac{dC_{O_2}}{d\tau} * V_{ch} * \epsilon = OUR_{construct} = N_{cells} * q_{O_2} \quad \textbf{(Eqn. 2a)}$$

Or, assuming zero-order kinetics for q_{O_2}:

$$\left(C_{O_2,out} - C_{O_2,in}\right) * \nu = OUR_{construct} \quad \textbf{(Eqn. 2b)}$$

$$= N_{cells} * q_{O_2} \quad \textbf{(Eqn. 2c)}$$

Where C_{O_2} = concentration of O_2 (subscripts "in" and "out" correspond to inlet and outlet of construct, respectively)

τ = residence time = $V_{ch} * \epsilon / \nu$

V_{ch} = volume of chamber

ϵ = porosity of construct

ν = volumetric flow rate of media through construct

$OUR_{construct}$ = construct oxygen uptake rate

N_{cells} = number of cells within each construct

q_{O_2} = cell-specific oxygen uptake rate

Utilizing these equations, $OUR_{construct}$ can be directly calculated in real-time during *in vitro* culture. If q_{O_2} (which may be a non-zero-order function of C_{O_2}, in particular observing Michaelis-Menten kinetics) is known, then N_{cells} can be directly calculated as well. q_{O_2}, however, is seen to be a function of more than just C_{O_2}, varying also with the degree of differentiation of the cells within the construct.

2.3.2 Glucose Consumption Rate

Due to the low cell-specific glucose consumption rate, a measurable decrease across each construct (as a function of flowrate) is not obtainable. As such, glucose consumption rates were measured as functions of time. Furthermore, due to the global media circulation system, all rates calculated from circulating media values are global-average values. Therefore, a global time-dependent closed-system mass balance on glucose was derived to be:

$$\frac{dC_{glc}}{dt} = -\frac{N_{cells}*N_{constructs}*q_{glc}}{V_{media,tot}} \quad \textbf{(Eqn. 3a)}$$

Or, assuming zero-order kinetics for $q_{glucose}$:

$$\frac{[C_{glc,0}-C_{\mathrm{glc},\Delta t}]}{\Delta t} = \frac{GCR_{global}}{V_{media,tot}} \quad \textbf{(Eqn. 3b)}$$

$$= \frac{N_{constructs}*GCR_{construct}}{V_{media,tot}} \quad \textbf{(Eqn. 3c)}$$

$$= \frac{N_{cells}*N_{constructs}*q_{glc}}{V_{media,tot}} \quad \textbf{(Eqn. 3d)}$$

Where C_{glc} = concentration of glucose (subscripts "0" and "Δt" correspond to time of media change and time of media sample, respectively)

$N_{constructs}$ = number of active constructs in bioreactor system

q_{glc} = cell-specific glucose consumption rate

$V_{media,tot}$ = total volume of media in bioreactor over time Δt

GCR_{global} = global glucose consumption rate

$GCR_{construct}$ = construct glucose consumption rate

Utilizing these equation, GCR_{global} and $GCR_{construct}$ can be directly calculated in real-time during *in vitro* culture. If q_{glc} (which may be a non-zero-order function of C_{glc}, in particular observing Michaelis-Menten kinetics) is known, then N_{cells} can be directly calculated as well. Similarly to oxygen, q_{glc} is seen to vary with the degree of differentiation of the cells within the construct, further complicating the analysis.

2.3.3 Osteoprotegerin Production Rate

The global time-dependent closed-system mass balance on osteoprotegerin is of the same form of that derived for glucose, **Eqn. 14a** (above), with the elimination of the "-" sign (as OPG is being produced, not consumed), such that:

$$\frac{dC_{OPG}}{dt} = \frac{N_{cells} * N_{constructs} * q_{OPG}}{V_{media,tot}} \quad \textbf{(Eqn. 4a)}$$

Again, assuming zero-order kinetics:

$$\frac{[C_{OPG,\Delta t} - C_{\mathrm{OPG},0}]}{\Delta t} = \frac{OPGPR_{global}}{V_{media,tot}} \quad \textbf{(Eqn. 4b)}$$

$$= \frac{N_{constructs} * OPGPR_{construct}}{V_{media,tot}} \quad \textbf{(Eqn. 4c)}$$

$$= \frac{N_{cells} * N_{constructs} * q_{OPG}}{V_{media,tot}} \quad \textbf{(Eqn. 4d)}$$

Where C_{OPG} = concentration of OPG (subscripts "0" and "Δt" correspond to time of media change and time of media sample, respectively)

q_{OPG} = cell-specific OPG production rate

$OPGPR_{global}$ = global OPG production rate

$OPGPR_{construct}$ = construct OPG production rate

Similarly to oxygen and glucose, $OPGPR_{global}$ and $OPGPR_{construct}$ can be calculated directly in real-time during *in vitro* culture. Furthermore, q_{OPG} is also seen to vary with the degree of differentiation of the cells within the construct.

3. RESULTS AND DISCUSSION

3.1 Post-Culture Construct Analyses

Although it might seem more appropriate to discuss the mid-culture analyses prior to discussion of the post-culture ones, the former data has no real significance without the latter. Overcoming this hurdle is indeed the purpose of the project herein, granting significance to these mid-culture analyses, circumventing the need to perform post-culture destructive analyses altogether.

3.1.1 Construct Cellularity Analysis

The first aspect of a construct determined via destructive, post-culture analysis was for cellularity (to ensure that cells were indeed present on the construct, and quantify their numbers for use in other analyses). As a dsDNA assay was used for this purpose, first the dsDNA content of each cell had to be determined. The resulting analysis showed this content to start at approximately 4.5 pg/cell for immature MSCs and steadily decrease to a value of approximately 2.5 pg/cell by day 14 for MSCs differentiating into osteoblasts. Over this time range (from day 0 to day 14), the cellularity of MSCs cultured in non-osteoinductive α-MEM was set at 4.5 pg/cell, while for differentiating MSCs the dsDNA content was calculated according to **Equation 5** as determined from experimental data (not shown).

$$m_{\frac{dsDNA}{cell}}(pg) = 4.5 - 0.0102 * t^2 \qquad \textbf{(Eqn. 5)}$$

Where t = culture time (in days)

This diminution in cellular dsDNA content can be attributed to the loss of proliferative ability by osteoblasts as compared with their progenitor MSCs. The resulting cellularity profiles for both the osteo-induced and non-osteoinduced reactors are provided in **Figures 16** and **17**, below (the difference between the two figures being the elimination of the Day 0 data points from both data sets, allowing for easier reading of later data points). Note: Day 0 refers to the amount of cells initially dispensed on top of each scaffold prior to initiation of the oscillatory seeding regimen.

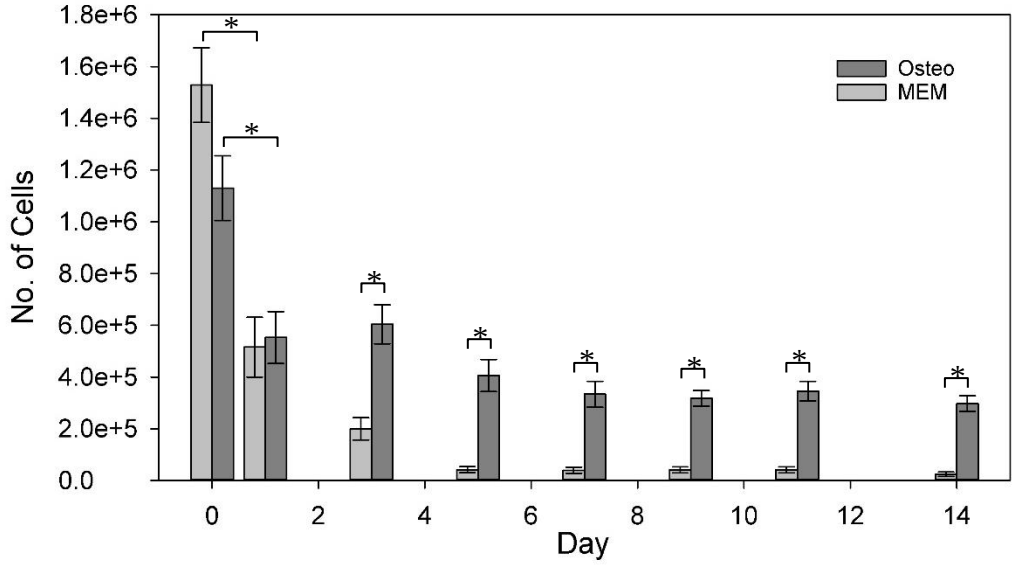

Figure 16. Construct Cellularity Day 0 – 14
The cellularity of the two data sets (osteoinduced constructs, "Osteo," in dark gray, non-osteoinduced, "MEM," in light gray) is seen to decrease and steady-off. The large decrease from Day 0 to Day 1 is typical, as Day 0 is the number of cells dispensed onto each construct prior to seeding, and Day 1 is the cellularity after one day being subjected to flow perfusion. The ratio of Day 1 to Day 0 is seeding efficiency, being 49% and 34% for the osteo- and non-osteo-induced constructs, respectively. Further analysis of the remaining data points available in **Figure 17**, below. Values are presented as mean ± SEM (N=4 for Osteo, 3 for MEM). Significance calculated via ANOVA with Tukey HSD Post-hoc analysis, "*" signifies $p < 0.05$.

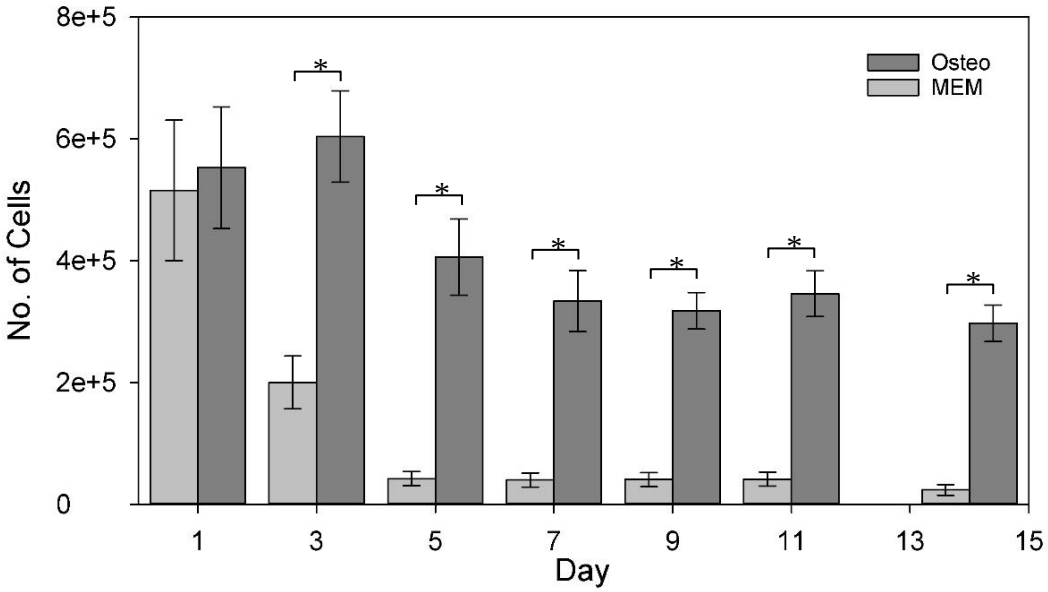

Figure 17. Construct Cellularity Day 1 – 14
The cellularity of the Osteo group is seen to level off to approximately 320,000 cells per construct by Day 5, while the MEM group levelled off to a much lower 40,000. This could potentially be due to increased binding affinity of the cells as they differentiate from MSCs (typically found in suspension within marrow *in vivo*) to osteoblasts (typically bound to osteoid *in vivo*). Values are presented as mean ± SEM (N=4 for Osteo, 3 for MEM). Significance calculated via ANOVA with Tukey HSD Post-hoc analysis, "*" signifies $p < 0.05$.

From the figures above, it is evident that the cellularity of the constructs levels off by Day 5, remaining fairly constant for the remainder of the experiment. Furthermore, it can be seen that the Osteo constructs maintained a significantly higher cellularity than the MEM ones. It is hypothesized that this is due to a potential higher affinity for attachment by osteoblastic-differentiating MSCs based on the fact that MSCs are typically found in solution *in vivo* within red bone marrow, being recruited and attaching to defect sites in the first step of their osteoinduction. It is important to note here, again, that both groups were seeded with non-osteoinductive media which was changed immediately after the seeding protocol with the respective media for each group.

3.1.2 Alkaline Phosphatase Activity Analysis

As has been mentioned previously, alkaline phosphatase (ALP) exhibits increased production in osteoblasts due to its importance in mineral deposition. As such, it is often used as an indicator of osteoblastic differentiation, as it is used herein. The figures below reveal the ALP activity per construct (**Figure 18**), and per cell (**Figure 19**).

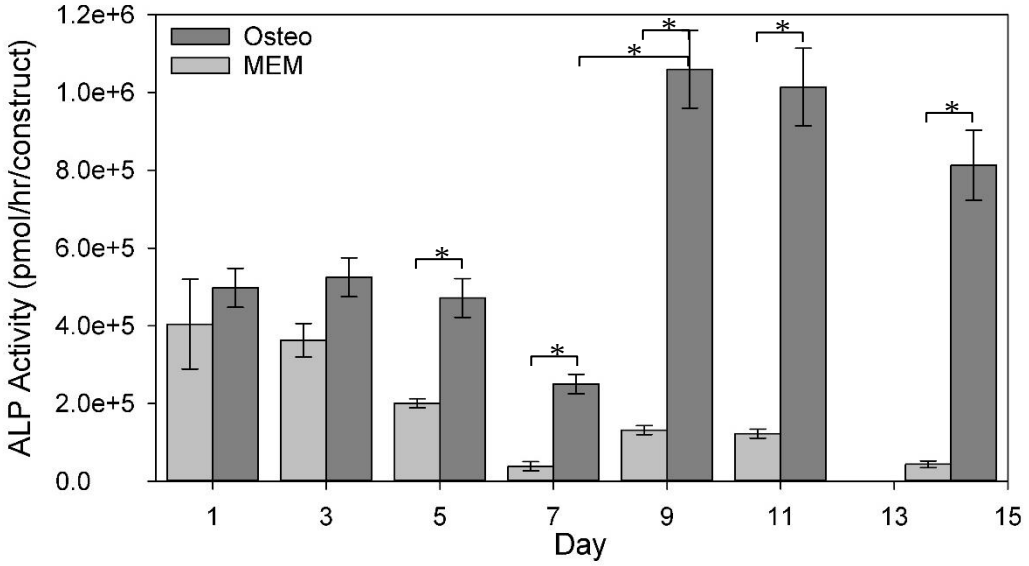

Figure 18. ALP Activity per Construct Day 1 – 14
A baseline level of ALP is seen to be expressed within the immature constructs as evinced by steady expression through Day 5. The activity level of alkaline phosphatase within each construct is seen to increase markedly between Days 7 and 9 for the Osteo group while remaining low in the MEM group. Values are presented as mean ± SEM (N=4 for Osteo, 3 for MEM). Significance calculated via ANOVA with Tukey HSD Post-hoc analysis, "*" signifies $p < 0.05$.

Due to the significant differences in cellularity between the two groups, a more apt analysis is provided by **Figure 19**, giving the ALP activity per cell. Nonetheless, both graphs demonstrate a significant increase in ALP activity from Day 7 to Day 9 for the Osteo group and no significant change for the MEM group. This observation serves as a primary indication of osteoblastic differentiation of the MSCs within the Osteo group, helping to validate that Objective 1 has been met.

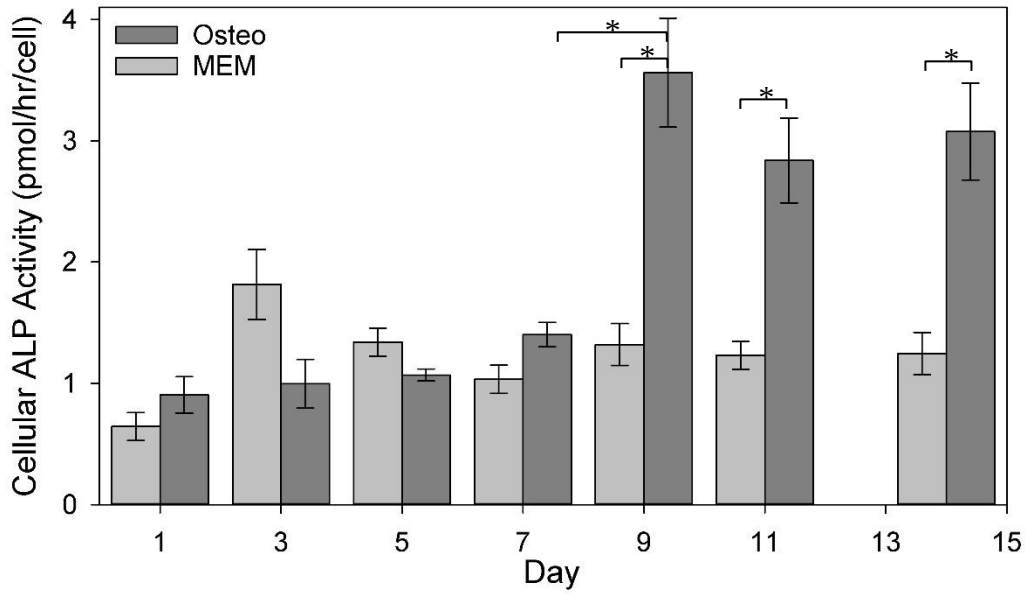

Figure 19. ALP Activity per Cell Day 1 – 14
A baseline level of ALP is seen to be expressed by immature MSCs as evinced by steady expression through Day 7. The activity level of alkaline phosphatase per cell is seen to increase markedly between Days 7 and 9 for the Osteo group while remaining at the baseline level in the MEM group. This result is a typical indication of osteoblastic differentiation. Values are presented as mean ± SEM (N=4 for Osteo, 3 for MEM). Significance calculated via ANOVA with Tukey HSD Post-hoc analysis, "*" signifies $p < 0.05$.

3.1.3 Calcium Deposition Analysis

Another key indicator of osteoblastic differentiation and bone formation is calcium deposition as secreting mineral (in the form of hydroxyapatite) is one of the main functions of osteoblasts. **Figure 20**, below, shows the calcium present within each construct over the culture period. A similar trend to that seen for ALP activity, above, is evident, with both groups exhibiting very low baseline levels of calcium (due to the presence of intracellular calcium), with a significant increase in calcium deposited from Day 7 to Day 9. Some of this difference can be explained by the differences in cellularity, though a majority of the difference is believed to be a result of the osteoinductive media differentiating the immature MSCs into osteoblasts.

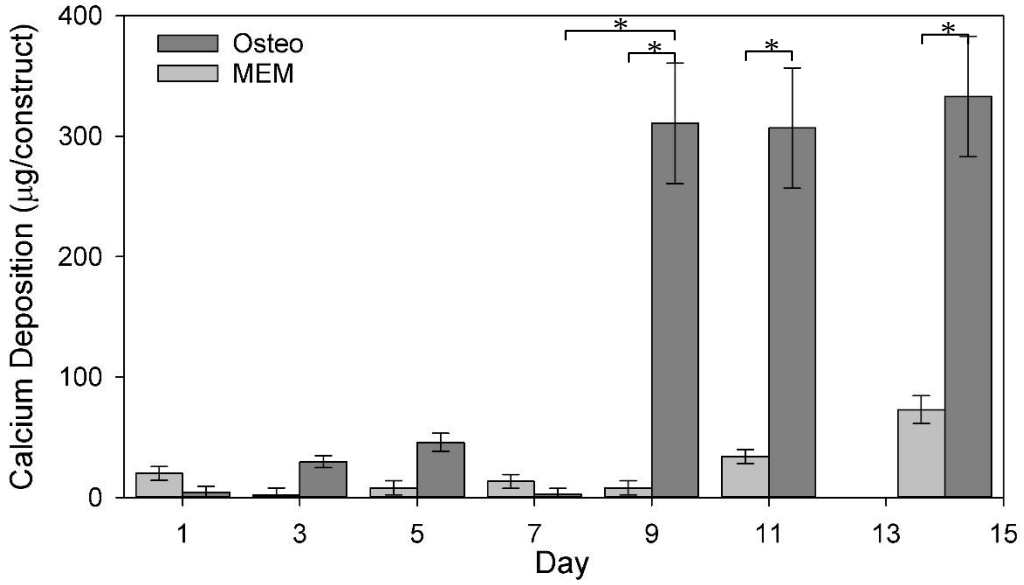

Figure 20. Calcium Deposition Within Construct Day 1 – 14
A low level of calcium is initially present within each scaffold, which can be attributed to intracellular calcium. A significant increase in calcium deposited within the construct between Day 7 and Day 9, a key indicator of osteoblastic differentiation and bone formation. Values are presented as mean ± SEM (N=4 for Osteo, 3 for MEM). Significance calculated via ANOVA with Tukey HSD Post-hoc analysis, "*" signifies $p < 0.05$.

3.1.4 Summary of Post-Culture Analyses

Overall, the above graphs exhibit several key trends. Firstly, the cellularity of constructs cultured in osteoinductive media are seen to have better cell attachment than those cultured in baseline non-osteoinductive media. Furthermore, the ALP activity and calcium deposition data support the conclusion that osteoinduced constructs demonstrate osteoblastic differentiation and "bone-like" formation as evinced by increases in both cell-specific ALP activity and total calcium deposited. These data support successful accomplishment of Objectives 1 and 3.

3.2 Mid-Culture Construct Monitoring

During culture, oxygen reading and media samples for glucose and OPG assay allow for the real-time monitoring the OUR, GCR, and OPGPR. The values obtained, however, may only be calculated on a global or per-construct basis without prior knowledge of the cellularity of the construct. Having determined the cellularity of the constructs over time already, it is now possible to calculate cell-specific rates of oxygen and glucose uptake and OPG production (although, again, such determinations cannot currently be made without the destruction of constructs to determine their cellularity without the development of monitoring metrics, to be discussed in Section 3.4).

3.2.1 Mid-Culture Oxygen Uptake Rates

Oxygen measurements taken throughout the entire culture period allowed for the quantification of the oxygen uptake rate per construct in real-time (see **Figure 21**).

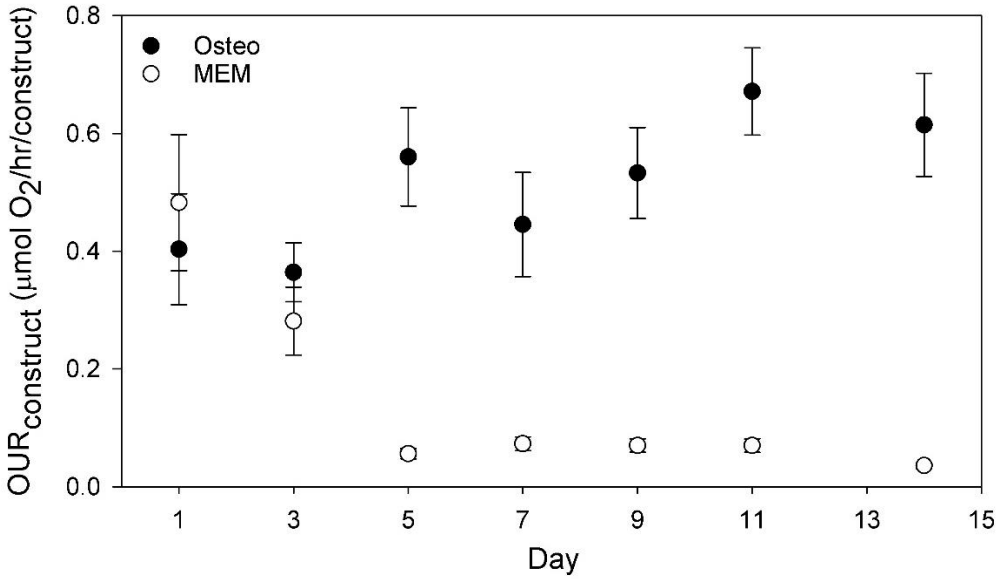

Figure 21. Construct OUR Day 1 – 14
The per-construct oxygen uptake rate (OUR) was calculated in real-time throughout the culture period. A fairly consistent (perhaps gradually increasing) OUR is observed for the Osteo group whereas a dramatic decline and leveling off is apparent for the MEM group. Values are presented as mean ± SEM (N=4 for Osteo, 3 for MEM).

The construct-specific OUR alone does not allow for reliable determination of construct quality, being itself a function of cellularity and cell-specific oxygen uptake rate (both of which can change throughout the culture period). If, however, one of these two variables are known, the other can be calculated. As such, with the cellularity over time having been discussed previously, the data in **Figure 21** can be divided by that in **Figure 17** to determine the much more informative cell-specific oxygen uptake rate, q_{O_2}, over time presented in **Figure 22**, below. It is important also to note that q_{O_2} is in fact expected to be a function of local oxygen concentration wherein lower values would be expected for the same cell present in a less oxygen-rich environment. As such, due to the decreased oxygen availability towards the exit of the construct, it can be expected than minor decreases in q_{O_2} may be exhibited by cells present within these less oxygen-rich environments. This effect, however, was mitigated within this study as the minimum oxygen tension measured at the construct effluent for any of the groups was not less than 86% of saturation. Still, **Figure 22** is presented as $q_{O_2,avg}$, the average cell-specific oxygen uptake rate throughout the construct.

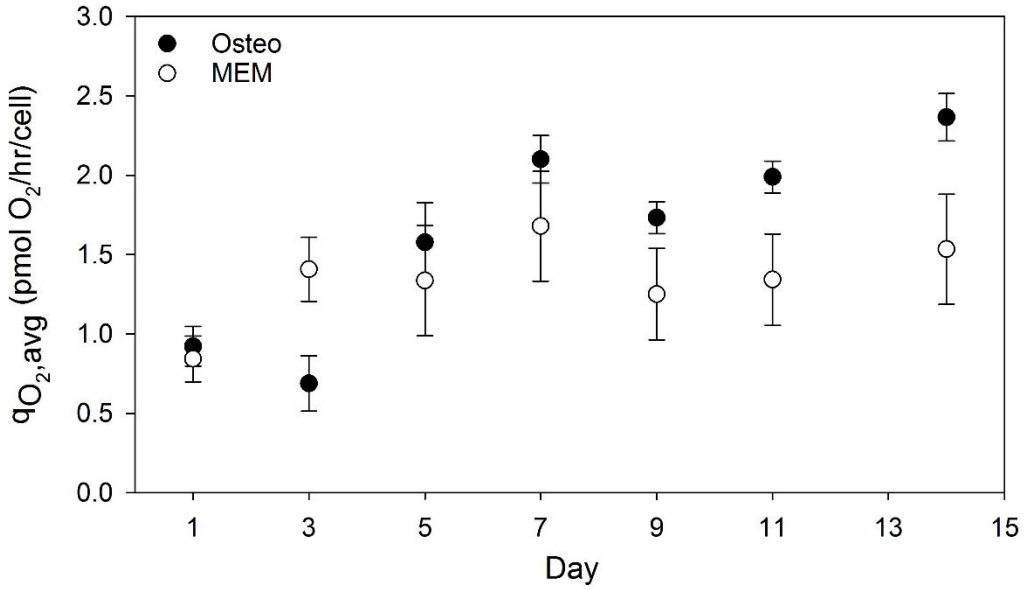

Figure 22. qO_2 Day 1 – 14
The average cell-specific oxygen uptake rate throughout the culture period was only able to be obtained after the destructive analysis of the construct to determine its cellularity. It can be seen that both groups start at the same $q_{O_2,avg}$, followed by a fairly steady value of approximately 1.4 pmol O_2/hr/cell for the MEM group and a potentially (though not significantly) increasing value up to a maximum at Day 14 of 2.4 pmol O_2/hr/cell for the Osteo group. This lack of significance between the values is heavily attributed to the large error in the MEM values at later time points due to lower limitations of the oxygen probe to detect differences at low cellularities. Values are presented as mean ± SEM (N=4 for Osteo, 3 for MEM).

The trends observed in **Figure 22** suggest an increase in the cell-specific oxygen uptake rate of osteoblasts (~2.4 pmol/hr/cell) as compared with immature MSCs (~1.4 pmol/hr/cell), a trend supported in the literature (see **Section 1.2.6**). Comparing the values obtained herein with literature values for the oxygen uptake rates of MSCs and osteoblasts, Pattappa et al. report a rate for human MSCs cultured under normoxia of ~98-119 fmol/hr/cell for [44,45]; Komarova et al. report values increasing from ~40 fmol/hr/cell to ~200 fmol/hr/cell for differentiation to rat osteoblasts [93]. It is important to note that these values were obtained for cells cultured on two-dimensional flasks,

providing a possible explanation for the approximately 10-20-fold higher oxygen uptake rates determined herein (cultured in 3D).

3.2.2 Mid-Culture Glucose Consumption Rates

Media samples obtained throughout the entire culture period allowed for the quantification of the glucose consumption rate per construct in real-time (**Figure 23**).

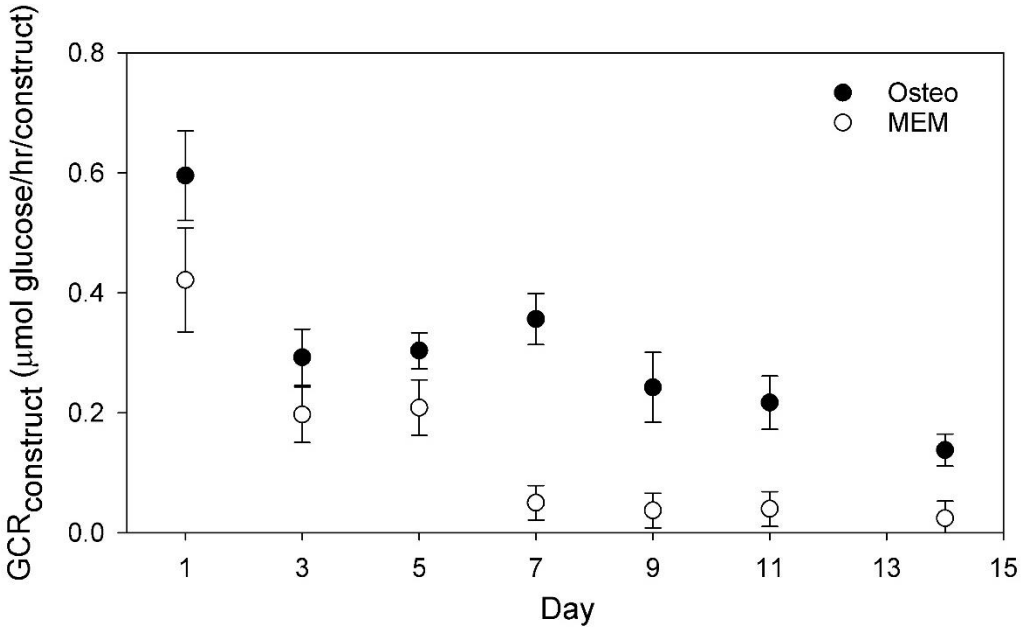

Figure 23. Construct GCR Day 1 – 14
The per-construct glucose consumption rate (GCR) was calculated in real-time throughout the culture period. Decreases over time are observed for both groups, with more dramatic declines for the MEM group. Values are presented as mean ± SEM (N=4 for Osteo, 3 for MEM).

As with the OUR, the construct-specific GCR alone does not allow for reliable determination of construct quality. As such, the cell-specific glucose consumption rate, q_{glc}, over time was calculated and is presented in **Figure 24**, below. Again, due to the decreasing glucose concentration throughout the culture period (between media changes), the values below are presented as $q_{glc,avg}$, the average cell-specific glucose

consumption rate over the time period between media changes. As with $q_{O_2,avg}$, the minimum glucose concentration (measured immediately prior to the change of media) was still fairly close to the starting concentration, at a maximum of an approximately 20% decrease from the starting value.

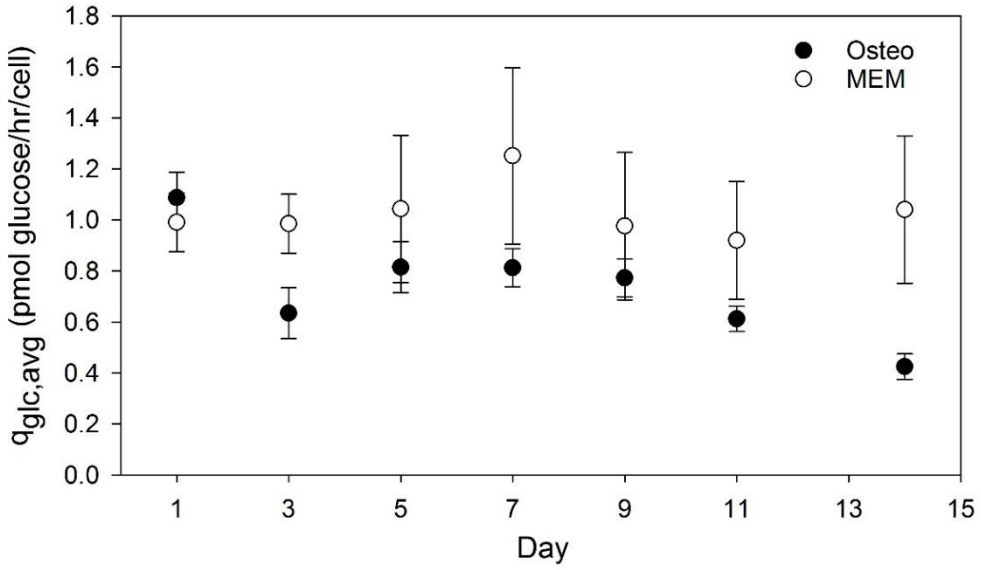

Figure 24. q_{glc} Day 1 – 14
The average cell-specific glucose consumption rate throughout the culture period was only able to be obtained after the destructive analysis of the construct to determine its cellularity. It can be seen that both groups start at the same $q_{glc,avg}$, followed by a fairly steady value of approximately 1.0 pmol glucose/hr/cell for the MEM group and a potentially (though not significantly) decreasing value down to a minimum at Day 14 of 0.4 pmol glucose/hr/cell for the Osteo group. This lack of significance between the values is heavily attributed to the large error in the MEM values at later time points due to accuracy limitations of the GlucCell™ meter to detect differences at low cellularities. Values are presented as mean ± SEM (N=4 for Osteo, 3 for MEM).

The trends observed in **Figure 24** suggest a decrease in the cell-specific glucose consumption rate of osteoblasts (~0.4 pmol/hr/cell = 400 fmol/hr/cell)) as compared with immature MSCs (~1.0 pmol/hr/cell = 1000 fmol/hr/cell), a trend supported in the literature (see **Section 1.2.6**). Literature values for the cell-specific glucose consumption rate of MSCs are available: Pattappa et al. report values of ~360 fmol/hr/cell and ~230 fmol/hr/cell for human MSCs [44,45]; dos Santos et al. report values

of ~540 fmol/hr/cell for human MSCs [94]; Schop et al. report values of ~250 fmol/hr/cell for rat MSCs [47]. Although the values determined herein are approximately 2-4 fold higher than those reported in the literature, this is still within fairly good agreement. Again it is important to note that these literature values were obtained for MSCs cultured in two-dimensions whereas this experiment cultured them in three-dimensions, potentially accounting for the some of the difference.

3.2.3 Mid-Culture OPG Production Rates

Media samples obtained throughout the entire culture period allowed for the quantification of the OPG production rate per construct (**Figure 25**); although not analyzed in real time, methods could be developed to allow for real-time measurement of OPG levels present within circulating media.

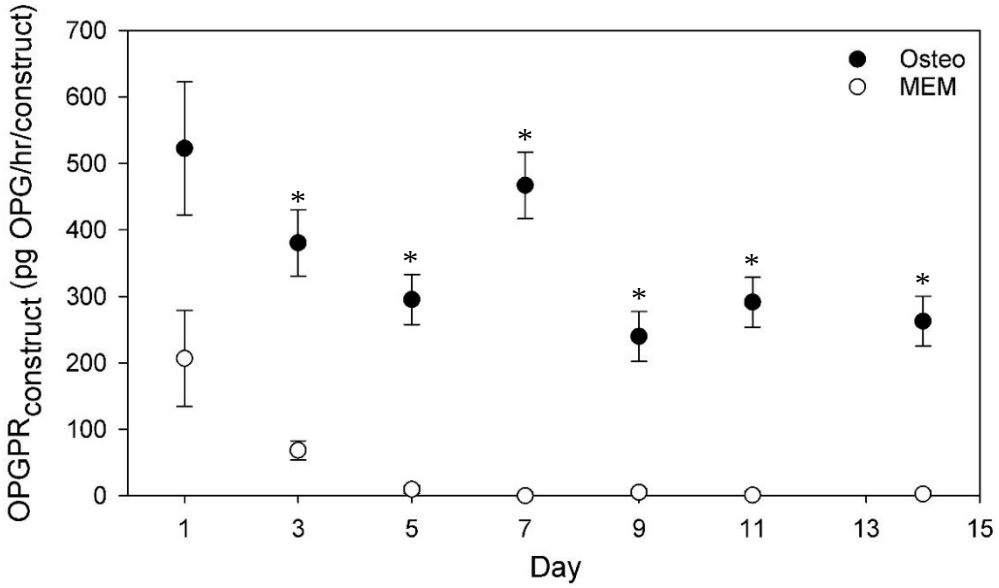

Figure 25. Construct OPGPR Day 1 – 14
The per-construct OPG production rate (OPGPR) was calculated from media samples collected throughout the culture period. Similar trends are observed for both groups, with an initial decrease to a constant value, although significantly higher values are seen for the Osteo group as compared with the MEM group for all time points except Day 1. Values are presented as mean ± SEM (N=4 for Osteo, 3 for MEM). Significance calculated via ANOVA with Tukey HSD Post-hoc analysis, "*" signifies $p < 0.05$.

As with the OUR and GCR, a plot of the cell-specific OPG production rate was produced in order to better understand the quality of each construct; said plot is provided as **Figure 26**, below.

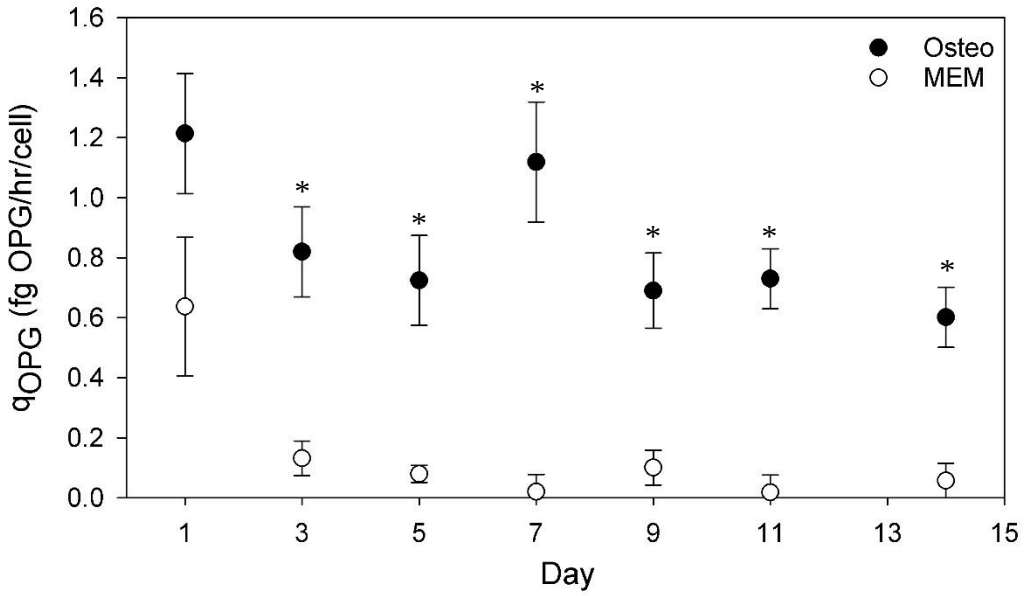

Figure 26. q_{OPG} Day 1 – 14
The cell-specific OPG production rate throughout the culture period was only able to be obtained after the destructive analysis of the construct to determine its cellularity. Both groups start out with similar values, though this is followed by a large decline to minimal values (~0.1 fg OPG/hr/cell) for the MEM group whereas the Osteo group maintains a fairly steady rate of OPG production (~0.7 fg OPG/hr/cell). Values are presented as mean ± SEM (N=4 for Osteo, 3 for MEM). Significance calculated via ANOVA with Tukey HSD Post-hoc analysis, "*" signifies $p < 0.05$.

The trends observed in **Figure 26** suggest OPG secretion by osteo-induced MSCs is maintained at a steady value (at least through 14 days of culture) whereas non-osteo-induced MSCs drastically decrease their production rates. Although no real literature values exist currently for OPG production rates by MSCs or osteoblasts, it is stated in the literature that MSCs express OPG constitutively, exhibiting increased expression through osteoblastic differentiation [28,29,95,96]. It is important to note that OPG, as a regulatory signaling molecule, may exhibit drastically different expression profiles

under different conditions. As such, the values obtained herein may prove valid only for the specific system utilized herein. Furthermore, the intermittent changing of media, resulting in the removal of accumulated OPG may well have influenced its secretion, which may have been otherwise decreased under conditions of high concentration of circulating OPG.

3.2.4 Mid-Culture Osteocalcin Detection

Although only at very low levels, osteocalcin was detected in media samples collected on Days 11 and 14 for the osteoinduced cultures, with none being detected at any time point for the non-osteoinduced cultures. This timing corresponds well with the ALP activity and calcium deposition trends, as well as the observed divergences in oxygen uptake and glucose consumption rate for osteoinduced cultures as compared with non-osteoinduced ones.

3.2.5 Summary of Mid-Culture Analyses

Overall, the graphs discussed above tend to suggest alterations in cellular oxygen uptake, glucose consumption, and OPG production rates as MSCs differentiate into osteoblasts. Decreasing glucose consumption along with concurrently increasing oxygen consumption suggests a shift in the metabolic profile from one more reliant on glycolysis to one benefiting more from oxidative phosphorylation, as supported by the literature (see **Section 1.2.6**). Furthermore, OPG production is seen to be maintained at a fairly constant level for the osteoinduced group while falling off rapidly for the non-osteoinduced group. Finally, osteocalcin secretion is noticed in minimally-detectible

quantities only at late time points (Days 11 and 14) for osteoinduced cultures only. The elucidation of these trends partially fulfills Objective 2. **Table 4**, below, summarizes the cell-specific rates determined above alongside the literature.

		Calculated Values (Day 14)	Literature Values	Reference
q_{O_2}**(fmol/hr/cell)**	MSC	1400 ± 600	100 ± 20 40 ± 10	44 93
	Osteoblast	2400 ± 300	200 ± 30	93
q_{glc}**(fmol/hr/cell)**	MSC	1000 ± 400	540 ± 80 250 ± 110	94 47
	Osteoblast	400 ± 100	-	-
q_{OPG}**(fg/hr/cell)**	MSC	0.1 ± 0.1	-	-
	Osteoblast	0.7 ± 0.2	-	-

Table 4. Summary of Cell-Specific Rates
Cell-specific rates calculated in this section compared with the literature (mean ± SD). Calculated values for MSC and osteoblast refer to Day 14 values for MEM and Osteo groups, respectively.

It is important to note that while the above table presents singular values for each rate, these are more appropriately termed average values, with cells in culture perhaps exhibiting varied rates as functions of local concentrations. As explained earlier, due to gradients in oxygen concentration throughout the construct, along with predicted Michaelis-Menten kinetics for the rate of oxygen uptake, it is expected that cells near the end of the construct may exhibit a slightly lower q_{O_2} than those near the beginning, although the low decrease in oxygen across the constructs in the experiments presented herein should greatly reduce such variations. Similar effects should be noted for the rates of glucose consumption and OPG production, with changing concentrations over time perhaps altering their respective rates. Again, small decreases in global glucose concentration over the time interval between media changes should greatly reduce such

variations in q_{glc}. In addressing these concerns, it is further important to note that the literature values referenced in **Table 4** were obtained from 2D culture experiments which could have suffered from diffusional limitations and/or low local concentration effects, resulting in lower average values. This provides one possible explanation for the discrepancy between those rates calculated herein and those referenced in the literature.

3.3 Development of Real-Time, Non-Destructive Quality Metrics

As mentioned previously, the all-important cell-specific rates calculated in **Section 3.3** are not currently able to be obtained mid-culture without the sacrifice of a sample; however, these cell-specific rates can be used as key indicators of construct quality. Furthermore, such aspects as ALP production rate and calcium deposition (often used in the field as the principle means of determining the osteoblastic differentiation and formation of "bone-like" mineral within a construct) also require sample sacrifice to quantify. In order to overcome these ever-prevalent dilemmas (of not being able to determine a construct's quality without destroying it), other metrics which allow for the determination of construct quality in real time without the need for sample sacrifice must be developed. Some promising alternatives will now be discussed.

3.3.1 OUR, GCR, and OPGPR Ratios Throughout Culture Period

The first logical step in developing such real-time, non-destructive metrics is the examination of ratios of the three mid-culture monitored molecules over time compared with the current destructive standards for determination of a bone tissue engineered construct's quality: ALP activity and calcium deposition (**Figures 19** and **20**; **Section**

3.1). Implementing simple ratios of these potential marker molecules effectively negates the dependence on cellularity of each, resulting in functions which should be valid over vast ranges of cellularity (assuming negligible effect of cellularity on these values). Because there are three monitored molecules utilized herein, three independent plots can be produced via simple ratios of any two of these: these were determined to be OPGPR/GCR, OPGPR/OUR, and OUR/GCR (**Figures 27 – 29**, respectively).

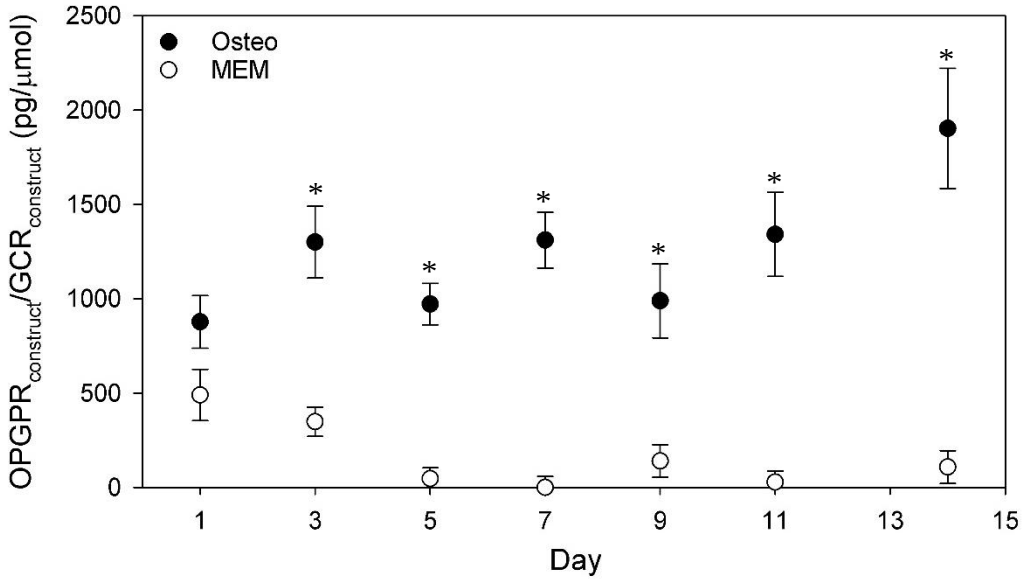

Figure 27. OPGPR/GCR Day 1 – 14
The ratio of per-construct OPG production rate to glucose consumption rate throughout the culture period. Values are seen to increase slightly for the Osteo group, and decline for the MEM group, resulting in statistically significant values for all days but Day 1. Values are presented as mean ± SEM (N=4 for Osteo, 3 for MEM). Significance calculated via ANOVA with Tukey HSD Post-hoc analysis, "*" signifies $p < 0.05$.

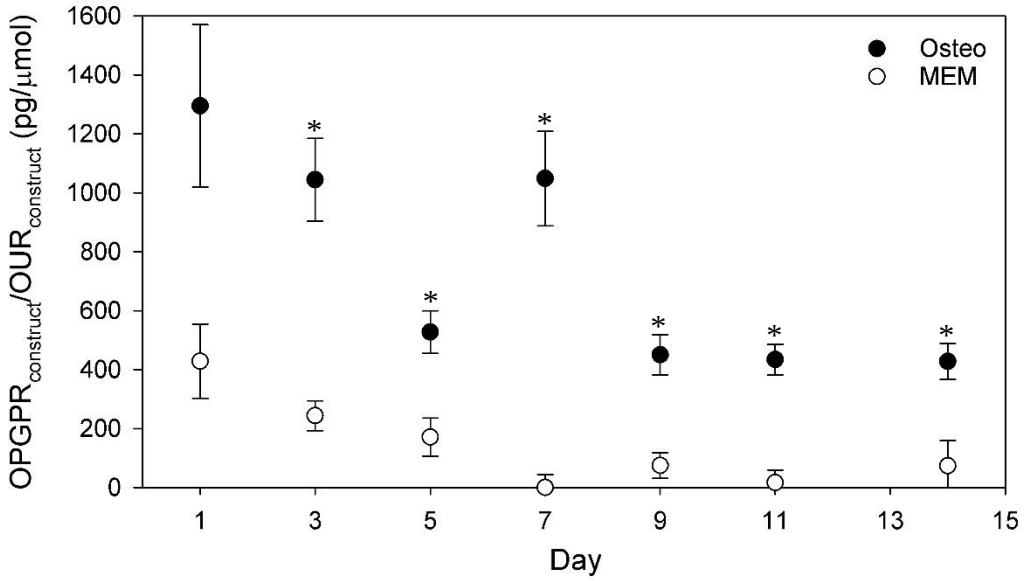

Figure 28. OPGPR/OUR Day 1 – 14
The ratio of per-construct OPG production rate to oxygen uptake rate throughout the culture period. Values are seen to increase decrease for both groups to steady values, though to a steady value much higher for the Osteo group than for the MEM group, resulting in statistically significant values throughout the culture period except for Day 1. Values are presented as mean ± SEM (N=4 for Osteo, 3 for MEM). Significance calculated via ANOVA with Tukey HSD Post-hoc analysis, "*" signifies $p < 0.05$.

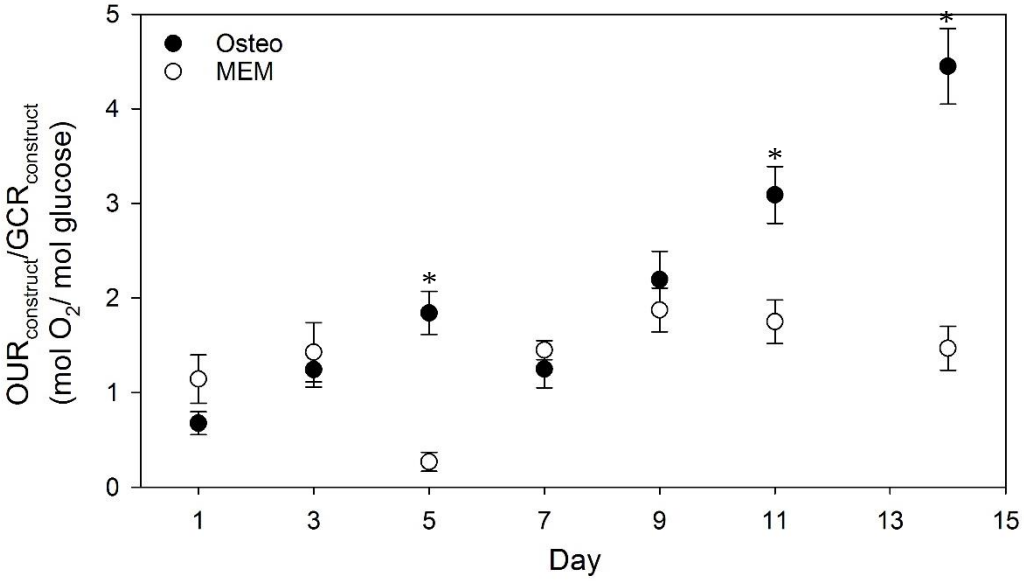

Figure 29. OUR/GCR Day 1 – 14
The ratio of per-construct oxygen uptake rate to glucose consumption rate throughout the culture period. Values for the MEM group are seen to remain fairly constant whereas those for the Osteo group tend to trend upward with time (on average). More marked differences between the two groups are seen for the later time points past Day 9. Values are presented as mean ± SEM (N=4 for Osteo, 3 for MEM). Significance calculated via ANOVA with Tukey HSD Post-hoc analysis, "*" signifies $p < 0.05$.

Observation of the above marker-ratio plots, it may seem as though **Figures 27** and **28** might be the best candidates for the development of quality metrics, however these two plots show statistically significant differences between the groups for a majority of the data range even though little difference is observed in the "gold-standard" quality metrics (ALP and calcium) for the first several data points. Upon comparison of the above plots with the ALP activity and calcium deposition plots developed earlier (**Figures 19** and **20**; **Section 3.1**), it is worthy to note that both the ALP and calcium plots demonstrate similar trends for both groups through Day 7, diverging (to great extent) for only the last few time points, a trend which is most strongly mimicked by **Figure 29**, above for the ratio of OUR/GCR. Furthermore, this ratio has the greatest significance from a physio-metabolic standpoint based on the literature- and experimentally-supported shift in metabolism toward greater reliance on oxidative phosphorylation as MSCs differentiate into osteoblasts. For these reasons, the OUR/GCR ratio was selected as the most promising quality metric, to be discussed further in the following section.

3.3.2 OUR/GCR Ratio as a Metric for Differentiation and Mineralization

As mentioned previously, the OUR/GCR ratio establishes itself as a natural metric for cellular differentiation (and potentially "bone-like" formation) based on a metabolic shift in MSCs as they differentiate into osteoblasts. Additionally, utilization of the ratio of per-construct rates effectively negates the intrinsic unknown cellularity of the construct. The first trend to observe to verify its use in determining the quality of bone tissue engineered constructs is to compare it with current methods for such

determination: ALP activity and calcium deposition, such a comparison is provided in **Figure 30**, below (henceforth all plots were created for the entire data set without differentiation between the Osteo and MEM groups).

The comparison afforded in **Figure 30**, below, reveals the existence of a clear demarcation between constructs exhibiting high calcium deposition and ALP activity and those not when plotted as functions of the OUR/GCR ratio. It is evident from the plot that a cutoff value of approximately OUR/GCR = 2.0 clearly differentiated between these two groups, with constructs exhibiting OUR/GCR ratios greater than 2.0 are very likely to have high osteoblastic differentiation (as evinced by high ALP activity) and high mineral deposition (as evinced by high calcium deposition), effectively representing well-developed bone tissue engineering constructs. (The other ratios discussed in the previous section were attempted but did not reveal strong potential).

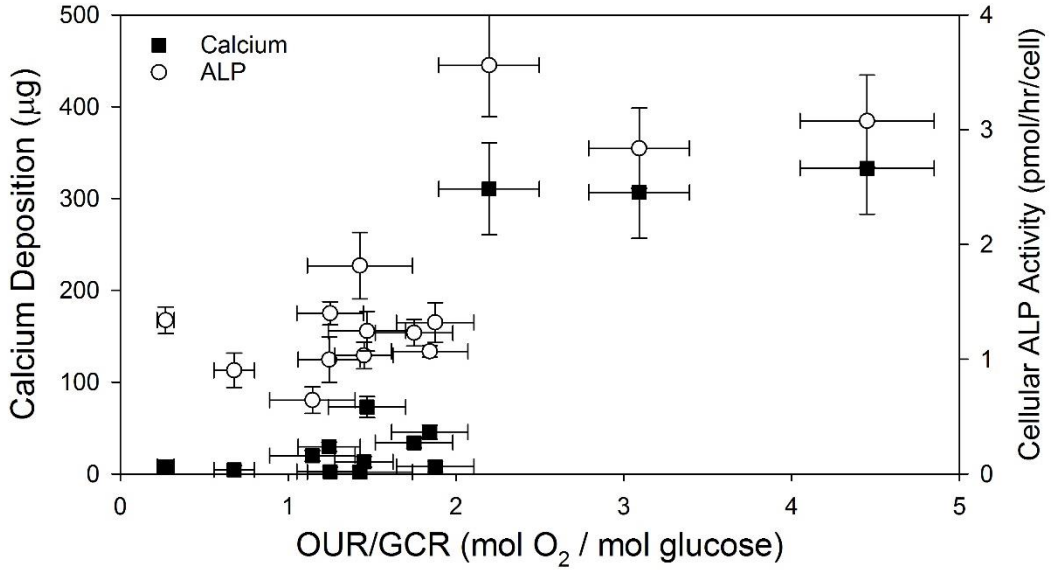

Figure 30. OUR/GCR vs Traditional BTE Construct Quality Markers
The ratio of OUR to GCR (plotted on the abscissa) vs the traditional bone tissue engineering construct quality markers of calcium deposition (on the primary ordinate; solid squares) and cellular ALP activity (on the secondary ordinate; open circles). Although there exists much noise in both data sets for low values of the OUR/GCR ratio, a clear demarcation can be made between low calcium and ALP activity levels corresponding to low ratios of OUR/GCR and high values of these markers

corresponding to high values of this ratio. As such, it appears as though an OUR/GCR ratio greater than ~2 strongly suggests high levels of calcium and ALP activity (thus relatively high occurrence of osteoblastic differentiation and mineral deposition). Values are presented as mean ± SEM (N=4 for Osteo, 3 for MEM).

3.3.3 OUR/GCR Ratio as a Metric for Determination of Cellularity

In order for this ratio to be well suited as a construct quality metric, it must be useful for more than the determination of the osteoblastic differentiation and mineralization of a construct (as **Figure 30** demonstrates is has high potential for). Moreover, it must be useful in determining the cellularity of a construct, albeit itself independent of cellularity. In fact, this seemingly difficult requirement can be achieved indirectly via the utilization of the OUR/GCR ration to determine cell-specific rates (of either oxygen uptake, glucose consumption, or OPG production). If at least one of these cell-specific rates can be accurately determined from the OUR/GCR ratio, this rate can then be divided into its corresponding per-construct rate (able to be quantified in real-time non-destructively) to determine constructs cellularity. With this in mind, **Figures 31** and **32**, below, compare the OUR/GCR ratio with the previously-quantified values of q_{O_2} and q_{glc}, respectively (a similar plot of OUR/GCR vs q_{OPG} was attempted, but revealed no clear trends and so is not included). Both plots were fit with linear regression (based on observation of the relationship between the variables as seen in the figures). 95% confidence intervals were also provided as a means to visualize the accuracy of the fit. The resulting equations and r^2-values for each fit are the following:

$$q_{O_2}\left(\frac{pmol}{hr*cell}\right) = 0.932 + 0.319 * \left(\frac{OUR}{GCR}\right) \qquad r^2 = 0.47 \qquad \textbf{(Eqn. 6)}$$

$$q_{glc}\left(\frac{pmol}{hr*cell}\right) = 1.158 - 0.159 * \left(\frac{OUR}{GCR}\right) \qquad r^2 = 0.56 \qquad \textbf{(Eqn. 7)}$$

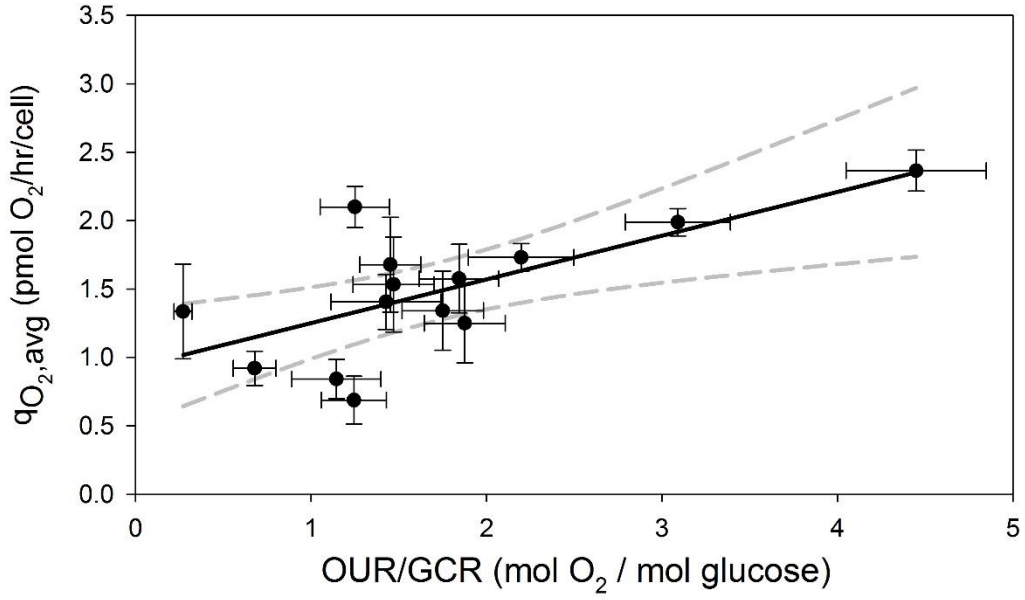

Figure 31. OUR/GCR vs qO_2
The cell-specific oxygen uptake rate as a function of the per-construct OUR/GCR ratio. A fairly decent positive correlation exists, with the linear regression (bold black line) resulting in the following function: $q_{O_2} = 0.932 + 0.319 * (\frac{OUR}{GCR})$ with an $r^2 = 0.47$. The 95% confidence interval is provided (dashed gray lines). Values are presented as mean ± SEM (N=4 for Osteo, 3 for MEM).

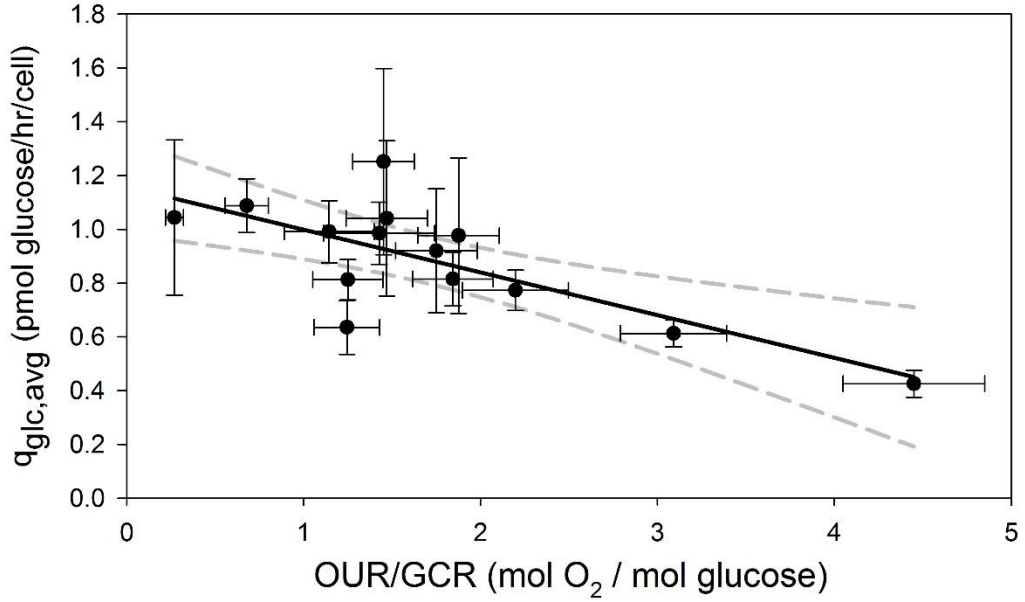

Figure 32. OUR/GCR vs q_{glc}
The cell-specific glucose consumption rate as a function of the per-construct OUR/GCR ratio. A decent negative correlation exists, with the linear regression (bold black line) resulting in the following function: $q_{glc} = 1.158 - 0.159 * (\frac{OUR}{GCR})$ with an $r^2 = 0.56$. The 95% confidence interval is provided (dashed gray lines). Values are presented as mean ± SEM (N=4 for Osteo, 3 for MEM).

Utilizing the linear regressions calculated from the above graphs (**Equations 6** and **7**, above), plots of the OUR/GCR – derived q_{O_2} and q_{glc} vs their experimental values were produced to better visualize the closeness-of fit. Said plots are provided below in **Figures 33** and **34**, respectively. Linear regression was again performed on these plots in order to analyze the slope and y-intercept of each as determinants of closeness-of-fit. Both regressions resulted in slopes of very nearly 1 with very small y-intercepts ($<10^{-3}$). 95% confidence intervals were again added to better visualize the accuracy of the fit.

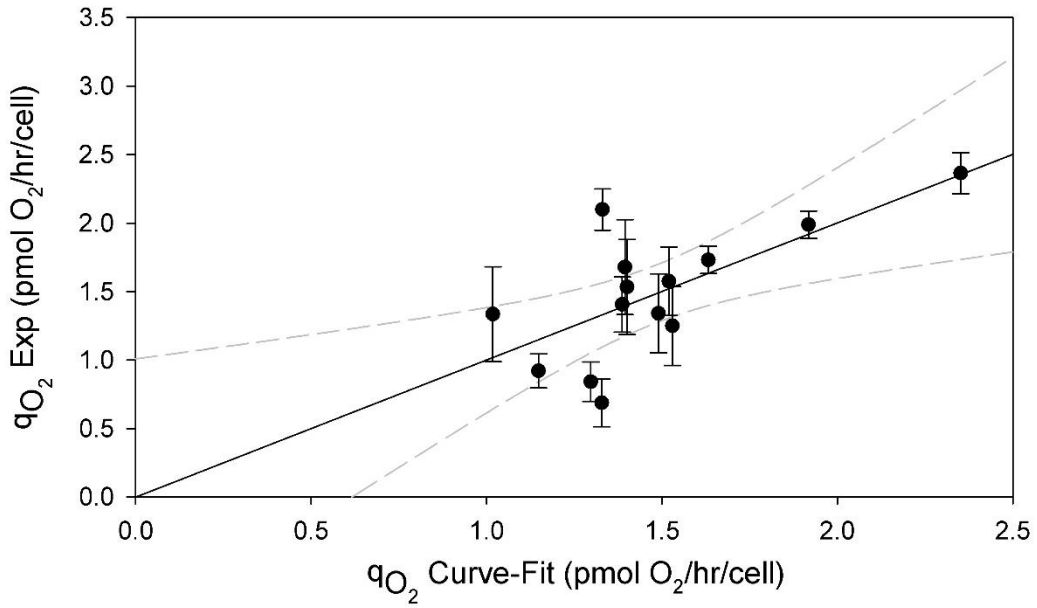

Figure 33. qO_2 Curve-Fit vs. Experimental Values
The OUR/GCR curve-fit cell-specific oxygen uptake rate vs. experimental values. The slope of the linear regression is 1.001, y-intercept is -1.11×10^{-3}, $r^2 = 0.56$. The 95% confidence interval is provided (dashed gray lines). Values are presented as mean ± SEM (N=4 for Osteo, 3 for MEM).

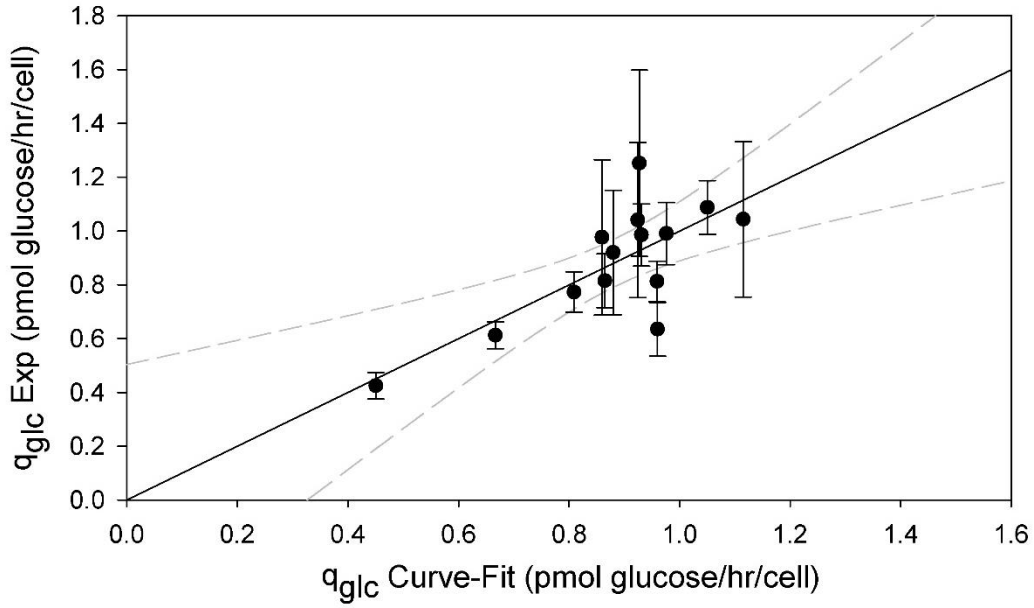

Figure 34. q_{glc} Curve-Fit vs. Experimental Values
The OUR/GCR curve-fit cell-specific glucose consumption rate vs. experimental values. The slope of the linear regression is 0.9998, y-intercept is -1.07×10^{-4}, $r^2 = 0.56$. The 95% confidence interval is provided (dashed gray lines). Values are presented as mean ± SEM (N=4 for Osteo, 3 for MEM).

Finally, **Equations 6** and **7** were used to calculate the cellularity of each construct as a function of only the per-construct OUR and GCR. The resulting equations for cellularity are given below as **Equations 8** and **9**, wherein the former was derived from the $q_{O_2} = f\left(\frac{OUR}{GCR}\right)$ curve-fit and the latter was derived from the $q_{glc} = f\left(\frac{OUR}{GCR}\right)$ curve-fit.

$$N_{cells} = \frac{OUR\left(\frac{\mu mol}{hr}\right)}{\left(0.932+0.319*\left(\frac{OUR}{GCR}\right)\right)} * 10^6 \qquad \textbf{(Eqn. 8)}$$

$$N_{cells} = \frac{GCR\left(\frac{\mu mol}{hr}\right)}{\left(1.158-0.159*\left(\frac{OUR}{GCR}\right)\right)} * 10^6 \qquad \textbf{(Eqn. 9)}$$

These equations were then plotted against the experimentally-obtained values of cellularity for each construct; linear regression was performed to determine fit.

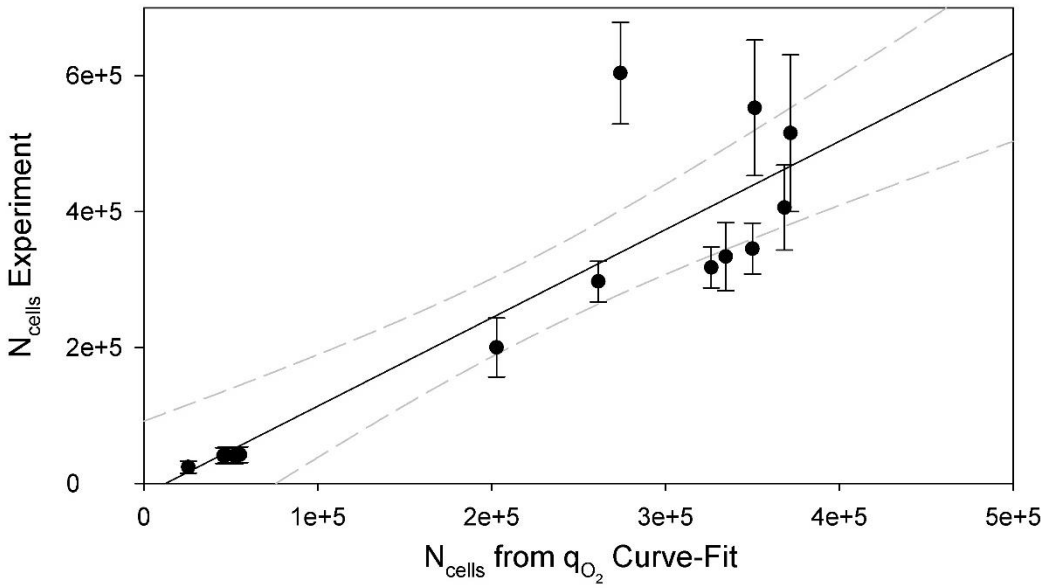

Figure 35. N_{cells} from qO_2 Curve-Fit (Eqn 8) vs. Experimental Values
The cellularity of each construct calculated via Equation 24 vs. its experimentally-determined cellularity. A linear regression (bold black line) resulted in a fairly decent fit, resulting in a slope of 1.30, y-intercept of -16100, and r^2-value of 0.793. The 95% confidence interval is provided (dashed gray lines). The resulting confidence is approximately ± 20% of the calculated cellularity. Values are presented as mean ± SEM (N=4 for Osteo, 3 for MEM).

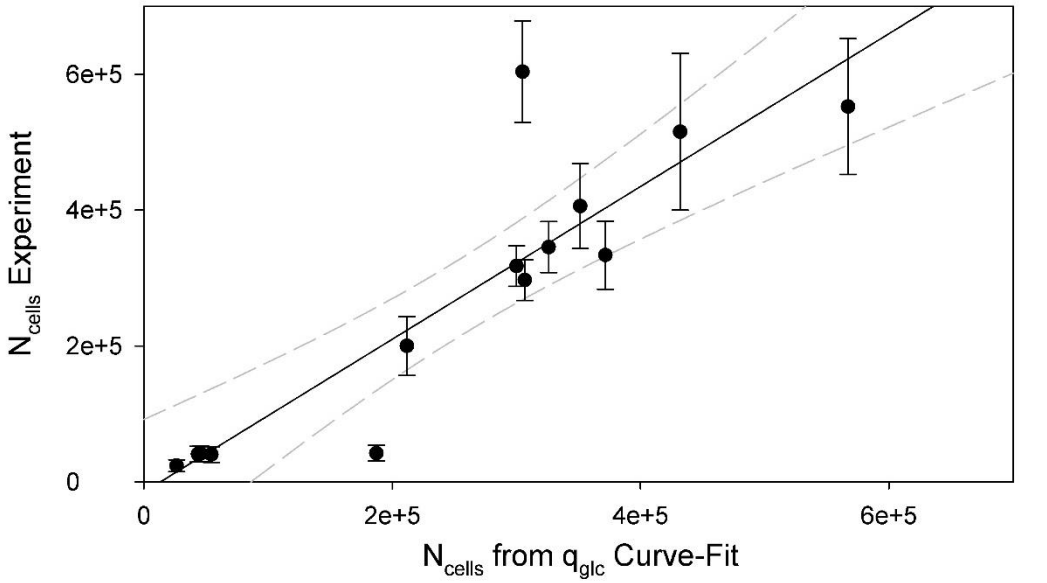

Figure 36. N_{cells} from q_{glc} Curve-Fit (Eqn 9) vs. Experimental Values
The cellularity of each construct calculated via Equation 25 vs. its experimentally-determined cellularity. A linear regression (bold black line) resulted in a fairly decent fit, resulting in a slope of 1.12, y-intercept of -14600, and r^2-value of 0.796. The 95% confidence interval is provided (dashed gray lines). The resulting confidence is approximately ± 20% of the calculated cellularity. Values are presented as mean ± SEM (N=4 for Osteo, 3 for MEM).

Both of these plots (**Figures 35** and **36**) reveal decent curve-fits, with r^2-values very nearly 0.80. As such, the OUR/GCR ratio does prove to have high potential for the determination of the cellularity of a bone tissue engineered construct in real time without the need for its sacrifice. Although oxygen consumption data has been used by others as a means to quantify the cellularity of 3D tissue constructs, this was performed for non-differentiating constructs without a changing metabolic profile[97]. If there exists a change in the cell-specific oxygen consumption rate during the culture period as was experienced herein, then this method is no longer valid, necessitating such a method of non-destructively determining the cell-specific oxygen uptake rate (or other rates) as developed in this study.

3.3.4 Summary of Quality Monitoring Metric Analyses

Upon reviewing several candidates for the real-time non-destructive monitoring and determination of construct quality (defined herein as the combination of the degree of osteoblastic differentiation, amount of mineralization, and overall cellularity of said construct), the most propitious result was obtained via the intrinsically natural (if not obvious) ratio of OUR/GCR. Based on the physio-metabolic changes of MSCs as they differentiate into osteoblasts, this ratio has proven promising as a means for the determination of osteoblastic differentiation and construct maturation (as currently determined via ALP activity and calcium deposition). Furthermore, it seems to be a viable determinant of both cell-specific oxygen uptake and glucose consumption rates, which can subsequently be used to quantify the cellularity of a construct. Additionally, the OPGPR as well as the presence of osteocalcin may potentially be used to verify

OUR/GCR-based data, though methods for such protein detection are typically costlier both in terms of time and money, establishing these as better candidates for intermittent validation as opposed to continual monitoring.

4. CONCLUSIONS

The studies presented herein have elucidated several aspects of bone tissue engineered constructs comprised of 85% porous spunbonded PLLA fibrous scaffolds seeded with rat MSCs and cultured in a flow perfusion bioreactor. Firstly, the flow profile through said constructs was determined via an analysis of residence time distributions to be well approximated by a plug flow model (study and results presented in the **Appendix**). The implications of this finding are not trivial, resulting in the validation of the assumption of negligible radial gradients in the flow profile and related shear stress and chemical species profiles. In other words, it implies that negligible differences in microenvironment should exist for all radial positions at a given axial coordinate, resulting in only axial gradients. With this conclusion, the velocity throughout the construct was determined to be approximately 0.42 cm/min, resulting in average wall shear stress values of approximately 0.017 dyne/cm^2. Comparable to values reported by other groups, ranging from 0.001 to >10 dyne/cm^2, such levels have been shown to positively influence osteoblastic differentiation[98].

Destructive post-culture construct analysis demonstrated successful development of bone tissue engineered constructs by Day 9 of culture in osteoinductive media. This claim is supported by sustained cellularity of 320,000 ± 30,000 cells per construct, and significant increases in ALP activity and calcium deposition to values of 3.0 ± 0.8 pmol/cell/hr and 300 ± 100 ug, respectively. These values were determined to have been significantly higher than those for constructs cultured in non-osteoinductive media of 1.2 ± 0.3 pmol/hr/cell and 70 ± 20 ug, respectively. Interestingly, the non-osteoinduced

constructs also exhibited significantly lower cellularity due to much greater detachment at early time points. Although the reasoning for this is not entirely known, it is hypothesized that it can potentially attributed to hypothetical higher binding affinity of osteoinduced MSCs as their attachment at a defect site is among the first steps in osteoblastic differentiation (whereas MSCs are typically present *in vivo* loosely bound in red bone marrow).

Mid-culture physio-metabolic rates of oxygen uptake, glucose consumption, and OPG production, upon normalization with construct cellularity obtained from the aforementioned post-culture analysis, demonstrated key differences in trends observed for osteoinduced and non-osteoinduced cultures. Increases in the cell-specific oxygen uptake rate of osteoinduced MSCs over time to a value of 2.4 ± 0.3 pmol/hr/cell (by Day 14) were noted to be higher than that for their non-osteoinduced counterparts of 1.4 ± 0.6 pmol/hr/cell. Although these values are seen to be 10-20 fold higher than those presented in the literature, the overall trend of increasing q_{O_2} is supported[93,44,45]. Gradual decreases were observed for the cell-specific glucose consumption rate for osteoinduced cultures to a value of 0.4 ± 0.1 pmol/cell/hr (by Day 14) as compared with the fairly constant value of 1.0 ± 0.4 pmol/cell/hr calculated for non-osteoinduced cultures. These values are in fairly good agreement with the literature, at approximately 2-4 fold higher values, and the overall trend of decreasing q_{glc} is supported [44,45,47,94]. These trends, together, support the conclusion that osteoblastic MSCs observe an increased utilization of oxidative phosphorylation over their immature counterparts, as is well supported in the literature [43–46]. Additionally, significant differences were observed for cell-specific OPG production rates with both cultures starting out with

rates around 0.8 ± 0.3 fg/hr/cell, a value which was fairly well-maintained by osteoinduced cultures exhibiting a value at Day 14 of 0.7 ± 0.2 fg/hr/cell whereas non-osteoinduced cultures experienced rapidly-declining rates to steady levels of 0.1 ± 0.1 fg/hr/cell. Although no literature values were available for cell-specific OPG production rates, the observation of higher rates for osteo-induced cultures as compared with non-osteoinduced ones is supported [28,29,95,96]. Lastly, osteocalcin secretion was detected only for osteoinduced cultures and only at late time points (Day 11 and Day 14), corresponding well with other observed trends, It is important to note that the literature values presented above were determined for cells cultured in stagnant 2D systems, possibly accounting for some of the differences in values obtained.

Finally, comparative analyses enabled the development of potential monitoring schemes for the determination of the differentiation/maturation of bone tissue engineered constructs in addition to their cellularity. These focus primarily on the utilization of the ratio of the per-construct oxygen uptake and glucose consumption rates as a key indicator of said aspects. It has been concluded that a cutoff value of 2.0 for the OUR/GCR can serve as a reliable indicator of osteoblastic differentiation and "bone-like" mineralization of a construct wherein values above 2.0 indicate such progression has occurred while those below 2.0 indicate a lack thereof. Furthermore, this OUR/GCR ratio has been shown to be a decently reliable method of determining cell-specific oxygen uptake and glucose consumption rates via correlation developed herein. Utilization of either (or both) of these rates can then be used along with the per-construct oxygen uptake and/or glucose consumption rates to determine the cellularity of the construct in question. The importance of such a method allowing for reliable

quantification of cells within a construct in real time and non-destructively for constructs with changing metabolic profiles cannot be understated, as it has not previously been possible for such complex systems, as will be required in securing FDA approval for bone tissue engineering interventions as viable bone graft substitutes.

5. FUTURE DIRECTIONS

The study herein has laid the foundation for meeting regulatory-mandated quality control of bone tissue engineered constructs. Further research, however, will be required to validate these results and broaden their applicability. First, the same study should be repeated for longer time points to ensure the developed correlations hold (or if new correlations need be developed to account for osteocytic differentiation at later time points). Moreover, further analyses of the sacrificed constructs could be performed to ensure their quality, such as PCR, histology, etc. Furthermore, more experiments varying initial cell seeding densities, seeding times, and flow rates should be performed to determine the effect of each on the maturation of constructs and their overall quality. Additionally, the monitoring of more potential marker molecules could result in more robust correlations, with lactate being a particularly obvious marker of choice (it was not studies herein as the FBS-supplemented media contains high levels of lactate dehydrogenase, adversely affecting the quantification of lactate; in order to overcome this, studies could be performed using serum-free, chemically-defined media). Finally, several groups have studied the effects of oxygen tension on the culture of MSCs [43–46,54,94]; the normoxic experiments presented herein could easily be adapted to an hypoxic setup with the simple replacement of oxygen-permeable tubing with non-oxygen-permeable tubing. Comparison of results between both setups could help develop the literature, especially noting that a majority of studies of the metabolism of cells *in vitro* are based on 2D culture which has shown in many aspects to differ greatly from 3D culture.

Ultimately, the cells utilized herein would not be applicable to human intervention; as such, repeated studies with human MSCs should be conducted to develop correlations therein (which may vary drastically from rat MSCs). Furthermore, the principles established herein could easily be adapted for the monitoring of tissue engineered constructs other than bone, with the substitution of any of the markers utilized herein with those more relevant to changing physio-metabolic profile of the cells of choice.

REFERENCES

1. Tang, D. *et al.* Biofabrication of bone tissue: approaches, challenges and translation for bone regeneration. *Biomaterials* **83,** 363–382 (2016).
2. Amini, A. R., Laurencin, C. T. & Nukavarapu, S. P. Bone Tissue Engineering: Recent Advances and Challenges. *Crit. Rev. Biomed. Eng.* **40,** 363–408 (2012).
3. Bone Grafts and Substitutes Market expected to reach USD 3.48 Billion Globally in 2023. Available at: http://www.transparencymarketresearch.com/pressrelease/bone-grafts-substitutes-market.htm. (Accessed: 5th April 2016)
4. Gómez-Barrena, E. *et al.* Bone fracture healing: Cell therapy in delayed unions and nonunions. *Bone* **70,** 93–101 (2015).
5. Roberts, T. T. & Rosenbaum, A. J. Bone grafts, bone substitutes and orthobiologics. *Organogenesis* **8,** 114–124 (2012).
6. Bone Graft. *Healthline* Available at: http://www.healthline.com/health/bone-graft. (Accessed: 5th April 2016)
7. Oryan, A., Alidadi, S. & Moshiri, A. Current concerns regarding healing of bone defects. *Hard Tissue* **2,** (2013).
8. Categorization of Bone Grafts | Bone Graft Material | Medtronic. Available at: http://www.infusebonegraft.com/healthcare-providers/bone-grafting-options/categorization-of-bone-grafts/index.htm. (Accessed: 10th July 2016)
9. Oryan, A., Alidadi, S., Moshiri, A. & Maffulli, N. Bone regenerative medicine: classic options, novel strategies, and future directions. *J. Orthop. Surg.* **9,** 18 (2014).
10. Dilthey, M. R. What Percentage of Body Mass is Bone? *LIVESTRONG.COM* Available at: http://www.livestrong.com/article/368497-percentage-of-body-mass-bone/. (Accessed: 11th July 2016)
11. Underst, P. O. V. with E. to & us, high quality health content for many years F. Frame size, how much does it affect your weight? - Measures of weight. *HealthStatus* (2007).

12. Introduction to Bone Biology: All About our Bones | International Osteoporosis Foundation. Available at: https://www.iofbonehealth.org/introduction-bone-biology-all-about-our-bones. (Accessed: 11th July 2016)
13. KristenW, A. T. A. Bones: A Brief Review on its Functions, Types, Structure and Development. *Interactive Biology, with Leslie Samuel* (2012).
14. ASBMR educational materials. Available at: https://depts.washington.edu/bonebio/ASBMRed/structure.html. (Accessed: 11th July 2016)
15. Boundless. Cell Types in Bones. *Boundless* (2016).
16. Types of Cells in Bone. Available at: http://www.mananatomy.com/basic-anatomy/types-cells-bone. (Accessed: 15th July 2016)
17. Bonewald, L. F. The Amazing Osteocyte. *J. Bone Miner. Res.* **26,** 229–238 (2011).
18. Aarden, E. M., Nijweide, P. J. & Burger, E. H. Function of osteocytes in bone. *J. Cell. Biochem.* **55,** 287–299 (1994).
19. Boyce, B. F., Yao, Z. & Xing, L. Osteoclasts have Multiple Roles in Bone in Addition to Bone Resorption. *Crit. Rev. Eukaryot. Gene Expr.* **19,** 171–180 (2009).
20. Teitelbaum, S. L. Bone Resorption by Osteoclasts. *Science* **289,** 1504–1508 (2000).
21. Alvarez, K. & Nakajima, H. Metallic Scaffolds for Bone Regeneration. *Materials* **2,** 790–832 (2009).
22. Bone & Skeletal Tissue Chapter 6. *SlidePlayer.com* Available at: http://slideplayer.com/slide/5017761/. (Accessed: 16th July 2016)
23. Clarke, B. Normal Bone Anatomy and Physiology. *Clin. J. Am. Soc. Nephrol. CJASN* **3,** S131–S139 (2008).
24. Dixon, J., Bird, H., Mbuyi-Muamba, J.-M., Dequeker, J. & Gevers, G. Biochemistry of bone. *Baillières Clin. Rheumatol.* **2,** 63–101 (1988).
25. Non-Collagen Bone Proteins. *Bone and Spine* (2008).
26. Young, M. F. Bone matrix proteins: their function, regulation, and relationship to osteoporosis. *Osteoporos. Int.* **14,** 35–42 (2003).
27. Simonet, W. S. *et al.* Osteoprotegerin: A Novel Secreted Protein Involved in the Regulation of Bone Density. *Cell* **89,** 309–319 (1997).

28. Udagawa, N. *et al.* Osteoprotegerin produced by osteoblasts is an important regulator in osteoclast development and function. *Endocrinology* **141,** 3478–3484 (2000).
29. Nakamichi, Y. *et al.* Osteoprotegerin Reduces the Serum Level of Receptor Activator of NF-κB Ligand Derived from Osteoblasts. *J. Immunol.* **178,** 192–200 (2007).
30. Oshita, K. *et al.* Human mesenchymal stem cells inhibit osteoclastogenesis through osteoprotegerin production. *Arthritis Rheum.* **63,** 1658–1667 (2011).
31. Guo, T. *et al.* Molecular Docking Characterization of a Four-Domain Segment of Human Fibronectin Encompassing the RGD Loop with Hydroxyapatite. *Molecules* **19,** 149–158 (2013).
32. BME 332: Bone Structure-Function. Available at: http://www.umich.edu/~bme332/ch9bone/bme332bone.htm. (Accessed: 17th July 2016)
33. SEER Training:Structure of Bone Tissue. Available at: http://training.seer.cancer.gov/anatomy/skeletal/tissue.html. (Accessed: 11th July 2016)
34. Gilbert, S. F. Osteogenesis: The Development of Bones. (2000).
35. Endochondral Ossification and Intramembranous Ossification. *Bone and Spine* (2015).
36. Ossification. *DEVELOPMENT OF HUMAN SKELETAL SYSTEM* Available at: http://skeletalsystemdev.weebly.com/ossification.html. (Accessed: 18th July 2016)
37. 7-6-3. Bone. *Ubooks* Available at: http://www.ubooks.pub/Books/ON/B0/E26R6789/P7C6S3U25.html. (Accessed: 18th July 2016)
38. Woven Bone and Lamellar Bone. *Bone and Spine* (2009).
39. The Role of Minerals in Joint Health. Available at: http://www.sierrasil.com/connect/news/studies/the-role-of-minerals-in-joint-health/. (Accessed: 18th July 2016)
40. Boundless. Bone Remodeling and Repair. *Boundless* (2016).

41. Kalfas, I. Principles of Bone Healing. *Medscape* (2001). Available at: http://www.medscape.com/viewarticle/405699. (Accessed: 10th July 2016)
42. Marzona, L. & Pavolini, B. Play and players in bone fracture healing match. *Clin. Cases Miner. Bone Metab.* **6,** 159–162 (2009).
43. Shyh-Chang, N., Daley, G. Q. & Cantley, L. C. Stem cell metabolism in tissue development and aging. *Development* **140,** 2535–2547 (2013).
44. Pattappa, G., Heywood, H. K., de Bruijn, J. D. & Lee, D. A. The metabolism of human mesenchymal stem cells during proliferation and differentiation. *J. Cell. Physiol.* **226,** 2562–2570 (2011).
45. Pattappa, G. *et al.* Continuous and Uninterrupted Oxygen Tension Influences the Colony Formation and Oxidative Metabolism of Human Mesenchymal Stem Cells. *Tissue Eng. Part C Methods* **19,** 68–79 (2012).
46. Chen, C.-T., Shih, Y.-R. V., Kuo, T. K., Lee, O. K. & Wei, Y.-H. Coordinated Changes of Mitochondrial Biogenesis and Antioxidant Enzymes During Osteogenic Differentiation of Human Mesenchymal Stem Cells. *STEM CELLS* **26,** 960–968 (2008).
47. Schop, D. *et al.* Growth, Metabolism, and Growth Inhibitors of Mesenchymal Stem Cells. *Tissue Eng. Part A* **15,** 1877–1886 (2009).
48. Hughey, C. C. *et al.* Increased oxygen consumption and OXPHOS potential in superhealer mesenchymal stem cells. *Cell Regen.* **1,** 3 (2012).
49. Sart, S., Agathos, S. N. & Li, Y. Process engineering of stem cell metabolism for large scale expansion and differentiation in bioreactors. *Biochem. Eng. J.* **84,** 74–82 (2014).
50. Smith, D. M., Johnston, C. C. & Severson, A. R. Studies of the metabolism of separated bone cells. I. Techniques of separation and identification. *Calcif. Tissue Res.* **11,** 56–69 (1973).
51. Zahm, A. M. *et al.* Numerical modeling of oxygen distributions in cortical and cancellous bone: oxygen availability governs osteonal and trabecular dimensions. *Am. J. Physiol. - Cell Physiol.* **299,** C922–C929 (2010).
52. Hirao, M. *et al.* Oxygen tension is an important mediator of the transformation of osteoblasts to osteocytes. *J. Bone Miner. Metab.* **25,** 266–276 (2007).

53. Zahm, A., Bucaro, M., Srinivas, V., Shapiro, I. M. & Adams, C. S. OXYGEN TENSION REGULATES PREOSTEOCYTE MATURATION AND MINERALIZATION. *Bone* **43,** 25–31 (2008).
54. Utting, J. C. *et al.* Hypoxia inhibits the growth, differentiation and bone-forming capacity of rat osteoblasts. *Exp. Cell Res.* **312,** 1693–1702 (2006).
55. Warren, S. M. *et al.* Hypoxia Regulates Osteoblast Gene Expression. *J. Surg. Res.* **99,** 147–155 (2001).
56. Yousefi, A.-M. *et al.* Prospect of Stem Cells in Bone Tissue Engineering: A Review. *Stem Cells Int.* **2016,** (2016).
57. Robey, P. G. Cell Sources for Bone Regeneration: The Good, the Bad, and the Ugly (But Promising). *Tissue Eng. Part B Rev.* **17,** 423–430 (2011).
58. Black, C. R. M. *et al.* Bone Tissue Engineering. *Curr. Mol. Biol. Rep.* **1,** 132–140 (2015).
59. Velasco, M. A., Narváez-Tovar, C. A. & Garzón-Alvarado, D. A. Design, Materials, and Mechanobiology of Biodegradable Scaffolds for Bone Tissue Engineering. *BioMed Res. Int.* **2015,** (2015).
60. Yu, X., Tang, X., Gohil, S. V. & Laurencin, C. T. Biomaterials for Bone Regenerative Engineering. *Adv. Healthc. Mater.* **4,** 1268–1285 (2015).
61. Narayanan, G., Vernekar, V. N., Kuyinu, E. L. & Laurencin, C. T. Poly (lactic acid)-based biomaterials for orthopaedic regenerative engineering. *Adv. Drug Deliv. Rev.* doi:10.1016/j.addr.2016.04.015
62. Ulery, B. D., Nair, L. S. & Laurencin, C. T. Biomedical Applications of Biodegradable Polymers. *J. Polym. Sci. Part B Polym. Phys.* **49,** 832–864 (2011).
63. Shim, I. K. *et al.* Novel three-dimensional scaffolds of poly(L-lactic acid) microfibers using electrospinning and mechanical expansion: Fabrication and bone regeneration. *J. Biomed. Mater. Res. B Appl. Biomater.* **95B,** 150–160 (2010).
64. Cai, Y. Z. *et al.* Electrospun nanofibrous matrix improves the regeneration of dense cortical bone. *J. Biomed. Mater. Res. A* **95A,** 49–57 (2010).
65. van Dijk, M. *et al.* In vitro and in vivo degradation of bioabsorbable PLLA spinal fusion cages. *J. Biomed. Mater. Res.* **63,** 752–759 (2002).

66. Slivka, M. A., Chu, C. C. & Adisaputro, I. A. Fiber-matrix interface studies on bioabsorbable composite materials for internal fixation of bone fractures. I. Raw material evaluation and measurement of fiber—matrix interfacial adhesion. *J. Biomed. Mater. Res.* **36,** 469–477 (1997).
67. Stiers, P.-J., van Gastel, N. & Carmeliet, G. Targeting the hypoxic response in bone tissue engineering: A balance between supply and consumption to improve bone regeneration. *Mol. Cell. Endocrinol.* **432,** 96–105 (2016).
68. Kaveh, K., Ibrahim, R., Zuki Abu B, M. & Azmi Ibrah, T. Mesenchymal Stem Cells, Osteogenic Lineage and Bone Tissue Engineering: A Review. *J. Anim. Vet. Adv.* **10,** 2317–2330 (2011).
69. Langenbach, F. & Handschel, J. Effects of dexamethasone, ascorbic acid and β-glycerophosphate on the osteogenic differentiation of stem cells in vitro. *Stem Cell Res. Ther.* **4,** 117 (2013).
70. Yeatts, A. B. & Fisher, J. P. Bone tissue engineering bioreactors: dynamic culture and the influence of shear stress. *Bone* **48,** 171–181 (2011).
71. Rauh, J., Milan, F., Günther, K.-P. & Stiehler, M. Bioreactor Systems for Bone Tissue Engineering. *Tissue Eng. Part B Rev.* **17,** 263–280 (2011).
72. El Haj, A. J. & Cartmell, S. H. Bioreactors for bone tissue engineering. *Proc. Inst. Mech. Eng. [H]* **224,** 1523–1532 (2010).
73. Yeatts, A. B., Choquette, D. T. & Fisher, J. P. Bioreactors to Influence Stem Cell Fate: Augmentation of Mesenchymal Stem Cell Signaling Pathways via Dynamic Culture Systems. *Biochim. Biophys. Acta* **1830,** 2470–2480 (2013).
74. Salter, E. *et al.* Bone tissue engineering bioreactors: a role in the clinic? *Tissue Eng. Part B Rev.* **18,** 62–75 (2012).
75. Gaspar, D. A., Gomide, V. & Monteiro, F. J. The role of perfusion bioreactors in bone tissue engineering. *Biomatter* **2,** 167–175 (2012).
76. Brockbank, K. G. M. *Tissue Engineering Constructs and Commercialization*. (Landes Bioscience, 2013).
77. Lloyd-Evans, M. Regulating tissue engineering. *Mater. Today* **7,** 48–55 (2004).
78. Hellman, KB. in *Topics in Tissue Engineering* (eds. Ashammakhi, R. R. & Chiellini, F.) (2008).

79. Evans, C. H. Barriers to the Clinical Translation of Orthopedic Tissue Engineering. *Tissue Eng. Part B Rev.* **17,** 437–441 (2011).
80. CFR - Code of Federal Regulations Title 21 Part 1271. Available at: http://www.accessdata.fda.gov/scripts/cdrh/cfdocs/cfcfr/CFRSearch.cfm?CFRPart=1271&showFR=1. (Accessed: 22nd July 2016)
81. Jeffrey K. Shapiro & Brian J. Wesoloski. FDA's Regulatory Scheme for Human Tissue: A Breif Overview. (2007).
82. CFR - Code of Federal Regulations Title 21 Part 861. Available at: http://www.accessdata.fda.gov/scripts/cdrh/cfdocs/cfcfr/CFRSearch.cfm?CFRPart=861&showFR=1&subpartNode=21:8.0.1.1.17.1. (Accessed: 22nd July 2016)
83. Maniatopoulos, C., Sodek, J. & Melcher, D. A. H. Bone formation in vitro by stromal cells obtained from bone marrow of young adult rats. *Cell Tissue Res.* **254,** 317–330 (1988).
84. de Rovère, A. & Shambaugh, R. L. Melt-Spun Hollow Fibers for Use in Nonwoven Structures. *Ind. Eng. Chem. Res.* **40,** 176–187 (2001).
85. Tuin, S. A., Pourdeyhimi, B. & Loboa, E. G. Interconnected, microporous hollow fibers for tissue engineering: Commercially relevant, industry standard scale-up manufacturing. *J. Biomed. Mater. Res. A* **102,** 3311–3323 (2014).
86. Tuin, S. A., Pourdeyhimi, B. & Loboa, E. G. Creating tissues from textiles: scalable nonwoven manufacturing techniques for fabrication of tissue engineering scaffolds. *Biomed. Mater.* **11,** 15017 (2016).
87. VanGordon, S. B. *et al.* Effects of Scaffold Architecture on Preosteoblastic Cultures under Continuous Fluid Shear. *Ind. Eng. Chem. Res.* **50,** 620–629 (2011).
88. Bancroft, G. N., Sikavitsas, V. I. & Mikos, A. G. Design of a Flow Perfusion Bioreactor System for Bone Tissue-Engineering Applications. *Tissue Eng.* **9,** 549–554 (2003).
89. Mikos, A. G., Lyman, M. D., Freed, L. E. & Langer, R. Wetting of poly(l-lactic acid) and poly(dl-lactic-co-glycolic acid) foams for tissue culture. *Biomaterials* **15,** 55–58 (1994).

90. Optical Dissolved Oxygen. *Ocean Optics* (2015). Available at: http://oceanoptics.com/tech-tip-principles-of-optical-dissolved-oxygen-measurements/. (Accessed: 2nd June 2016)
91. Yoo, E.-H. & Lee, S.-Y. Glucose Biosensors: An Overview of Use in Clinical Practice. *Sensors* **10,** 4558–4576 (2010).
92. Glucose Meter for Cell Culture. *CESCO BioProducts* Available at: http://www.cescobioproducts.com/gluccell-glucose-monitoring-system.html. (Accessed: 3rd June 2016)
93. Komarova, S. V., Ataullakhanov, F. I. & Globus, R. K. Bioenergetics and mitochondrial transmembrane potential during differentiation of cultured osteoblasts. *Am. J. Physiol. - Cell Physiol.* **279,** C1220–C1229 (2000).
94. dos Santos, F. *et al.* Ex vivo expansion of human mesenchymal stem cells: A more effective cell proliferation kinetics and metabolism under hypoxia. *J. Cell. Physiol.* **223,** 27–35 (2010).
95. Schoppet, M., Preissner, K. T. & Hofbauer, L. C. RANK ligand and osteoprotegerin: paracrine regulators of bone metabolism and vascular function. *Arterioscler. Thromb. Vasc. Biol.* **22,** 549–553 (2002).
96. Sharaf-Eldin, W. E. *et al.* The Modulatory Effects of Mesenchymal Stem Cells on Osteoclastogenesis, The Modulatory Effects of Mesenchymal Stem Cells on Osteoclastogenesis. *Stem Cells Int. Stem Cells Int.* **2016, 2016,** e1908365 (2015).
97. Santoro, R., Krause, C., Martin, I. & Wendt, D. On-line monitoring of oxygen as a non-destructive method to quantify cells in engineered 3D tissue constructs. *J. Tissue Eng. Regen. Med.* **6,** 696–701 (2012).
98. Litwack, G. *Stem Cell Regulators*. (Academic Press, 2011).
99. Levenspiel, O. *Chemical Reaction Engineering*. (John Wiley & Sons, 1999).

APPENDIX

A.1 Bioreactor Flow Profile Characterization

The above rate-of-change equations allow for the quantification of the total drop in species concentration over time (or across the construct), but do not allow for the determination and/or prediction of the intra-construct species concentration profiles. In order to determine these, the flow profile through the constructs must be determined. This was achieved by performing a residence time distribution (RTD) analysis for the constructs.

A.1.1 Residence Time Distribution Basics

The method of residence time distribution analysis consists of injecting a tracer into the flow stream upstream of the construct chamber, and quantifying its concentration downstream of the chamber over time. For these studies, the tracer of choice was selected to trypan blue due to its ready dissolution in water, distinct absorbance peak at 590 nm out to fairly dilute concentrations, and its potential for use in future experiments.

Two predominant methods exist for such analysis: a pulse tracer input and a step tracer input. Each has its own benefits and disadvantages, and as such both were employed in order to best characterize the flow; each will now be discussed, in turn.

A.1.2 Pulse Tracer Input

A pulse tracer input consists of injecting a small quantity of tracer into the stream for a short amount of time and observing the peak and subsequent wash-out of said tracer. This was achieved by utilizing two 3-way valves and an injection tip connected in series with the inlet tubing and creating two parallel flow paths, one of which is pre-loaded with the tracer and the other of which is open to the main flow line (as seen in **Figure A1a**, below). At time t = 0 both valves were turned to divert the flow through the tracer-loaded channel, and samples were begun to be collected of the effluent of the construct chamber. Each sample consisted of 2 droplets obtained in approximately 22 seconds (resulting in approximately 55 µL of sample) collected in micro-centrifuge tubes. The experiment was allowed to run until the effluent was observed to have no remaining trypan blue. Experiments were run at a flowrate of 150 µL / min (the same flowrate used for the bioreactor experiments) with the use of the same peristaltic pump used for the bioreactor experiments (Langer Instruments, Model # BT100-1L). At the end of each run, 50 µL of each sample was loaded into a clear 96-well plate and subsequently run on a Synergy HT microplate reader (Bio-Tek) at an absorbance wavelength of 590 nm. Controls were also run for the concentration profile exiting the injection tip (to allow for compensation of the delay from t = 0 to the actual time the tracer entered into the construct chamber) and for the profile through the empty cassette (without a scaffold, to determine the effect the scaffold plays in the flow profile). Multiple experiments were run for each condition.

Raw absorbance values from the plate reader were corrected by subtracting a baseline absorbance of 50 µL of DI water at 590 nm. These corrected values constituted the

concentration profiles, c(t). Next, the residence time distribution function, E(t), and cumulative distribution function, F(t), were calculated in order to normalize all runs:

$$E(t) = \frac{C(t)}{\int_0^{t_{final}} C(t)dt} \quad \textbf{(Eqn. A1)}$$

$$F(t) = \int_0^t E(t)dt \quad \textbf{(Eqn. A2)}$$

Where t_{final} is defined as the time at which $c(t)$ reached 101% of the baseline DI water value

Numerical integration using the trapezoid rule was employed in solving F(t).

Then, the mean residence time, t_m, and variance, σ^2, were calculated for each run:

$$t_m = \tau = \int_0^{t_{final}} t * E(t)dt \quad \textbf{(Eqn. A3)}$$

$$\sigma^2 = \int_0^{t_{final}} (t - t_m)^2 * E(t)dt \quad \textbf{(Eqn. A4)}$$

Next, in order to relate the injection profile, empty cassette, and experimental runs, the dimensionless forms the residence time and cumulative distribution functions were calculated:

$$E(\Theta) = \tau * E(t) \quad \textbf{(Eqn. A5)}$$

$$F(\Theta) = \int_0^{\Theta_{final}} E(\Theta)d\Theta \quad \textbf{(Eqn. A6)}$$

Where $\Theta = \frac{t}{\tau}$ = dimensionless time

Finally, the resulting functions were plotted and qualitatively analyzed against literature curves for a variety of flow reactor systems.

A.1.3 Step Tracer Input

A step tracer input consists of a continuous injection of a tracer into the flow stream and observing the increase in tracer concentration until such time as the effluent concentration of the tracer is equal to that of the injected tracer. This was achieved by utilizing three 3-way valves connected in a Y-pattern (as seen in **Figure A1d**, below). The upper valves were connected in series to separate recirculation loops (one for a diluted tracer reservoir and one for a DI water reservoir). The lower valve was used to select either the water or the tracer as the injection fluid. At time t = 0 all three valves were turned to divert the selected injection fluid from the DI water to the tracer, and samples were begun to be collected of the effluent of the construct chamber. The experiment was allowed to run until the effluent was observed to have a tracer concentration equal to the inlet tracer concentration. Remainder of experiment was performed as described for pulse input (described above).

Raw absorbance values from the plate reader were corrected by subtracting a baseline absorbance of 50 µL of DI water at 590 nm. These corrected values constituted the concentration profiles, c(t). Next, the cumulative distribution function, F(t), and residence time distribution function, E(t), were calculated in order to normalize all runs:

$$F(t) = c(t)/c_0 \qquad \textbf{(Eqn. A7)}$$

$$E(t) = \frac{d}{dt}\big(F(t)\big) \qquad \textbf{(Eqn. A8)}$$

Where c_0 = tracer input concentration

Due to the step size and noise in the data, numerical differentiation was unsuccessful for calculating E(t). As such, c(t) was curve-fit utilizing a least-squares regression. The equation employed for the fit was selected to be of the form of **Eqn. A9**. In order to improve the fit, weighting factors were employed for the scaffold run (**Eqn. A10**).

$$c(t) = c_0 - \frac{c_0}{1+\left(\frac{t-t_{bt}}{C_1}\right)^{C_2}} \qquad \textbf{(Eqn. A9)}$$

$$c(t) = \left[c_0 - \frac{c_0}{1+\left(\frac{t-t_{bt}}{C_1}\right)^{C_2}}\right] * (1-W) + c_0 * W \qquad \textbf{(Eqn. A10)}$$

Where $W = \frac{t-t_{bt}}{t_f-t_{bt}}$

t_{bt} = breakthrough time (at which tracer was first detected in effluent)

t_f = final time (when the effluent concentration reached 99% of the input concentration)

C_1, C_2 = curve-fitting parameters

The resulting functions were then analytically differentiated to produce E(t).

The remainder of the analysis was followed as described for the pulse input, above.

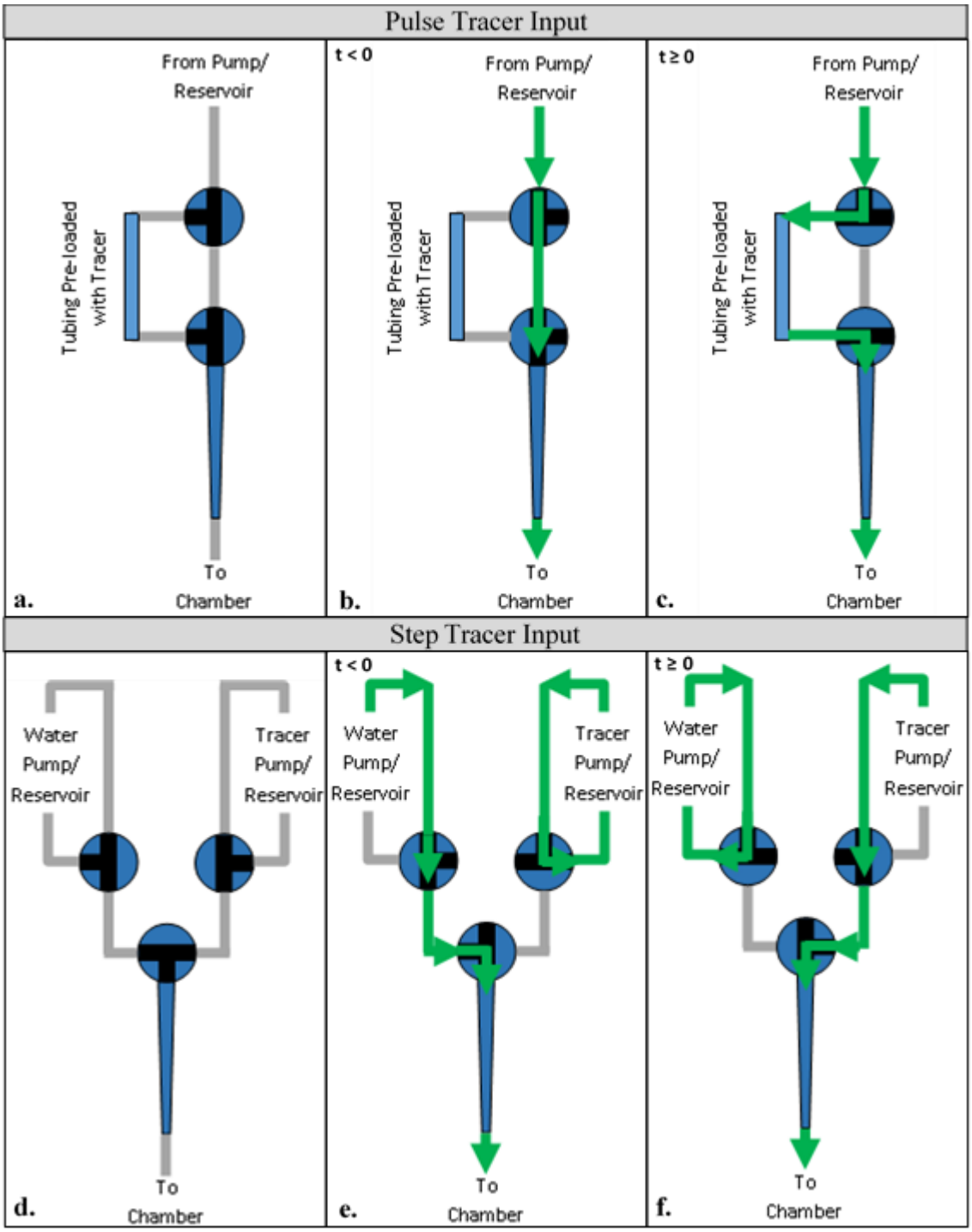

Figure 37. RTD Experimental Set-Up and Flow Diagrams
Diagrams a. through c. represent the setup for the pulse input experiments. Diagrams d. through f. represent that for the step input experiments. Green arrows represent the flow paths for the pre-experimental (b. and e.) and experimental (c. and f.) setups. The blue circles represent 3-way valves with flow channels indicated in black. The blue trapezoids at the bottom of each diagram represent the injection tip.

A.1.4 Shear Stress Analysis

Upon determining the flow distribution pattern throughout the construct, the velocity profile was subsequently calculated to be approximated by plug flow. Assuming the media behaves as a Newtonian fluid flowing at a constant velocity through a uniformly-porous scaffold through cylindrical pores exhibiting laminar flow through each individual pore, the wall shear stress was calculated as:

$$\sigma_w = -\mu * \frac{dv_z}{dr}|_{r=R} = -\mu * \left(-2 * v_{media,avg} * \frac{2}{R_{pore}}\right) \quad \textbf{(Eqn. A11a)}$$

$$= \frac{8*\mu*v_z}{D_{pore}} \quad \textbf{(Eqn. A11b)}$$

Where μ = dynamic viscosity of media, 0.75 cp

v_z = average media velocity

D_{pore} = pore diameter of construct, 250 µm

The resulting values for the wall shear stress throughout the scaffold were compared with literature values as they pertain to osteoinductive effects.

A.2 Results: Bioreactor Flow Characterization via RTD Analysis

In order to better understand the flow characteristics within the flow perfusion bioreactor utilized within these experiments, residence time distribution analyses were performed. These allow for the determination of the flow profile(s) present within the reactor which subsequently allow for the estimation of shear stress and concentration profiles within the *in vitro* cultured constructs.

A.2.1 Pulse Tracer Input

Three RTD experimental runs were performed with pulse tracer inputs at the bioreactor flow rate of 150 μL/min for each of the following setups: injection, open cassette, scaffold in cassette, and void-plugged scaffold in cassette. These setups were selected in order to best understand the individual contribution of each on the resulting RTD data, enabling for the deconvolution of the data obtained for the setup equal to that used in all cell-based studies. The injection runs represent the input concentration profile, the open cassette runs represent the flow through the cassette without any scaffold, the scaffold in cassette runs represent the experimental setup used for the cell-based studies, and the void-plugged scaffold in cassette represents the flow through the scaffold alone (with the void space above the scaffold in the cassette plugged, in order to determine the effect of this void space on the flow field). The resulting RTD and cumulative distribution functions are provided below in **Figure A2** and **Figure A3**, respectively.

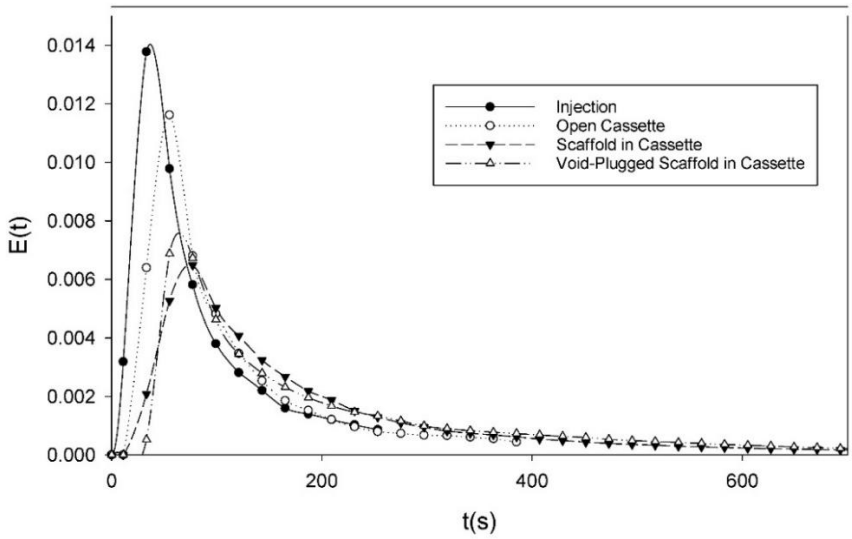

Figure 38. E(t) - Pulse Tracer Input
Residence time distribution functions for pulse tracer inputs into bioreactor. Injection (solid circles) is the tracer input profile; open cassette (open circles) is the exit profile from the cassette without a scaffold; scaffold in cassette (solid triangles) is the exit profile from the cassette with a scaffold; void-plugged scaffold in cassette (open triangles) is the exit profile from the cassette with a scaffold with the void space above the scaffold plugged. The times corresponding to each peak, t_{pk}, are 35 s, 55 s, 80 s, and 65 s, respectively. The mean residence times, τ, associated with each function are 80 s, 110 s, 185 s, and 200 s, respectively. Error bars removed to facilitate viewing, with average standard deviations of approximately 15%.

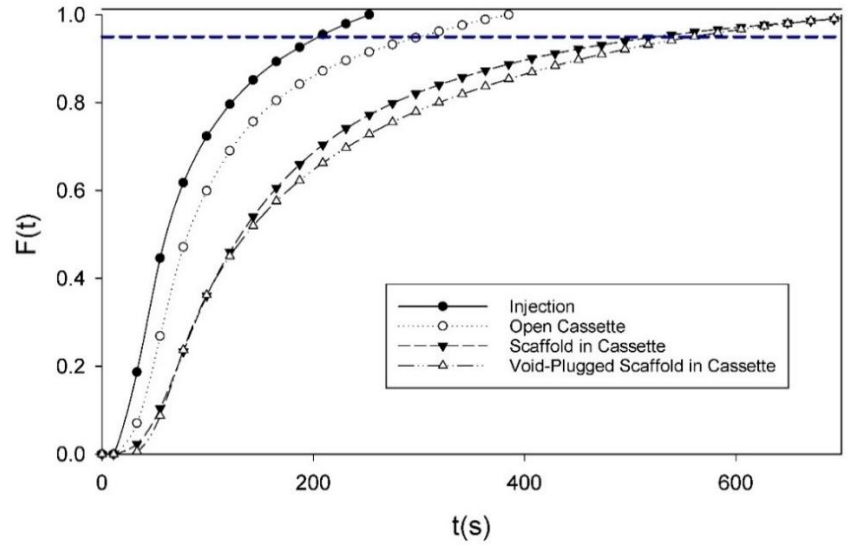

Figure 39. F(t) – Pulse Tracer Input
Cumulative distribution functions for pulse tracer inputs into bioreactor. Same experimental setups as described in **Figure A2**. The dashed horizontal line is located at F(t) = 0.95, representing the point at which 95% of the injected tracer had exited the reactor. The corresponding times for 95% tracer clearance, t_{95}, for each function are 200 s, 295 s, 525 s, and 545 s, respectively.

It is evident from **Figures A2** and **A3**, above, that the tracer input deviates from the ideal Dirac delta function, exhibiting significant tail-right behavior due to the mode of injection. This non-ideal injection can be seen to affect the effluent profiles, though comparative analysis can still be accomplished with compensation. For a first approximation, this can be achieved by simply subtracting the relevant times associated with the injection profile from the times associated with effluent profile. The resulting corrected values are tabulated in **Table A1**, below. In order to better compare the flow phenomena, the E(t) and F(t) curves must be normalized by residence time; the resulting graphs are provided as **Figures A4** and **A5**, below.

	Raw Values			**Corrected Values**		
	$t_{pk}\ (s)$	$\tau\ (s)$	$t_{95}\ (s)$	$t_{pk}^{*}\ (s)$	$\tau^{*}\ (s)$	$t_{95}^{*}\ (s)$
Injection	35	80	200	0	0	0
Empty Cassette	55	110	295	20	30	95
Scaffold	80	185	525	45	105	325
VP-Scaffold	65	200	545	30	120	345

Table 5. Characteristic Times for RTD Curves
Characteristic times listed are the time associated with the peak E(t) value, the mean residence time, and the 95% tracer clearance time. Corrected values obtained by subtracting corresponding values for Injection profile from each other profile's values.

The corrected characteristic times for each of the experimental setups suggest differing flow phenomena experienced within each. The low t_{pk}^{*} values for each setup demonstrate the presence of significant levels of dispersion within the system. The low τ^{*} and t_{95}^{*} values for the empty cassette suggest significant channeling (due to the concentric alignment of the entrance and exit and lack of any flow distributor). Comparing the scaffold and void-plugged scaffold runs it is evident from the t_{pk}^{*} values that the void-plugged scaffold contains a smaller liquid volume (being displaced by the

plug). Additionally, the τ^* and t_{95}^* values suggest the presence of more back-mixing within the void-plugged scaffold. This could potentially be explained by the lack of a flow settling region (afforded by the void above the scaffold) in the void-plugged scaffold, causing the formation of internal eddies due to the direct injection of the tracer into the center of the top of the scaffold.

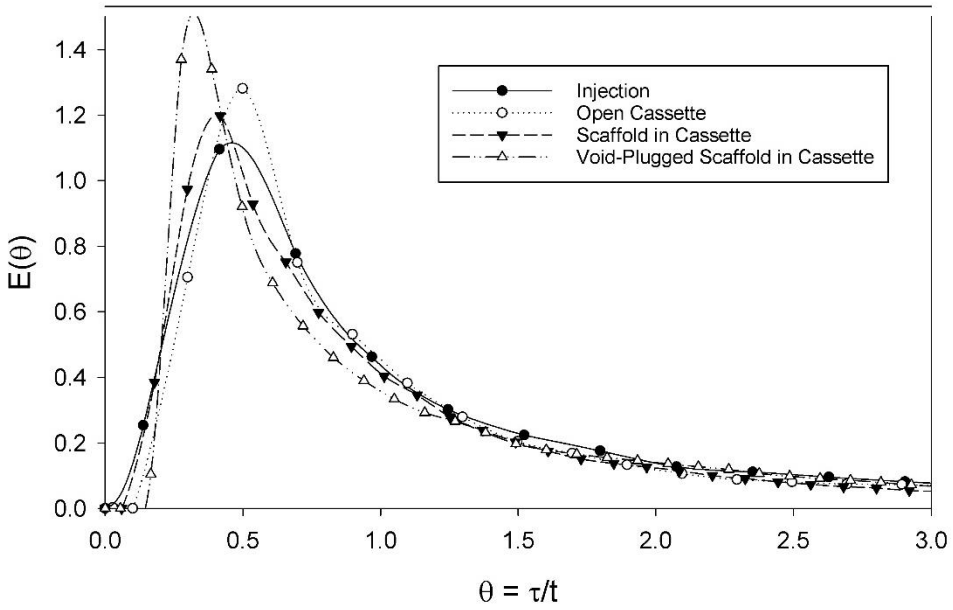

Figure 40. E(θ) - Pulse Tracer Input
Normalized residence time distribution functions for pulse tracer inputs into bioreactor. Same experimental setups as described in **Figure A2**. The θ values corresponding to each peak are 0.45, 0.50, 0.42, and 0.33, respectively. Error bars removed to facilitate viewing, with average standard deviations of approximately 15%.

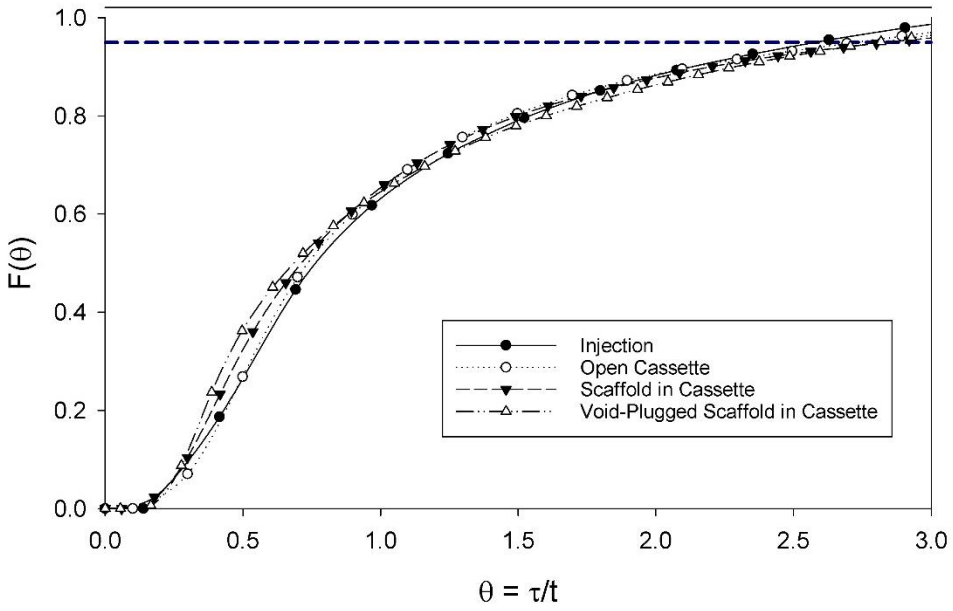

Figure 41. F(θ) - Pulse Tracer Input
Normalized cumulative distribution functions for pulse tracer inputs into bioreactor. Same experimental setups as described in **Figure A2**. All curves exhibit the same tailing behavior, but key differences are present in the range from 0-τ.

Figures A4 and **A5** demonstrate the similarity between all the experimental setups, all representing high dispersion within the system. Notably, the void-plugged scaffold is seen to exhibit a delayed, steeper, and narrower initial peak than the other systems, demonstrative of potential channeling as a result of the lack of a flow settling region (as described previously). Overall, the comparative analysis of the pulse tracer inputs suggests the presence of plug flow with high dispersion within all setups, though the significant tailing in the tracer input could be confounding the analysis. As such, step tracer input experiments were performed on the standard scaffold-in-cassette system to better elucidate the flow regime(s) present within the bioreactor.

A.2.2 Step Tracer Input

Three RTD experimental runs were performed with step tracer inputs at the bioreactor flow rate of 150 µL/min for the injection profile and the scaffold in cassette setups described in the previous section. The resulting concentration data was curve-fit, the resulting equations and parameters are provided in **Table 4**, below. This equation was then used to produce F(t), which was analytically differentiated to obtain E(t). The E(t) and F(t) curves for both setups are provided below in **Figure A6** and **Figure A7**, respectively.

The normalized residence time and cumulative distribution functions are provided in **Figure A8** and **Figure A9**, respectively, to better compare the two functions.

	Equation	**Parameters**			
		t_{bt}	C_1	C_2	t_f
Injection	$c(t) = c_0 - \frac{c_0}{1 + \left(\frac{t - t_{bt}}{C_1}\right)^{C_2}}$	15	19.3	2.48	-
Scaffold in Cassette	$c(t) = \left[c_0 - \frac{c_0}{1 + \left(\frac{t - t_{bt}}{C_1}\right)^{C_2}}\right] * (1 - W) + c_0 * W$ $W = \frac{t - t_{bt}}{t_f - t_{bt}}$	90	110.3	1.39	1100

Table 6. RTD Step Input Curve-Fitting Parameters
Curve-fit equations and parameters used for step input RTD c(t) curves. W is the weighting factor used to improve the fit for the scaffold-in-cassette run, c_0 is the concentration of the tracer injected, t_{bt} is the breakthrough time, t_f is the final time (at c = 99% of c_0), and C_1 and C_2 are curve-fitting parameters.

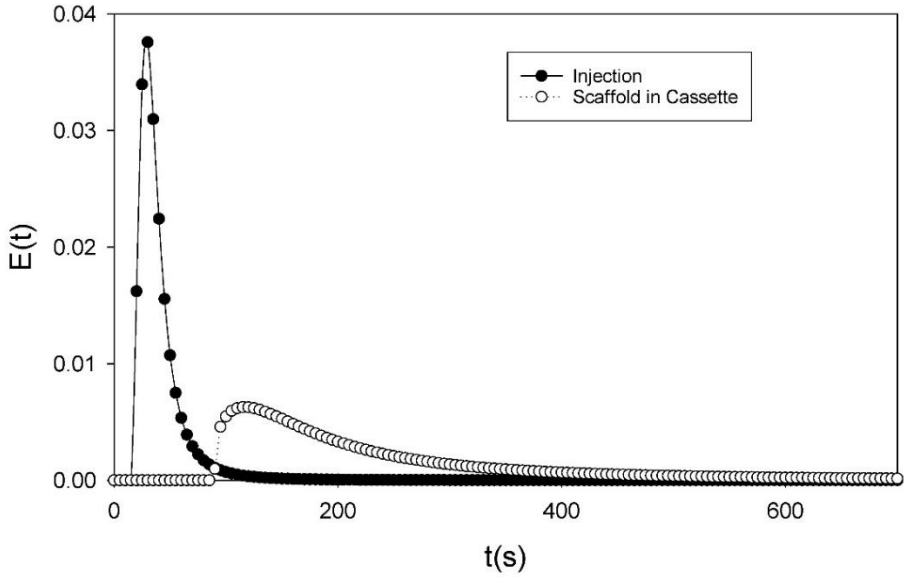

Figure 42. E(t) – Step Tracer Input
Residence time distribution functions for step tracer inputs into bioreactor. Injection (solid circles) is the tracer input profile; scaffold in cassette (open circles) is the exit profile from the cassette with a scaffold. The times corresponding to each peak, t_{pk}, are 30 s and 115 s, respectively. The mean residence times, τ, associated with each function are 36 s and 162 s, respectively. Error bars removed to facilitate viewing, with average standard deviations of approximately 8%.

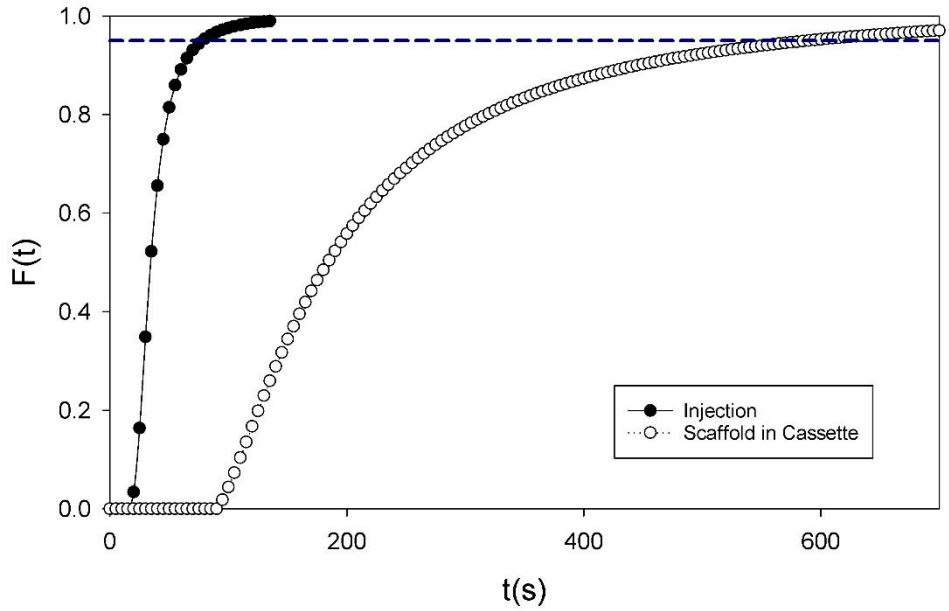

Figure 43. F(t) - Step Tracer Input
Cumulative distribution functions for step tracer inputs into bioreactor. Same experimental setups as described in **Figure A6**. The dashed horizontal line is located at F(t) = 0.95, representing the point at which 95% of the injected tracer had exited the reactor. The corresponding times for 95% tracer clearance, t_{95}, for each function are 80 s and 590 s, respectively.

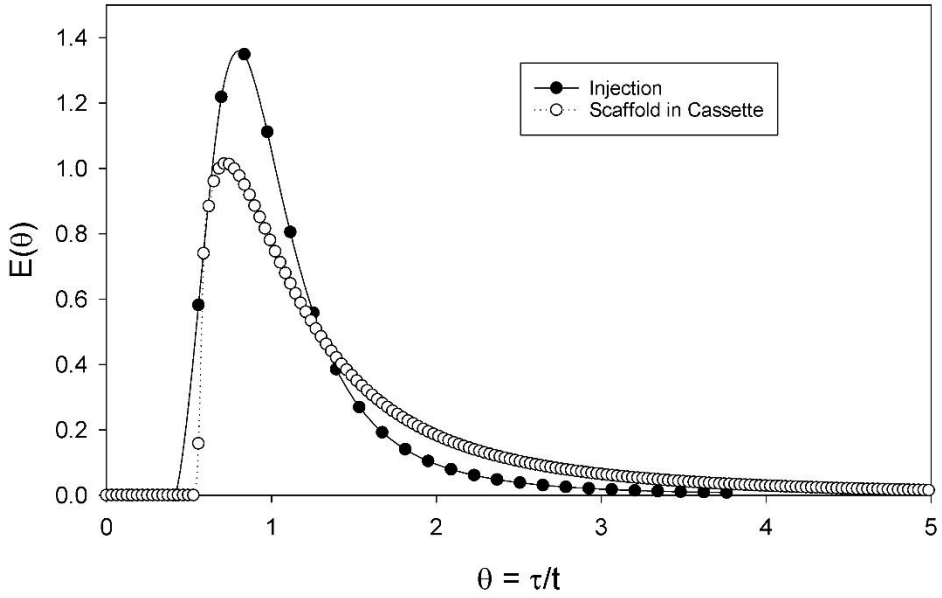

Figure 448. E(θ) - Step Tracer Input
Normalized residence time distribution functions for step tracer inputs into bioreactor. Same experimental setups as described in **Figure A6**. The θ values corresponding to each peak are 0.84 and 0.71, respectively. Error bars removed to facilitate viewing, with average standard deviations of approximately 8%.

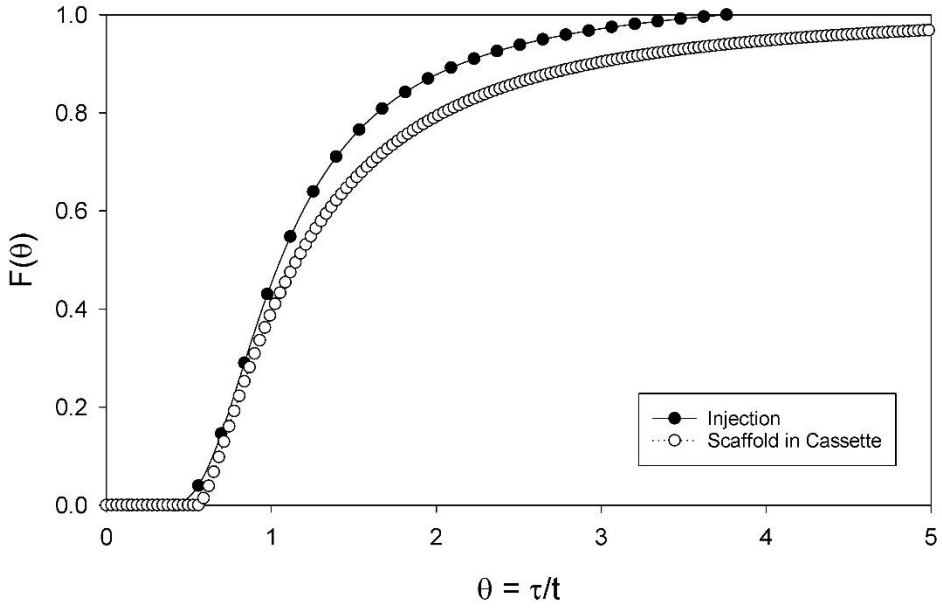

Figure 45. F(θ) - Step Tracer Input
Normalized cumulative distribution functions for step tracer inputs into bioreactor. Same experimental setups as described in **Figure A6**. Both curves demonstrate similar breakthrough θ values and general overall shape, with more significant tailing observed for the scaffold in cassette setup.

A much cleaner injection profile was achieved by the step input mode as opposed to the pulse input, exhibiting far less tailing, facilitating the effluent analysis of the reactor system. Significant tailing is still observed in the scaffold in cassette system, resulting in much higher t^* values: t^*_{pk} = 85 s, τ^* = 126 s, and t^*_{95} = 510 s. These, along with the much higher peak-associated θ-value for the bioreactor system strongly support the conclusion that the flow regime through the scaffold is well approximated as plug flow with significant dispersion. This conclusion is further buttressed upon comparing the E(θ) curve with a plug-flow with dispersion model curve from Levenspiel (side-by-side comparison provided in **Figure A10**).

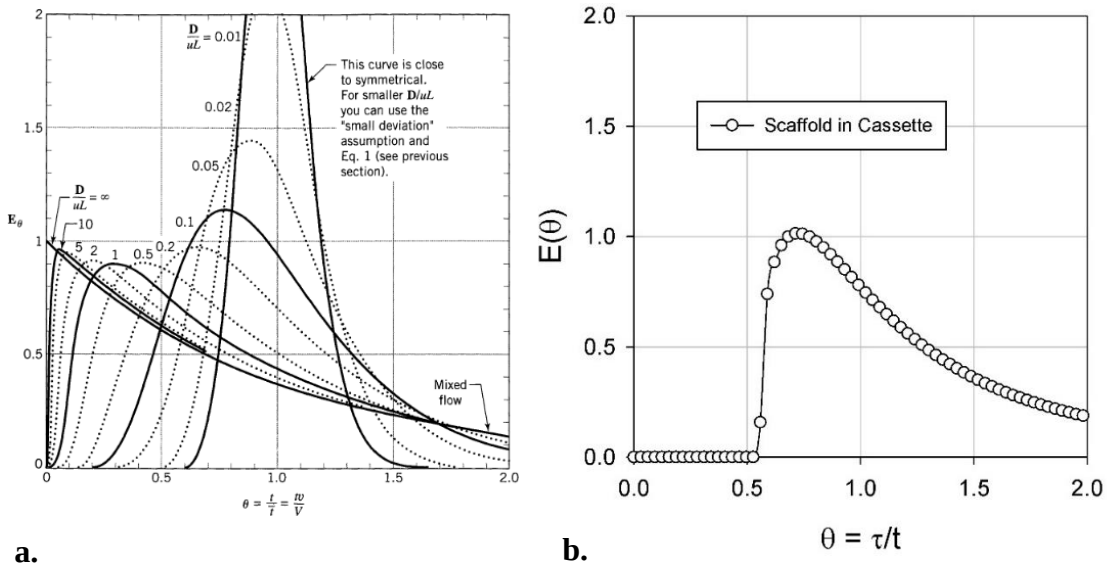

Figure 46. Comparison of RTD Data with Literature
A plot from Levenspiel's *Chemical Reaction Engineering* for the plug flow with dispersion model for various amounts of dispersion (a.) compared with the E(θ) function obtained from a step tracer input RTD experiment (b.). The great similarity between these two plots supports the conclusion that the flow profile through the scaffold is plug flow with dispersion. (**Figure A10a** copied from [99]).

A.2.3 Determination of Shear Stress

Based on the plug flow profile determined above, utilization of **Equation A11b** results in uniform initial wall shear stress values throughout the construct of approximately 0.017 dyne/cm^2. Although this value is on the lower end of those used by other groups, ranging from 0.001 to >10 dyne/cm^2, such low levels have still been shown to promote osteoblastic differentiation of MSCs [98]. As cells proliferate and deposit mineral, the pores will necessarily narrow (and become less homogenous), thereby resulting in increased wall shear stress values in addition to greater variability of such values throughout the construct. As such, it is beneficial to start at low shear stress values, allowing for increases throughout the culture period to still sustainable levels.

A.2.4 Summary of Flow Profile Analysis

Based upon the data presented in the above sections, it was concluded that the flow through the scaffold within the bioreactor is well approximated as plug flow with dispersion. Furthermore, it is theorized that the void space above the scaffold may act as a flow settling region, allowing for the distribution of species and momentum prior to entering the scaffold, thereby resulting in uniform species concentrations and flow velocities across the entrance to the scaffold. As such, it is concluded that a plug flow velocity distribution is appropriate to model the flow through the reactor (with modifications for the scaffold and cell impedance), which along with the assumption of uniform cell distribution throughout the scaffold (or at least a uniform distribution for all radial positions at a given axial coordinate) allows for the elimination of radial concentration gradients in both species concentrations and shear stress distributions.